Max-Planck-Institut
für Meteorologie

MAX-PLANCK-GESELLSCHAFT

International Max Planck Research School
on Earth System Modelling

Stratospheric Controls on Northern Hemispheric Storm Tracks

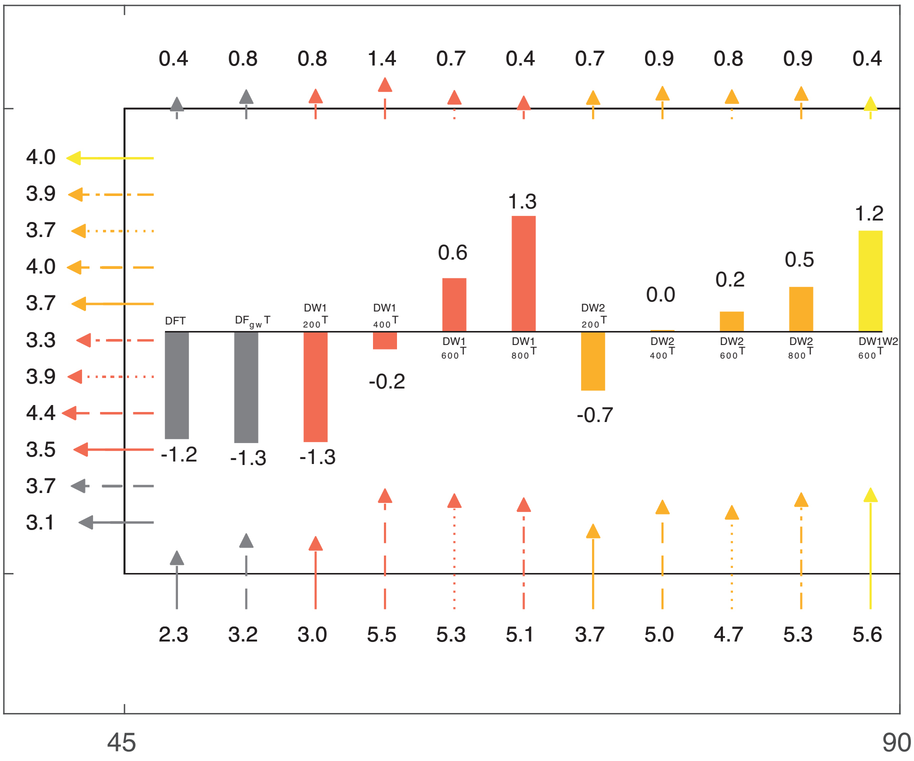

Tobias Haufschild

Hamburg 2019

Berichte zur Erdsystemforschung
Reports on Earth System Science

216
2019

Hinweis

Die Berichte zur Erdsystemforschung werden vom Max-Planck-Institut für Meteorologie in Hamburg in unregelmäßiger Abfolge herausgegeben.

Sie enthalten wissenschaftliche und technische Beiträge, inklusive Dissertationen.

Die Beiträge geben nicht notwendigerweise die Auffassung des Instituts wieder.

Die "Berichte zur Erdsystemforschung" führen die vorherigen Reihen "Reports" und "Examensarbeiten" weiter.

Anschrift / Address

Max-Planck-Institut für Meteorologie
Bundesstrasse 53
20146 Hamburg
Deutschland

Tel./Phone: +49 (0)40 4 11 73 - 0
Fax: +49 (0)40 4 11 73 - 298

name.surname@mpimet.mpg.de
www.mpimet.mpg.de

Notice

The Reports on Earth System Science are published by the Max Planck Institute for Meteorology in Hamburg. They appear in irregular intervals.

They contain scientific and technical contributions, including Ph. D. theses.

The Reports do not necessarily reflect the opinion of the Institute.

The "Reports on Earth System Science" continue the former "Reports" and "Examensarbeiten" of the Max Planck Institute.

Layout

Bettina Diallo and Norbert P. Noreiks
Communication

Copyright

Photos below: ©MPI-M
Photos on the back from left to right:
Christian Klepp, Jochem Marotzke,
Christian Klepp, Clotilde Dubois,
Christian Klepp, Katsumasa Tanaka

Stratospheric Controls on Northern Hemispheric Storm Tracks

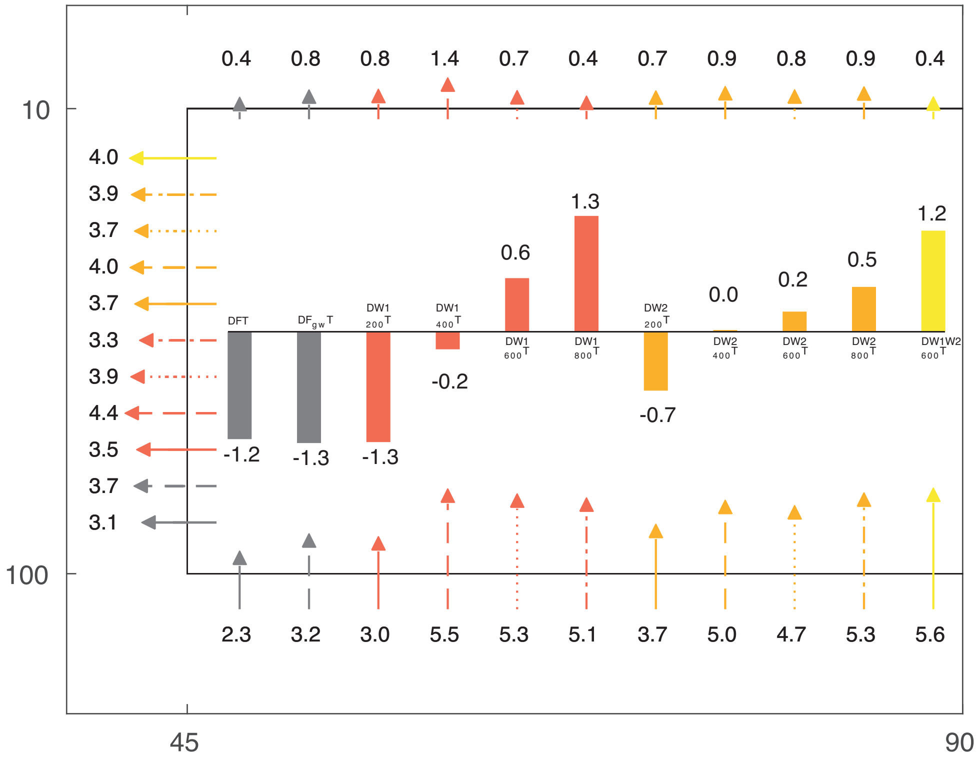

Tobias Haufschild

Hamburg 2019

Tobias Haufschild

Max-Planck-Institut für Meteorologie
The International Max Planck Research School on Earth System Modelling
(IMPRS-ESM)
Bundesstr. 53
20146 Hamburg

Universität Hamburg
Geowissenschaften
Meteorologisches Institut
Bundesstr. 55
20146 Hamburg

Tag der Disputation: 16. April 2019

Folgende Gutachter empfehlen die Annahme der Dissertation:
Prof. Dr. Gualtiero Badin
Dr. Elisa Manzini

Berichte zur Erdsystemforschung / Max-Planck-Institut für Meteorologie 216
Reports on Earth System Science / Max Planck Institute for Meteorology 2019

ISSN 1614-1199

Abstract

The winter time stratospheric circulation and the tropospheric storm track responses to global warming remain uncertain. Further, the understanding of the mechanisms by which the winter time stratospheric circulation response impact the tropospheric eddy-driven jet and storm track response is still incomplete. The framework of this thesis aims at isolating the mechanisms relevant for stratospheric circulation responses in order to constrain uncertainties. This is pursued by developing and applying the idealized ICON-DRY model. It is tailored to study the stratosphere-troposphere coupled response. More precisely, the model is constructed in such a way that it is non-simplified regarding the presentation of radiative processes, but highly idealized regarding the representation of moist processes. The dry tropospheric circulation is then forced by idealized prescribed zonally symmetric thermal forcing that substitutes moisture-related heating processes.

The model framework allows for prescribing additional thermal forcing. The procedure to test the circulation response to external forcing is, therefore, technically similar to the procedure in dry dynamical core models, but with a full representation of radiation-wave interactions. The experiments are performed by prescribing idealized additional thermal forcing that resembles Tropical Amplification (TA), Polar Amplification (PA) and CO_2 induced Stratopause Cooling (SC) in combination with idealized orography.

If only dry transient waves are involved in the response to TA, wave propagation changes dominate and wave generation changes are rather unimportant. Wave propagation changes are highly sensitive to the mean state of the control experiment's eddy-driven jet position. An increase of wave generation is only found, if stationary waves or moisture are included in the response to TA or if an additional zonally asymmetric PA is prescribed.

The presence of moisture leads to increased tropospheric wave generation amplifying the high latitude dissipation change and the easterly change of the polar vortex. Further, planetary wave generation increases potentially through and upward energy transfer from synoptic-scale waves.

Under dry conditions, if stationary waves are involved in the response to TA, two competing mechanisms are found: (1) The horizontal EP-flux (associated with wave propagation), whose response is a robust reduction of high latitude wave dissipation; and (2) The vertical EP-flux component, whose response is an increase of high latitude wave dissipation. This wave dissipation increase depends strongly on the surface orography amplitude. It is found that the decrease of the stratospheric polar vortex is associated with a significant equatorward shift of the eddy-driven jet. The stratospheric circulation change is, therefore, found to be the dominant factor in limiting the poleward shift of the eddy-driven jet as a response to TA.

The zonally asymmetric PA poses an additional wave source that increases wave flux into the stratosphere. If stationary waves are involved, constructive interference of the anomalous wave response with the stationary wave (orography) is found impacting the stratospheric circulation mainly due to shifting the preferred region of wave breaking downward and thereby leading to a pronounced amplification of the stratospheric response. Moreover, vertically coherent changes of zonal winds indicate a strong projection of the response onto the annular mode of variability.

The CO_2 induced Stratopause Cooling helps to weaken the polar vortex as its response is in the same direction as the change that is induced by stationary waves (orography). This suggests that interactive chemistry is needed to avoid stratospheric circulation biases in climate models.

Concerning the role of the baroclinic eddies in the response to TA, the high latitude static stability change is found to be intrinsically linked to the eddy-driven jet position change via the presence of stationary waves, which on their own are dynamically coupled to the stratospheric change. Since CMIP5 model simulations also show an increase in the static stability, this thesis identifies a sufficient condition for the static stability increase as well as the equatorward shift of the eddy-driven jet and storm tracks.

Zusammenfassung

Die Auswirkungen der globalen Erwärmung auf die stratosphärische Zirkulation und die troposphärische subpolare Tiefdruckrinne (Zyklonenbahn) sind nach wie vor unsicher. Des Weiteren ist nicht vollständig verstanden, wie die Veränderung der stratosphärischen Zirkulation den troposphärischen wirbel-angetriebenen Strahlstrom und die Zyklonbahnen beeinflusst. Diese Dissertation zielt darauf ab, die im Zusammenhang mit der stratosphärischen Zirkulation stehenden Prozesse zu isolieren und die Unsicherheit damit einzuschränken. Dies wird durch die Entwicklung und Anwendung eines idealisierten Models (ICON-DRY) realisiert. Die spezifische Anpassung des Models ermöglicht die Auswirkungen auf die stratopshärisch-tropophärische Kopplung zu untersuchen. Das Model simuliert Strahlungsprozesse ohne Vereinfachung, wohingegen Feuchtprozesse stark vereinfacht werden. Die trockene troposphärische Zirkulation wird durch einen idealisierten zonal-symetrischen thermischen Antrieb forciert. Der thermische Antrieb substituiert die mit Feuchtprozessen im Zusammenhang stehenden diabatischen Erwärmungsraten. Dem Model können zusätzliche thermische Antriebe vorgeschrieben werden, um die Auswirkung auf einen externen Antrieb testen zu können. Damit ist die technische Umsetzung vergleichbar mit derjenigen, die in trockenen dynamischen Modellen (dry dynamical core) verwendet wird; lediglich mit der Ergänzung, dass ICON-DRY die Interaktionen von Strahlung und atmopshärischen Wellen vollständig repräsentiert. Die Experimente werden durch das Vorschreiben zusätzlicher idealisierter thermischer Antriebe, die der tropischen Temperaturverstärkung (TA), der polaren Temperaturverstärkung (PA) und der durch CO_2 induzierten Stratopausen-Abkühlung (SC) ähneln, in Kombination mit idealisierter Orographie, durchgeführt.

Sind ausschließlich transiente Wellen vorhanden, zeigen sich als Reaktion auf TA verstärkte Änderungen in der Wellenpropagation. Diese wiederum sind sehr sensitiv für Positionsänderungen des wirbel-angetrieben Strahlstroms. Ein Anstieg der Wellenanregung zeigt sich nur, wenn stationäre Wellen oder Feuchtprozesse einbezogenen werden oder eine zusätliche zonal asymetrische PA vorgeschrieben wird.
Feuchtprozesse begünstigen die Anregung von troposphährischen Wellen und ver-

stärken die stratosphärische Wellendissipation in den hohen Breiten. Dies führt zu einer östlichen Windänderung des Polarwirbels. Des Weiteren werden die troposphärischen planetaren Wellen, vermutlich durch einen aufwärtsgerichteten Enrgietransfer, verstärkt.

Unter trockenen Bedingungen, wenn stationäre Wellen vorhanden sind, zeigen sich zwei gegensätzliche Mechansimen als Reaktion auf TA: (1) Zum einen führt die Änderung der horizontalen EP-fluss-Komponente zu einer robusten Verringerung der Wellendissiaption in den hohen Breiten; (2) Zum zweiten führt die Änderung der vertikalen EP-Fluss-Komponente zu einer Verstärkung der Wellendissiption, deren Änderung wiederum stark von der Amplitude der 0rographie abhängt. Die Änderung des stratosphärischen Polarwirbels steht in engem Zusammenhang mit der Positionsänderung des troposphärischen wirbel-angetriebenen Strahlstroms. Die Änderung der stratosphärischen Zirkulation limitiert die polwärtige Verschiebung des wirbel-angetriebenen Strahlstroms maßgeblich.

Die zonal asymmetrische PA verursacht zusätzliche Wellen, die den Wellenfluss in die Stratopshäre erhöhen. Wenn stationäre Wellen vorhanden sind, führt die konstruktive Interferenz der anomalen Welle mit der stationären Welle zu einer erhöhten Wellendissipation. Dies wird hauptsächlich durch die Verschiebung der Wellendissiaption von der oberen in die untere Stratospähere verursacht. Dabei kommt es zu einer verstärkten Abschwächung des Polarwirbels. Außerdem indizieren die vertikal kohärenten Änderungen der zonalen Windgeschwindigkeit eine Projektion auf die Arktische Oszillation.

Die CO$_2$ induzierte Stratopausen-Abkühlung trägt zur Abschwächung des Polarwirbels bei, weil ihre Änderungsrichtung der durch stationäre Wellen induzierten Änderungsrichtung entspricht. Dies deutet darauf hin, dass interaktive Chemie notwendig ist, um Fehler bei der stratophärischen Zirkulationänderung in Klimasimulationen zu vermeiden.

Im Bezug auf die Rolle der baroklinen Wirbel zeigt sich als Reaktion auf TA, dass die Änderung der statischen Stabilität in den hohen Breiten intrinsisch mit der Positionsänderung des wirbel-angetriebenen Strahlstroms über die Präsenz der stationären Wellen verbunden ist. Die stationären Wellen sind ihererseits mit der stratosphärischen Änderung dynamisch gekoppelt. Da in CMIP5 Simulationen ebenfalls eine Erhöhung der statischen Stabilität auftritt und diese im Zusammenhang mit der äquatorwärtigen Verschiebung der wirbel-angetrieben Strahlströme und Zyklonenebahnen steht, zeigt diese Dissertation eine hinreichende Bedingung für diesen Zusammenhang.

Contents

Abstract III

Zusammenfassung V

1 Introduction 1

1.1 Stratospheric and Tropospheric Zonal Circulations 1
1.2 Stratosphere-Troposphere Coupling at Intra-Seasonal Time-Scales . . . 3
1.3 Stratosphere-Troposphere Coupled Change in Climate Models 5
1.4 Stratosphere-Troposphere Coupled Change in Simplified Models 7
1.5 Novelty and Thesis Aim 9

2 ICON-DRY 13

2.1 Model Construction 13
  2.1.1 Model Base 13
  2.1.2 Radiation 13
  2.1.3 Surface Boundary Condition 14
  2.1.4 Theoretical Background 14
  2.1.5 Implementation of Thermal Forcing 21
2.2 Experimental Setups 22
  2.2.1 Control Configurations 22
  2.2.2 Sensitivity Experiments 24
2.3 Validation of the Control Configurations 26
  2.3.1 Equilibration 26
  2.3.2 Low-Frequency Variability 27
  2.3.3 Hemispheric Correlation 28
  2.3.4 Classification of the ICON-DRY's Atmosphere by Means of ERA-Interim Reanalysis 29
    2.3.4.1 Stationery Waves 30

2.3.4.2 Tropospheric and Stratospheric Mean State 33

3 Controls of the Stratosphere-Troposphere Response to Thermal Forcing in Idealized Models: Mean Changes 37

3.1 Transient Waves 37

3.1.1 Dry Atmosphere 37

3.1.2 Moist Atmosphere 46

3.2 Stationary Waves 49

3.2.1 Tropical Amplification 49

3.2.2 Polar Amplification 55

3.2.3 CO_2 Induced Stratopause Cooling 60

3.3 Baroclinic Eddies 62

4 Conclusions and Outlook 67

4.1 ICON-DRY 69

4.2 Controls of the Stratosphere-Troposphere Response to Thermal Forcing in Idealized Models: Mean Changes. 71

4.3 Outlook 76

Appendix XVII

List of Figures XXI

List of Tables XXIX

Acronyms XXXI

Acknowledgments XXXIII

Introduction

1

This thesis aims at identifying mechanisms relevant for the two-way coupled stratosphere-troposphere response to global warming, in particular with regards to the role of the stratospheric change in the storm track and eddy-driven jet responses. The problem is tackled by developing and applying a tailored idealized model framework.

The winter time stratospheric circulation and the tropospheric storm track responses to global warming remain uncertain. Further, the understanding of the mechanisms by which the winter time stratospheric circulation response impact the tropospheric storm track and eddy-driven jet responses are still incomplete. The eddy-driven jet was studied in idealized model frameworks with the aim of identifying mechanisms governing the responses. Reduced complexity, in many aspects, helped to understand principle mechanisms that affect the eddy-driven jet in a warming climate. However, most studies using idealized models investigated the eddy-driven jet response without a representation of stratospheric processes. Studies, that included the stratosphere simplified not only the troposphere but also stratospheric radiative processes. To reduce uncertainty in the stratosphere-troposphere coupled response to global warming, there is the need for constructing an idealized model framework that consist of a full representation of the stratospheric radiation.

In the following I will introduce the topic of this thesis in more detail by giving an introduction on the key elements of the stratospheric and tropospheric zonal circulations, followed by a review of the current literature regarding the stratosphere-troposphere coupling at intra-seasonal time-scales and the coupled response in climate and in idealized models. Afterward, I will present the novelty of this thesis and formulate the research questions.

1.1 Stratospheric and Tropospheric Zonal Circulations

The tropospheric and stratospheric zonal circulations are mainly characterized by 3 different types of westerly winds depicted in Figure 1. There are two jets in the troposphere, that are the subtropical jet and the eddy-driven jet. The subtropical jet is caused by the meridional transport of angular momentum at the upper edge of the Hadley circulation and by the equator-pole temperature gradient. Due to the vertical shear of winds and the meridional temperature gradient the subtropical jet is baroclinic, meaning it facilitates growth of instabilities.

The eddy-driven jet stretches from the upper troposphere to the surface of the mid-latitudes. This westerly flow is balanced by the vertically integrated eddy momentum

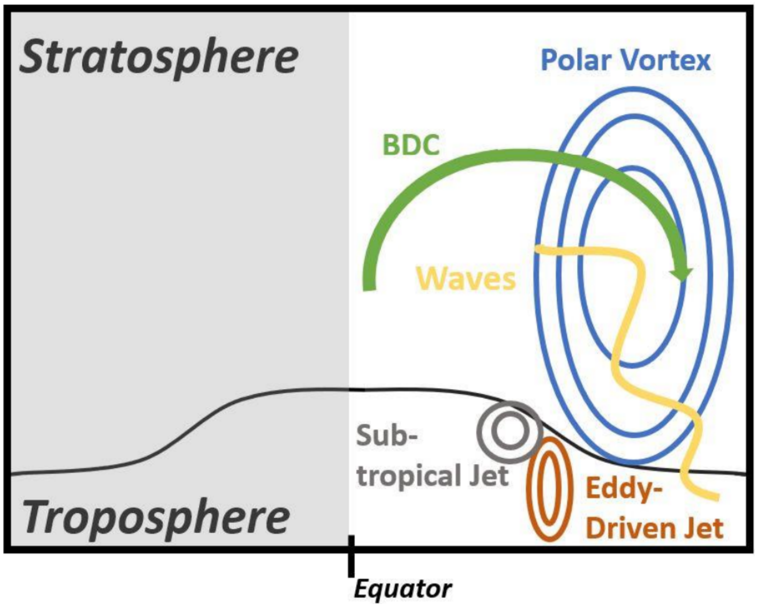

Figure 1.1. Sketch of the key elements of the tropospheric and stratospheric circulation. Depicted are the polar vortex, the subtropical jet, the eddy-driven jet, the Brewer-Dobson circulation (BDC) and the upward propagation of waves. The black line separating the stratosphere and the troposphere represents the tropopause region .

convergence and the surface drag. The momentum convergence occurs mostly in transient (baroclinic) eddies, which is why the jet is called eddy-driven. Since the eddy-driven jet has much less vertical shear of winds and a weaker meridional temperature gradient, it is considered to be rather barotropic in its nature than the subtropical jet, even though it is forced by baroclinic transient eddies.(Vallis, 2006). The maximum of the eddy-driven jet surface westerlies can be used as a proxy for the position of the storm tracks (Lu et al., 2010). The storm-track is shaped by zonal asymmetries (land and ocean distribution) and eddy dynamics themselves.

The wintertime stratospheric circulation is characterized by circumpolar westerly winds known as the stratospheric polar vortex (Palmer, 1959; Waugh et al., 2017). The stratospheric polar vortex is forced by the meridional differential heating caused by absorption of ultra-violet radiation (Fels, 1985; Shine, 1987). It is characterized by large variability (i.e departure from the radiative equilibrium) which is forced by dissipation (i.e wave breaking) of waves (e.g Geller, 1983) that originate predominantly in the troposphere, decelerating the polar vortex by transferring their momentum onto the zonal flow. There is also thermal wave dissipation that occurs due to radiative processes. In this way, stratospheric dynamics differ fundamentally from the tropospheric dynamics. The tropospheric dynamics are driven by instabilities making the troposphere turbulent[1] whereas the stratospheric dynamics are driven by dissipation of waves that originate in the turbulent troposphere. The turbulent troposphere gives rise to gravity waves, whose restoring force is gravity or buoyancy and Rossby waves whose restoring force is the meridional change of the Coriolis force. These waves propagate vertically into the stratosphere and mesosphere, and depending on their wave properties and the background flow, break at particular heights. Gravity wave breaking plays an important role in the upper stratosphere and mesosphere. Rossby waves break predominantly in the stratosphere, and are the major driver of stratospheric variability (Plumb, 2002).

---

[1] The term turbulent refers to the large-scale turbulent flow, not to the the turbulent boundary layer

Rossby waves can be separated into planetary-scale waves with zonal wavenumbers between 1 and 3 and synoptic-scale waves with wavenumbers larger 3. Synoptic-scale Rossby wave breaking only plays a role in the lowermost stratosphere. Planetary-scale Rossby waves break at all stratospheric heights and are the main focus of this thesis. The Rossby waves' zonal group speed can be eastward or westward depending on the wave number. The Rossby waves' zonal phase speed, however, is always westward, relative to the background flow (Rossby, 2015). Since the summer time stratosphere consists of easterly (east to west) zonal winds only fast Rossby waves are able to travel into the summer stratosphere. Quasi-stationary waves are blocked and can not travel into the stratosphere. However, the winter time westerly zonal winds allow for quasi-stationary wave propagation. (Andrews et al., 1987).

Vertical wave propagation allows the troposphere to impact the stratospheric dynamics which can be described as an upward connection. However, there is also a downward connection that enables the stratosphere and its variability to impact the tropospheric circulation, by that forming a two-way coupled system (Baldwin and Dunkerton, 1999). The downward connection is illustrated in Figure 1.2. It shows a composite of anomalously weak and strong polar vortex events using reanalysis (ERA-Interim) data from the European Centre for Medium-Range Weather Forecasts between 1979 and 2008. After the onset of weak or strong vortex anomalies the anomalies propagate downward and affect the tropospheric circulation 1 to 3 weeks later. The stratospheric anomalies project onto the annular modes of tropospheric variability (Thompson and Wallace, 1998) and thereby affect the eddy-driven jet and storm tracks (Lorenz and Hartmann, 2001; Nigam, 1990).

1.2 Stratosphere-Troposphere Coupling at Intra-Seasonal Time-Scales

The influence of the stratospheric polar vortex on the tropospheric dynamics was, firstly, mentioned by Bates (1977). Using a two-dimensional model he showed that the

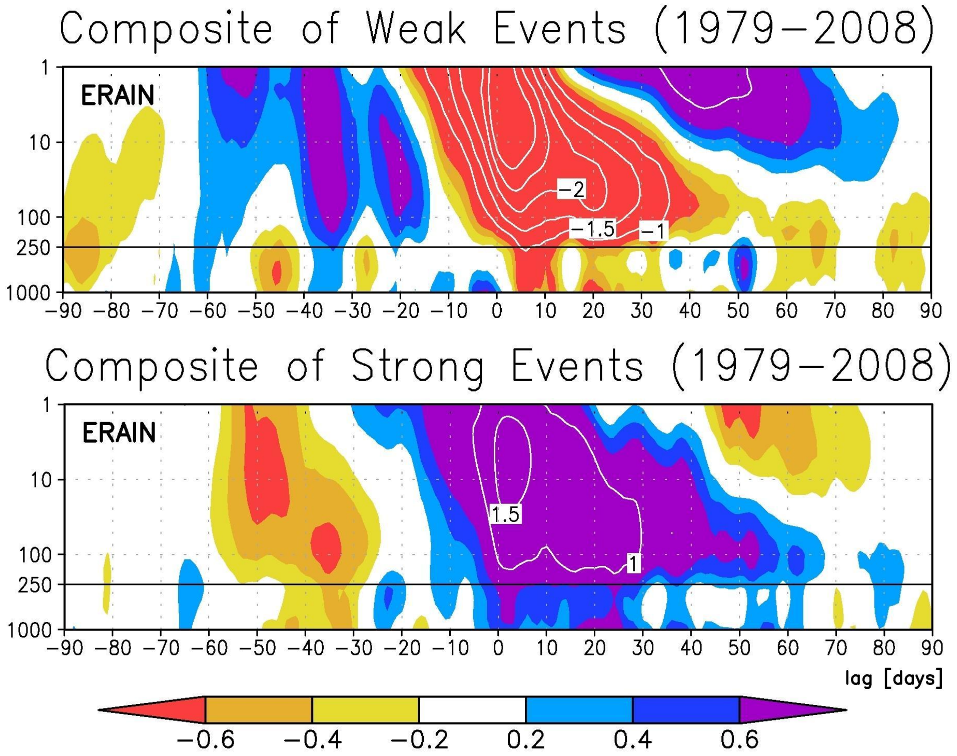

Figure 1.2. Composite of weak and strong polar vortex events represented by the Northern annular mode, calculated using the geopotential height at all levels between 1 hPa and 1000 hPa and between 20°N 90°N. The events are determined by the dates on which the 10 hPa annular mode values cross -3 and +1.5, respectively. With respect to those onset dates composites are calculated covering a period ranging from -60 day lag to +60 day lag. The composite consists of 15 weak events and 32 strong events. Color shading and contours show the standard deviation. The Figure is produced by using ERA-Interim data during 1979 -2008 and therfeore is an update of the Figure of Baldwin and Dunkerton (2001) who used reanalysis data from the National Centers for Environmental Prediction during 1958-1999

meridional heat flux of ultra-long waves in the troposphere is sensitive to changes in the stratospheric wind profile and the static stability. Using 2-dimensional models, this influence was confirmed by Geller and Alpert (1980) who found that changes in the zonal winds in the vicinity of 35 km or below give rise to changes in the tropospheric planetary-wave pattern that are on the same order as the observed inter annual variability. Further, evidence for a stratospheric influence on the upper troposphere stationary waves was found by Schmitz and Grieger (1980) and Lin (1982). Building upon this result Boville (1984) showed that not only the planetary waves are influenced, but also the transient eddies at all scales.

The capability of the stratospheric zonal mean zonal winds to impact the tropospheric zonal mean zonal wind was confirmed by Kodera et al. (1990) who showed that strong

December stratospheric zonal winds were followed by intensified polar tropospheric zonal winds in February. Several studies showed that the lower stratospheric wintertime polar vortex variability is strongly coupled to the North Atlantic oscillation (NAO) (e.g Baldwin et al., 1994; Perlwitz and Graf, 1995). Thompson and Wallace (1998) showed that this coupled pattern projects onto the leading empirical orthogonal function (EOF) of the Northern hemisphere wintertime monthly mean sea level pressure (slp). They refer to the leading EOF of the slp as the Arctic Oscillation (AO), which is characterized by zonally symmetric meridional seesaw pattern in atmospheric mass, similar to the variations at stratospheric levels. Further, Thompson and Wallace (2000) pointed out that the Northern and Southern hemispheric annular modes amplify with height upward into the stratosphere when planetary wave-mean flow interactions are permitted. By examining separately time series of the AO at tropospheric and stratospheric levels, Baldwin and Dunkerton (1999) showed that AO anomalies that appear in the stratosphere propagate downward into the troposphere. Further, a correlation analysis revealed that the surface anomalies lag peaks of stratospheric anomalies by about three weeks. Moreover, they pointed out that the surface anomalies were characterized by a considerable change in the the storm tracks and strength of the mid-tropospheric flow. Composites of weak and strong polar vortex events confirmed the downward propagation of stratospheric anomalies and the influence on storm tracks a few weeks after the onset (Baldwin and Dunkerton, 2001).
Shaw et al. (2010) termed the downward propagation of stratospheric anomalies is as the zonal mean coupling since it strongly projects onto the annular mode. Another form of coupling occurs due to reflection of waves, which is known as downward wave coupling. Perlwitz and Harnik (2003) found that when the polar night jet peaks in the high latitude mid-stratosphere, zonal waves with a zonal wave number 1 get reflected back toward the troposphere. Shaw et al. (2010) showed that in the Southern hemisphere, the downward wave-1 coupling dominates, whereas in the Northern hemisphere downward wave-1 coupling and zonal-mean coupling are found to be equally important.

1.3 Stratosphere-Troposphere Coupled Change in Climate Models

In CMIP5 (Coupled Model Intercomparison Project Phase 5) models the annual mean eddy-driven jet is robustly projected to shift poleward of about 1° to 2° (Barnes and Polvani, 2013; Swart and Fyfe, 2012) in the response to anthropogenic forcing (RCP8.5). However, for the winter time Northern hemisphere when the stratosphere and troposphere are dynamically coupled (active season) Barnes and Polvani (2013) showed a considerable uncertainty in the direction of the eddy-driven jet shift. A bit less than 50% of the model responses show an equatorward shift of the eddy-driven jet and sightly more than 50% show a poleward shift. A similar but not that pronounced uncertainty in the eddy-driven jet direction shift was found in Autumn (active season) in the Southern hemisphere.

A similar spread was found in the projection of the high latitude stratospheric winds. Manzini et al. (2014)) shows that two-thirds of the CMIP5 models show an easterly change of the high latitude stratospheric winds, whereas one-third show a westerly change. They further demonstrated that a considerable amount of the uncertainty in the projection of the surface annular mode originates in the uncertainty in the projection of the stratospheric polar vortex. The impact of the stratospheric polar vortex change on the tropospheric annular mode response and eddy-driven jet response was consolidated by studies that found a significant relationship between the stratosphere polar vortex change and the surface climate change (Karpechko and Manzini, 2012; Scaife et al., 2012; Simpson et al., 2018)).

There were several attempts to explain the mechanisms that govern the stratospheric circulation change and the uncertainty in climate models. Song and Robinson (2004) suggested that the planetary-wave induced high latitude deceleration is an important step in the downward influence of stratospheric changes. Sigmond and Scinocca (2010) showed that the Northern hemispheric polar vortex change depends on the basic state of the atmosphere. In particular they showed that the lower stratospheric winds play an important role in determining the circulation response to climate change. Recently, Karpechko and Manzini (2017) showed that in CMIP5 models driven by prescribed SSTs all models reveal a stratospheric dynamical warming, mostly due to increased upward propagation of quasi-stationary wavenumber 1. They further demonstrated that the increase in wave flux to the stratosphere is related to the strengthening of the zonal winds in the subtropics and mid-latitudes near the troposphere.

The role of the baroclinic eddies in the stratosphere-troposphere coupled response was also investigated in climate models. Song and Robinson (2004) supported the idea that the tropospheric response due to changes in the stratosphere is enhanced via a transient eddy feedback. Further, climate models with low stratospheric resolution show an increase of maximum growth rate for baroclinic eddies as a response to increased CO_2 concentrations (Yin, 2005) and as a response to increase SSTs (Frierson et al., 2007). However, Scaife et al. (2012) found in addition, that climate models with well resolved stratosphere show a consistent latitudinal change in baroclinic growth rates, shifting the preferred latitude for growth of eddies, and hence the storm track southwards. However, Hitchcock and Simpson (2016) found using an climate model with prescribed SST that the key mechanism for the downward coupling, involves the tropospheric planetary waves, which are modified by the stratospheric anomalies, and concluded that the direct influence of the stratosphere on the synoptic-scale eddies and the balanced downward control response are relatively unimportant.

The Northern hemisphere retreat of sea ice is an integral part of the anthropogenic climate change. Recently, the impact of the sea ice retreat of the Barent- and Kara Seas on the large-scale circulation became subject of interest as a consequence to the fast decline in sea ice extent since 2007 (Petoukhov and Semenov, 2010). The retreat of sea ice in localized regions imposes an asymmetric component in Arctic amplification. It was shown that the impact of the asymmetric component of sea ice retreat may emerge in two ways, as a localized thermal response and as remote dynamical response via a stratospheric pathway (e.g Jaiser et al., 2013; Kim et al., 2014; Nakamura et al., 2016). The studies showed a crucial role of the stratosphere in the sea ice impact on the mid-latitudes by coupling between the stratospheric polar vortex and planetary-scale waves. Further, the asymmetric component of sea ice retreat poses a stationary wave source that may interact constructively or destructively with the background stationary wave. Sun et al. (2015) reported that depending on the region of sea ice retreat the response of the stratospheric polar vortex is of opposite sign due to constructive or destructive interference. Depending on whether the effect of the Pacific (Cai et al., 2012) or the Barents-Kara sea (Kim et al., 2014) sea ice loss dominate destructive or constructive interference occurs, respectively. However, the stratospheric responses due to sea ice retreat are often found to be statistically non-significant. (Peings and Magnusdottir, 2014a; Screen et al., 2013).

1.4 Stratosphere-Troposphere Coupled Change in Simplified Models

Idealized general circulation models were used to test the dynamical responses to global warming by prescribing idealized thermal forcing that represent the characteristic signatures of global warming such as Tropical Amplification (TA) and Polar Amplification (PA). Idealized models were used to reduce the complexity with the aim of understanding the underlying mechanisms that are governing the responses, which in complex climate models can not be shown due to internal variability (Shepherd (2014)).The Held-Suarez (HS) experiment is the most commonly used idealized model. It was developed to evaluate the dynamical cores of atmospheric general circulation models, independently of the physical parameterization. Perturbations are relaxed to a prescribed temperature profile, which is realized by the use of a Newtonian cooling scheme (Held and Suarez, 1994). All studies mentioned in this section used the concept of the HS model experiment. They may differ slightly regarding the parameter settings, forcing and dissipation.

Eichelberger and Hartmann (2005) prescribed TA and found a strengthened Brewer-Dobson circulation (BDC) associated with increased wave flux into the stratosphere. In contrast, as a response to TA Butler et al. (2010) found a weakening of the BDC and pointed to the decrease in stratospheric wave flux. Wang et al. (2012) showed that a regime change may occur in HS models, when the tropical heating exceeds a certain threshold value. They found a moderate strengthening of the BDC for a weak TA, but a weakening of the BDC for a strong TA. They argued, that this regime change may be related to the opposing BDC responses found in Eichelberger and Hartmann (2005) and Butler et al. (2010). However, their model includes a stationary planetary wavenumber 2, that both other models don't.

Idealized general circulation models were also used with the aim of understanding the stratospheric circulation change and its impact on the tropospheric circulation including the eddy-driven jet and storm tracks by systematically changing the stratospheric vortex strength. Polvani and Kushner (2002) showed, that the eddy-driven jet shifts poleward when the stratospheric polar vortex strengthens due to imposed stratospheric cooling. Gerber and Polvani (2009) showed, that in both, the climatological mean and on intraseasonal time-scales, a weaker vortex is associated with an equatorward shift in the tropospheric eddy-driven jet. More over, they demonstrated, that the mean structure and variability of the stratospheric polar vortex is sensitive to the amplitude of the topography, and a realistic frequency of stratospheric sudden warming events, occurs only for a relatively narrow range of topographic heights.

The role of the baroclinic eddies in the stratosphere-troposphere coupled response was investigated also in simplified models. Kushner and Polvani (2004) found, that the stratospheric cooling induces a response, that is confined to the stratosphere in the absence of eddy feedbacks. In the contrast, the stratospheric response penetrates into the mid-troposphere when eddy feedbacks are included. However, they found no impact of the eddy feedback on the position of the eddy-driven jet. The relationship between the polar vortex strength and the position of the eddy-driven jet was shown to exist also when topographically forced stationary waves were included (Gerber and Polvani, 2009). Domeisen et al. (2013) showed that the synoptic eddy feedback is necessary to shift the eddy-driven jet equtorward after Sudden Stratospheric Warmings (SSW).

1.5 Novelty and Thesis Aim

In idealized numerical models the uncertainty in the eddy-driven jet, so far, was mostly studied without a realistic dynamical representation of the stratosphere (e.g. Baker et al., 2017; Butler et al., 2010). Most idealized models (e.g. Held-Suarez (HS) model) used a prescribed temperature profile together with a Newtonian cooling scheme, that relaxes perturbations to the prescribed profile. Such models have the advantage that they provide complete control over the basic state, but require to set up relaxation time-scales in the troposphere and stratosphere. This means, that the radiative processes in the stratosphere are simplified. Radiation-wave interactions are crucial for stratospheric dynamics. Because of the sensitivity of the wave properties to the relaxation time-scales and since it was shown that the stratosphere is important for the wintertime tropospheric dynamical responses, there is a need for developing a simplified model that is, regarding the representation of radiative processes, not simplified. However, when using a physical radiation scheme in the model, prescribing a temperature profile, as in the HS model, is no longer possible. Therefore, the first question this thesis addresses is:

- **Is it possible to construct an idealized numerical model that provides full radiation-wave interactions but which at the same time is highly idealized in its moist processes, allowing for prescribing tropospheric thermal forcing conceptually similar to the HS model?**

  This questions emerges because it is not obvious that its is technical feasible. On the one hand full radiation disallows prescribing a temperature profile. On the other hand making the model dry leads to an unrealistic zonal mean temperature state. Hence, a dry model with full radiation needs a forcing in order to achieve a realistic circulation. Whether this is feasible is unclear.

In order to constrain the uncertainty in the eddy-driven jet, there is the need to understand the dynamical processes of the two-way coupled stratosphere-troposphere response to global warming. Since, the downward connections occurs not only at monthly but also at centennial (i.e. climate change) time-scales (Kidston et al., 2015), in this thesis I focus on long time-scales, addressing the question of the steady state two-way coupled stratosphere-troposphere response to global warming with the aim of identifying factors possibly controlling the stratospheric vortex and the eddy-driven jet response.
The questions, that I address regarding the stratosphere-troposphere coupled response to additional thermal forcing are:

- **What is the role of transient waves in the stratospheric polar vortex and eddy-driven jet response to tropical amplification for different background states**?

  The question is of interest since even in simplified model with only transient waves no consistent stratosphere response to TA was found so far. An idealized model that consists of full radiation, bridging between Aquaplanet models and HS model may provide the opportunity to constrain the uncertainty.

- **Do moisture related effects impact the troposphere-stratosphere coupled response on a flat surface**?

  Until now the effects of moisture on the stratospheric circulation response to TA were not studied in an idealized model framework with full radiation. Moisture might be important for the stratospheric circulation change as it affects the development of baroclinic instabilities (Geen et al., 2016) and Rossby waves through upscale-energy transfer (Doyle et al., 2014). The effects of moisture may be isolated by comparing the dry idealized model with full radiation to a moist version of an equivalent model.

- **What is the role of stationary waves in limiting the poleward shift of the eddy-driven jet through a stratospheric pathway**?

  There are indications that stationary waves play a crucial role in the response of the stratospheric circulation and in the response of the downward coupling to the troposphere (Karpechko and Manzini, 2017). Prescribing, systematically, idealized orography with different amplitudes provides the opportunity of investigating the sensitivity of the stratospheric circulation response and its impact on the eddy-driven jet to stationary waves in the response to TA.

- **Is there a condition, under which the asymmetric component of polar amplification affects the eddy-driven jet through a stratospheric pathway**?

  The stratospheric responses to sea ice retreat could not be found with statistical significance. Further, it is unclear to which extent the arctic amplification is affecting the mid-latitudes (Screen, 2014). Since the impact of the asymmetric component of PA was, so far, only studied in climate models, an idealized model approach may be useful to clarify whether, the localized sea ice retreat has a significant impact on the mid-latitudes via an stratospheric pathway.

- **How large is the potential bias in the stratospheric response without chemistry**?

  Most climate models do not have interactive chemistry because it is computational very costly. Instead, climate models usually prescribe trends in ozone (O_3) concentration that are obtained from an interactive climate-chemistry model. In the real atmosphere the concentration of O_3 ,however, depends on the temperature evolution as the chemical reaction between NO_x and O_3 is temperature-dependent. A CO_2-induced cooling of the stratosphere therefore affects O_3 concentrations. In fact, a cooling of the stratosphere means reduced reaction rate between NO_x and O_3 leading to more O_3 to remain in the stratosphere and therefore increasing the absorption of ultra-violet radiation and reducing the cooling. Some of the CO_2 induced cooling, therefore, is compensated due to increased absorption of ultra-violet radiation. Neglecting interactive chemistry, therefore, may add a bias in the projection of the stratospheric polar vortex response.

- **What is the role of the baroclinic eddies in the stratosphere-troposphere coupled response including different stationary wave amplitudes?**

  This question is of interest since there are conflicting responses regarding the role of the planetary and synoptic waves in the stratosphere-troposphere coupled response in idealized models (Domeisen et al., 2013; Hitchcock and Simpson, 2016). Since Scaife et al. (2012) showed that the high latitude Eady growth rate change is associated with an equatorward shift of the preferred latitude of growth of eddies, this question focuses on the growth rate of baroclinic eddies for different stationary wave numbers and amplitudes in the response to TA.

The thesis is structured as follows. Chapter 2 addresses the first question by introducing the ICON-DRY model. It further describes the method and validates the model. Chapter 3 tackles the remaining questions by quantifying the dynamical responses to Tropical Amplification, Polar Amplification and CO_2 induced stratopause cooling relative to the different control experiments. Chapter 4 summarizes and discusses the results and eventually gives an outlook on future work.

ICON-DRY

2

2.1 Model Construction

This section introduces the ICON-DRY model. After a short introduction on the main aspects of the ICOsahedral Non-hydrostatic (ICON) model it describes in detail the ICON-DRY model's configuration in terms of atmospheric forcing. In particular it explains the theoretical background of the ICON-DRY's atmospheric thermal forcing and the algorithm with which the thermal forcing function is obtained.

2.1.1 Model Base

ICON-DRY is an dry idealized model based on the ICON model developed by the German weather service (DWD) and the Max-Planck Institute (MPI) for Meteorology. The model uses the MPI physics package which originates from the ECHAM6 general circulation model. The ICON dynamical core solves the fully compressible non-hydrostatic equations of motion. Further, the ICON model provides exact local mass conservation, mass-consistent tracer transport and a flexible grid nesting capability. The dynamical core is formulated on an icosahedral-triangular Arakawa C grid. Time integration is performed with a two-time-level predictor- corrector scheme that is fully explicit, except for the terms describing vertical sound-wave propagation. Competitive computational efficiency is achieved by applying a time splitting between the dynamical core on the one hand and tracer advection, physics parameterizations and horizontal diffusion on the other hand (Zängl et al., 2015). Further information about the ICON model can be found in Wan et al. (2013) and Giorgetta et al. (2018).

2.1.2 Radiation

Motivated by the dependence of the depth and duration of lower stratosphere thermal perturbations to the radiative damping rates (Hitchcock et al., 2013) ICON-DRY includes the ECHAM model radiative transfer (Giorgetta et al., 2018). In terms of radiative-wave interactions, when comparing the ICON-DRY model to an Held-Suarez (HS) model, it, therefore, consists of a non-simplified stratosphere. In the stratosphere the short wave radiation is absorbed by a fixed hemispherically symmetric prescribed equinoctial ozone distribution, which heats up the equatorial stratosphere and drives westerly stratospheric polar vortexes in both hemispheres. The short wave radiation includes a diurnal cycle. The tropospheric atmosphere in ICON-DRY is hardly impacted by the short wave radiation because of the fixed sea surface temperatures (SSTs) and the dry atmospheric conditions. Stratospheric chemistry, as used in the majority of climate (CMIP) models is neglected.

2.1.3 Surface Boundary Condition

The model's surface boundary is defined by prescribed SSTs. The SSTs are uniformly distributed in the zonal direction. In the meridional direction a temperature gradient is prescribed, that drives the general tropospheric circulation through the generation of baroclinic instabilities on a rotating globe. Since the most frequently used Aquaplanet (AP) SST profile proposed by Neale and Hoskins (2000) has been developed to study mainly tropical dynamics it lacks by purpose a high latitude temperature gradient. Therefore, following Thatcher and Jablonowski (2016) a profile is prescribed, that is close to the APE-SST profile in the tropics but includes a high latitude temperature gradient, that follows the bottom layer temperature distribution of an HS model, that has been developed to study extra-tropical dynamics. The meridional temperature profile is defined by:

$$T_s = \Delta T \ \ exp\big(-\frac{\phi^2}{2(\Delta\phi)^2}\big) + T_{min} \tag{2.1}$$

where ΔT is the equator- pole temperature difference, that is 29 K, T$_{min}$ the minimum temperature at the pole, that is 271 K, ϕ the latitude in radians and $\Delta\phi$ = $26\pi/180$.

2.1.4 Theoretical Background

The ICON-DRY technically descends from the Aquaplanet experiment (APE) and can be classified as a dry (simplified) version of an APE. Its atmospheric forcing is identical regarding the Coriolis force, the short wave radiation and the SSTs. It differs from an APE regarding the dry atmosphere whose circulation is driven by idealized thermal forcing. The idealized thermal forcing substitutes atmospheric heating rates related to moist processes in order to drive a tropospheric circulation which is realistic in terms of magnitude and spatial scales.

Atmospheric moist convection arises due to instabilities. It transports latent heat to atmospheric levels aloft, and drives not only tropical waves but also the tropical, subtropical and mid-latitude circulation indirectly through latent heat release. The strength of the subtropical jet depends on the angular momentum transport which depends on the strength and extent of the Hadley cell which on its own depends on the latent heat release. The strength of the subtropical jet depends on the upper level equator-pole temperature gradient which depends on the tropical temperatures and therefore on the latent heating. The eddy-driven jet may even be impacted by the release of tropical latent heat since the broad tropical and subtropical warming impact

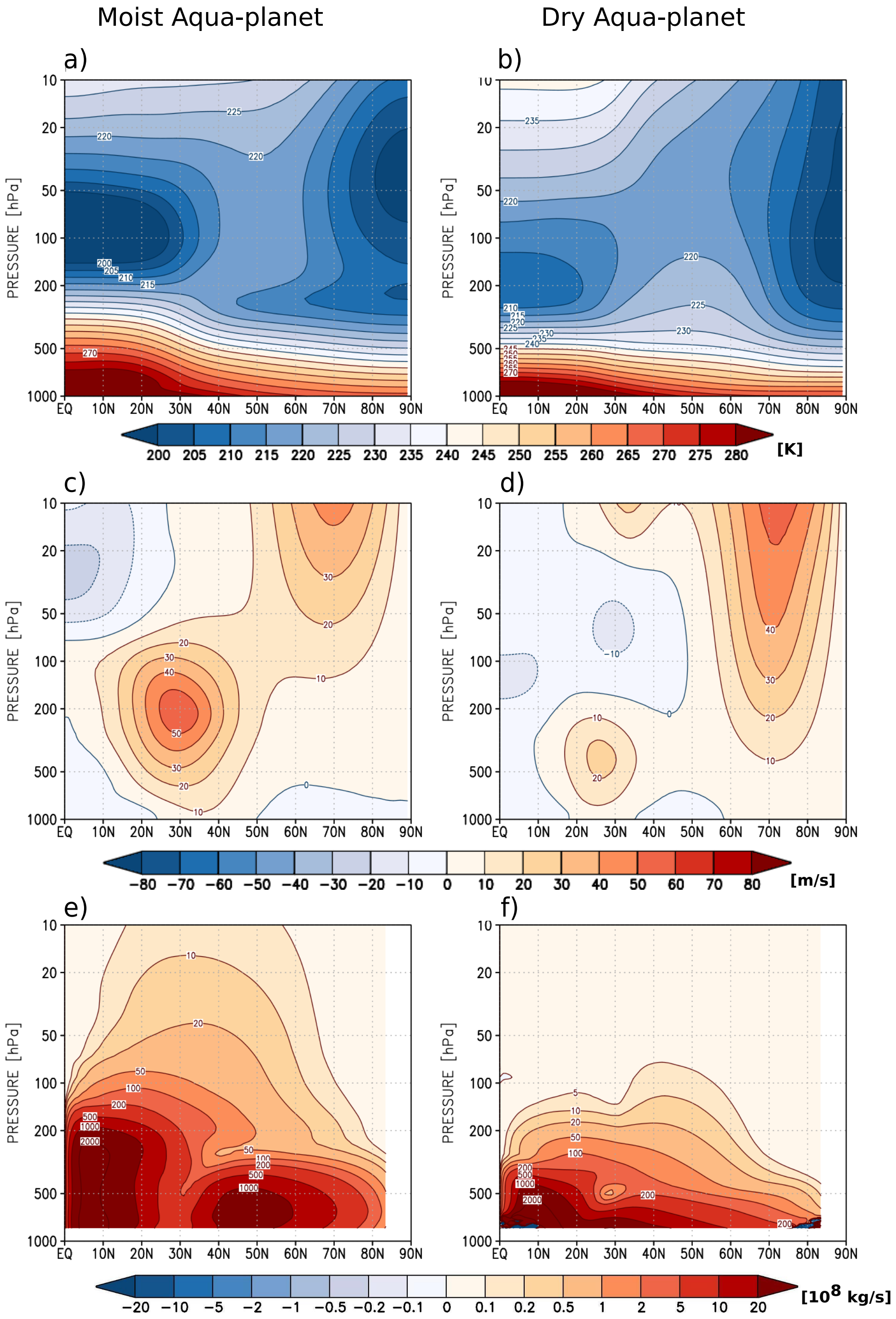

Figure 2.1. Basic state of the zonal mean temperature (a,b), the zonal mean zonal wind (c,d), and zonal mean stream function (e,f) shown for the MOIST-AP on the left and for the DRY-AP on the right.

the mid-latitude static stability and vertical wind shear and thereby through changes in the baroclinicity the eddy momentum convergence (Vallis, 2006).
The tropospheric impact of moisture on the circulation is illustrated in Figure 2.1. The left column of Figure 2.1 shows a standard APE which from now on is called MOIST-AP the right column shows a dry Aquaplanet (DRY-AP) in which simply the convection and cloud parametrization are turned off and no idealized thermal forcing is prescribed yet. Figure 2.1 a) and b) show the zonal mean temperature basic states, Figure 2.1 c) and d) the zonal mean zonal wind basic states and Figure 2.1 e) and f) the zonal mean meridional stream function basic states of both models. Due to the missing latent heating the upper tropical troposphere in Dry-AP is much cooler than in the Moist-AP. further, the tropopause region characterized by the reversal of the vertical temperature gradient shifts from approximately 100hPa in MOIST-AP to approximately 200hPa in DRY-AP. The Hadley cell turns into a dry shallow meridional circulation (Figure 2.1f) losing its deep branch and shifting the level of maximum angular momentum transport to lower atmospheric levels, which manifest in weaker super-rotation and therefore weaker subtropical westerlies (Figure 2.1d). Further, the tropospheric sub-tropical upper (at 250hPa) meridional temperature gradient is reduced in DRY-AP contributing to the weaker mid-latitude westerlies. The decrease in temperature in the tropical and subtropical troposphere favor baroclinic instabilities due to decreased stability more equator-ward in the DRY-AP than in MOIST-AP. Further, the decrease in the mid-latitude meridional temperature gradient in the DRY-APE reduces the zonal mean winds via the thermal wind relation and thereby reduces baroclinic instabilities through decreased vertical wind shear in the mid-latitudes. Both, process shift the eddy-driven jet toward the equator in the DRY-AP.
Therefore, when turning off convection and cloud parametrization as in Dry-AP additional tropospheric thermal forcing is necessary to capture a realistic vertical extent of the Hadley circulation and realistic mid-latitude dynamics.

In ICON-DRY a zonal uniform thermal forcing constant in time is prescribed to drive a realistic tropospheric general circulation. The thermal forcing is obtained from heating rates of the MOIST-AP. In the following the term $heatingrate$ is used to describe the outcome of the different Moist-AP parameterizations and the term thermal forcing is used to describe the function, that drives the ICON-DRY's atmosphere. In the following the relevant heating rates and their interactions are discussed in detail.
The effects of neglecting moist compounds can be classified in two process categories. The first category contains those processes, that simply disappear when switching off the moist compounds which are the latent heat flux and short wave radiation absorption due to the presence of liquid water and ice. The second category contains

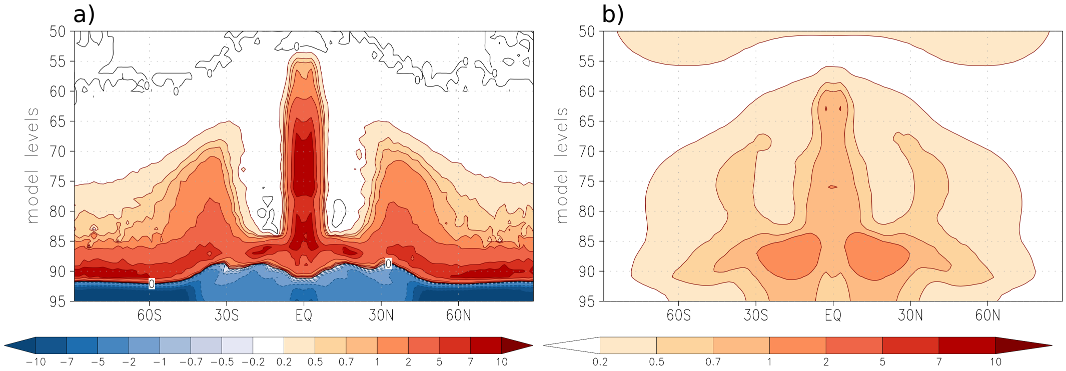

Figure 2.2. Heating rates due to the evaporative cooling and diabatic warming (a) and short wave radiation (b) in the MOIST-AP in K/day.

those processes, that adapt to the dry conditions such as the vertical diffusion including sensible heat flux and the long wave radiation.

The latent heat flux appears as negative and positive heating rates corresponding to diabatic cooling (evaporation) and diabatic warming (condensation), respectively. Figure 2.2a shows the basic state of the zonal mean heating rate due the convection and cloud parameterization of a two-year MOIST-AP experiment. The vertical levels are shown in model levels. Level 50 corresponds to approximately 150hPa. Since the heating rates are obtained in model levels and also the thermal forcing, later on, is calculated in model levels, model levels are shown instead of pressure levels. The near surface levels are cooled by evaporation and the atmospheric layers aloft are warmed by condensation. The basic state of the zonal mean heating rates due to short wave absorption is shown in Figure 2.2b. Large parts of the troposphere are heated up by about 0.5K/day.

If only the heating rates obtained from evaporative cooling, diabatic warming and short wave radiation absorption are considered in the thermal forcing for ICON-DRY the thermal forcing would lead to an unrealistic high temperature state. This is because the in the absence of moisture the long wave radiation capability of the atmosphere is lower since water vapor is an efficient absorber and emitter of terrestrial radiation, and also because in the boundary layer to some degree the sensible heat flux compensates the heating due to latent processes.

Figure 2.3b shows the time mean zonal mean of the heating rates due to long wave radiation in the DRY-AP. The MOIST-AP, which is shown in Figure 2.3a exhibits much greater negative heating rates due to long wave radiation. There are two process sequences involving long wave radiation, that are initiated when moist compounds are switched off; one process sequence, that relates to a temperature change due to a change in long wave radiation of all constituents and another process sequence, that relates to a change of the total emissivity of the atmosphere due to the absence of a constituent namely the water compounds.

The absence of water compounds account the most for the emission change. This

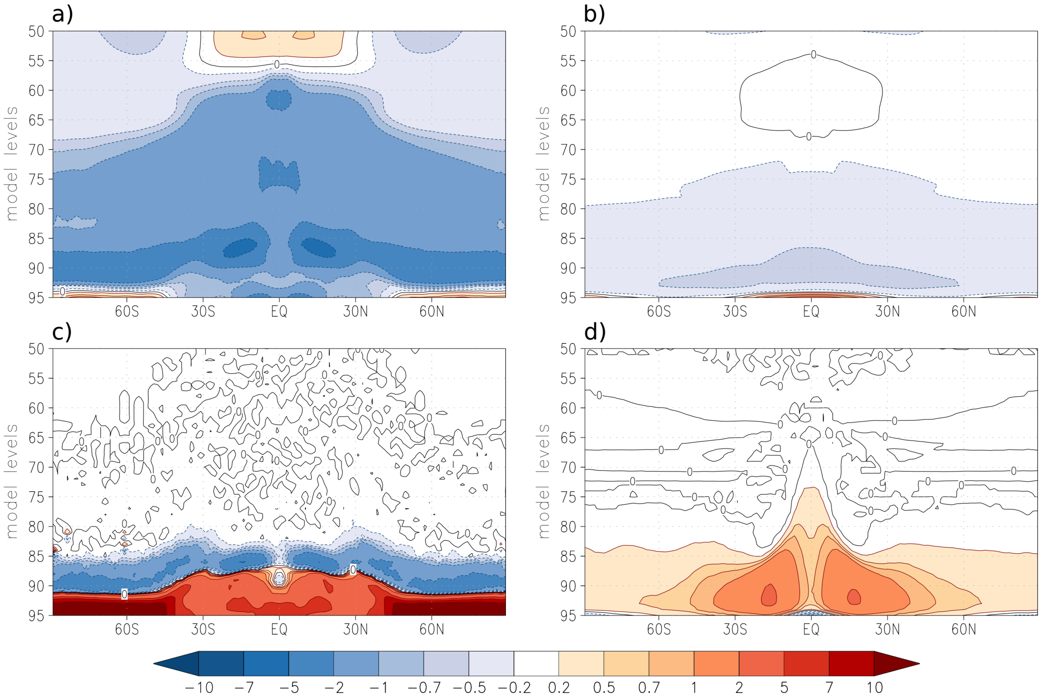

Figure 2.3. Heating rates due to long wave radiation in the MOIST-AP (a) and in the DRY-AP (b) in K/day. Heating rates due to vertical diffusion in MOIST-AP (a) and in DRY-AP (b) in K/day.

can be explained when considering Kirchhoff's law. The rate at which a body radiates thermal radiation is equal to the rate at which it absorbs thermal radiation. This is also true for any given wavelength. Hence, since it is known that nitrogen and oxygen are poor absorber for terrestrial radiation they are also poor emitter for terrestrial radiation. In MOIST-AP we only have water vapor and CO_2 as greenhouse gases. In DRY-AP we only retain CO_2 as greenhouse gases. Water vapor accounts for approximately two-thirds of the absorbed terrestrial radiation and is therefore by far the most important emitter for terrestrial radiation in the atmosphere. CO_2 only accounts for approximately one-third in our model configuration. Hence, the total change in long wave radiation is a combination of a long wave radiation reduction of about two-third due to the absence of water vapor and a long wave radiation reduction due to the temperature change, that is felt by the retained CO_2. The impact of the long wave radiation change of the CO_2 can only be maximal one-third, and as the temperature change is rather small the impact on the long wave radiation compared to the change initiated due to the absence of water vapor is very small. However, the latter is not important to consider in the thermal forcing because the long wave radiation which is felt by the CO_2 automatically adapts to the higher temperatures in ICON-DRY when prescribing the thermal forcing since the CO_2 is kept in ICON-DRY.

The Stefan-Boltzmann law is considered to illustrate the importance of taking into account the long wave radiation change due to the missing water vapor in the thermal forcing. For simplicity as a heat source only latent heating and as a constituent only water vapor and CO_2 are considered. The balance is then given by:

$$LH = \epsilon \sigma T^4 \tag{2.2}$$

where LH is the latent heating. The σ is the Stefan-Boltzmann constant and ϵ is the emissivity due to water vapor and CO_2. Any additional heating is balanced by an increase in emitted long wave radiation in both models the MOIST-APE and the DRY-AP. However, there is reduced emissivity in DRY-APE since there is no water vapor, which can be seen in the long wave radiation of DRY-AP (Figure 2.3b). When the emissivity is reduced but the additional heating is still the same ,consequently, the temperature needs to be higher to achieve equilibrium state (equation 2.2). Therefore, the difference between the long wave radiation heating rate of the Moist-AP and that of the DRY-AP needs to be considered in the thermal forcing of ICON-DRY. Note, that the greenhouse effect in our model is limited as we prescribe the lower boundary with fixed sea surface temperature, meaning that back radiation is not capable of heating the surface.

The vertical diffusion contains the subgrid- scale turbulent mixing processes, that includes latent heat flux and sensible heat flux. The diabatic heating due to the condensation is strongly linked to the turbulent mixing in the boundary layer as the latter provides the latent heat flux. In other words, turbulent mixing brings the water vapor to the level where it condensates and heats the atmosphere. Prescribing the diabatic processes related to condensation in ICON-DRY means taking into account indirectly the latent heat flux as described above but not the sensible heat flux.

In the MOIST-AP the sensible heat flux (Figure 2.3c) counteracts the heating rates due evaporation and condensation (Figure 2.2a) in the boundary layer. By comparing both figures it is obvious, that within the boundary layer the latent heat flux and sensible heat flux are strongly linked. Hence, when considering the latent heating in the boundary layer one needs to consider the sensible heat flux as well. In DRY-APE the sensible heat flux (Figure 2.3d) mainly counteracts the atmospheric cooling due to long wave radiation. Since it is still present in APE-DRY the residual heating rate, which is the difference between the vertical diffusion of Moist-APE and the DRY-APE is considered in the thermal forcing for ICON-DRY in order to account for the turbulent mixing process.

The processes, that disappear can be easily substituted in ICON-DRY by implementing simply the respective heating rates from MOIST-AP. The technical procedure of

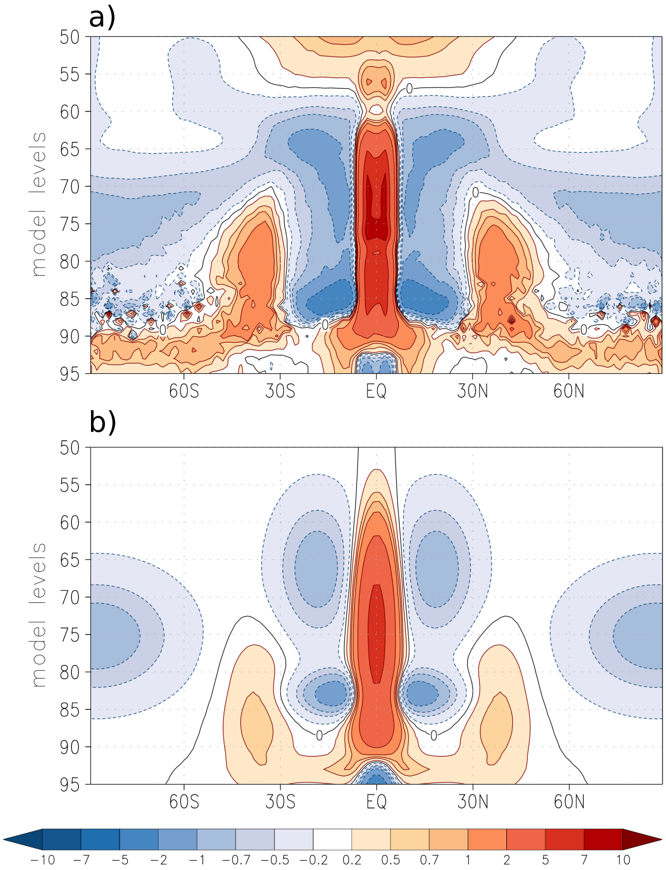

Figure 2.4. Sum of the heating rates due to evaporative cooling and diabatic warming, the water vapour related long wave radiation, the vertical diffusion difference and tropospheric short wave radiation in K/day (a). The tuned thermal forcing is shown in K/day in (b).

implementing the heating rates are explained in the following section. However, the processes, that only adapt to the dry conditions require calculations of differences between the MOIST-AP and the DRY-AP. Note, that taking into account the difference in heating rates between two basic states might not be the ideal solution since many processes in the atmosphere are non-linear and therefore do not simply add up. Given this caveat tuning of the function is necessary. In order to obtain the thermal forcing of ICON-DRY, we sum up the heating rates due to latent heating and cooling, tropospheric short wave radiation absorption, long wave radiation related to water vapor and vertical diffusion residual. Figure 2.4a shows the zonal mean sum of all heating rates.

2.1.5 Implementation of Thermal Forcing

In ICON-DRY a simplified function is implemented, that is a best fit to the obtained heating rates of the Moist-AP. The function provides the opportunity to adjust certain heating and cooling aspects. The best fit is performed on zonal mean heating rates averaged over the last 2 years of a 3-year MOIST-AP experiments. The best fit function consists of bivariate Gaussian distributed functions of the form:

$$f(y_i, z_j) = exp\left(- \left(\frac{(y_i - y_0)^2}{2\sigma_y^2} + \frac{(z_j - z_0)^2}{2\sigma_z^2} \right) \right) A_0 \tag{2.3}$$

where y_i and z_j are the normalized latitudes and model levels, i and j the indexes of the function, y_0 and z_0 determine the normalized position of the function center, the σ the spatial extension of the function and A_0 the amplitude of the function. The latitudes are normalized accordingly to:

$$y_i = \frac{(\phi_k + \frac{\pi}{2})}{\pi};\ y_i \Big| \Big\{ 0 \leq\ y_i \leq\ 1 \Big\};\ \phi_k \Big| \Big\{ -\frac{\pi}{2} \leq\ \phi_k \leq\ \frac{\pi}{2} \Big\} \tag{2.4}$$

where ϕ_k are the latitudes in radiant. The transformation to normalized vertical coordinates is done with the following equation:

$$z_j = \frac{n_l - 1}{n_{max} - 1};\ z_j \Big| \Big\{ 0 \leq\ z_j \leq\ 1 \Big\};\ \ n_l \Big| \Big\{ 1 \leq\ n_l \leq\ 95 \Big\} \tag{2.5}$$

where n_l are the model levels. n_{max} is the total number of levels which is in our case 95. In principle the best fit function can be applied to any horizontal resolution. However one needs to be careful since the respective moist experiment at a different horizontal resolution might respond differently. Therefore, when constructing dry models the best fit function must be obtained from a moist model, that has the same resolution as the dry model to which the best fit function is applied to. The vertical model levels are non- uniformly distributed and therefore require a recalculation whenever the vertical resolution is changed.

The total number of bivariate Gaussian functions used for finding the thermal forcing may depend on the goal. This approach is a result of seeking a function which is a good fit to the data but at the same time is not too complex. So choosing the number of functions enables to have some control over the complexity. An iterative process is used in which at each iteration step a new Gaussian function is obtained. The number of iterations therefore is equal to the chosen number of Gaussian functions. First, the algorithm calculates the hemispheric mean in order to get a perfect hemispherical symmetric distribution. This is to prevent asymmetric results. This only accounts for equinox conditions. In the second step it smooths the data and detects the position of the maximum absolute value. This value can either be positive or negative and therefore it checks the sign and gets the amplitude of the maximum from the non-smoothed data. We use the amplitude from the non-smoothed data, because smoothing results in a decrease of the amplitude and we want to have a function, that resembles the maximum forcing well. Afterward, a best fit loop over the extensions coefficients σ is performed to get the first best fit bivariate Gaussian function. This function then is subtracted from the data. The new data is used to repeat the procedure for a given number of times. The smoothing of the data is especially crucial after subtracting several functions from the original data as the data becomes more and more noisy. We use 16 bivariate Gaussian functions to obtain the thermal forcing.

In the last step a range of sensitivity experiments have been performed in which the amplitude of the mid-latitude thermal forcing has been slightly adjusted. It has been found, that the mid-latitude temperature gradient is sensitive to the prescribed thermal forcing in the mid-latitudes and that the amplitude of the mid-latitude thermal forcing is to high leading to too high temperature. This too high temperature results in a weak meridional temperature gradient at 40°N/S and a strong meridional temperature gradient at 60°N/S. The reason for that originates in the fact, that the thermal forcing does not cover the negative heating rates between 60°N/S and 30°N/S at model level 60 to 70. Therefore, the amplitude of the thermal forcing in the mid-latitudes is reduced in order to achieve a realistic temperature profile. Figure 2.4b shows the best fit function, which is thermal forcing that drives the ICON-DRY large scale circulation. It can be compared to the zonal mean sum of all heating rates (Figure 2.4a). Further evaluation of the ICON-DRY model basic state can be found in the last section of this chapter.

2.2 Experimental Setups

2.2.1 Control Configurations

The ICON-DRY in its default control configuration consists of a flat surface without non-orographic gravity wave parametrization, and is named DF. The meaning of the different acronyms are listed in Table 2.1. Additional control configurations are constructed in which we include non-orographic gravity wave parameterization ($D_{gw}F$) or idealized orographic forcing. The idealized orographic forcing is prescribed in terms of sinusoidal perturbations in the surface geopotential height, hence introducing water mountains and water valleys of the form:

$$\Delta Z_g(\phi_i, \lambda_j) = \sin(2\phi_j)^4(\sin(\lambda_i)n)A \tag{2.6}$$

Table 2.1. Explanation of acronyms

Acronym	Explanation
D	Dry atmosphere
D_{gw}	Dry atmosphere with non-orographical gravity wave parameterization
M	Moist atmosphere
D_j	Dry atmosphere with eddy driven jet position as in M
F	Flat surface
$W1_x$	Prescribed wavenumber 1 at 45°N/S (implemented as surface geopotential height anomaly with certain amplitude, e.g $W1_{600}$
$W2_x$	Prescribed wavenumber 2 at 45°N/S (implemented as surface geopotential height anomaly with certain amplitude, e.g $W1_{600}$
T	Tropical amplification (anomalous heating rate, only for dry atmosphere)
4K	4K uniformly increased SSTs (only for moist atmosphere)
S	Stratospheric CO_2 cooling (quadrupled CO_2 concentration)
P_H	Polar amplification as thermal forcing (zonally symmetric and asymmetric tropospheric anomalous heating rate at 70°N/S)

where ϕ_i and λ_j are the latitudes and longitudes, respectively, n the zonal wave number and A the amplitude of the wave in meter. The latitudinal position of the wave is controlled by the first sine function. A wave number 1 anomaly ($DW1_x$) or a wavenumber 2 anomaly ($DW2_x$) at 45°N/S is prescribed with different surface amplitudes (x=200m, x=400m, x=600m, x=800m). There is further a configuration, that includes both a stationary wavenumber 1 and a wavenumber 2 with an amplitude of 600m ($DW1W2_{600}$). The function is given by:

$$\Delta Z_g(\phi_i, \lambda_j) = \left[\sin(2\phi_j)^4(\sin(\lambda_i)n_1)A\right] + \left[\sin(2\phi_j)^4(\sin(\lambda_i)n_2)A\right] \tag{2.7}$$

where n_1 = 1, n_2= 2 and A=600m. Finally, also the Moist-AP is considered and named M. Since, the MOIST-AP reveals a different position of the the eddy driven jet a ICON-DRY configuration is constructed in which the eddy-driven jet position is similar to the MOIST-AP's jet position. It is named D_j.

2.2.2 Sensitivity Experiments

The sensitivity experiments are performed by prescribing additional idealized thermal forcing which resembles the characteristic feature of global warming rates. We test the dynamical responses to Tropical amplification (TA) and Arctic amplification (AA) in the troposphere. Moreover, the CO_2 concentrations is quadrupled to test the dynamical response to CO_2 induced stratopause cooling (SC).

A detailed description of the different additional thermal forcing can be found in Figure 2.5. A list of the different forcing abbreviations can be found in table 2.1. The TA is an imposed zonally symmetric thermal forcing anomaly as shown in color shading for the DFT experiment in Figure 2.5a. Contour lines show the thermal forcing, that drives the control experiment (DF). The additional thermal forcing is skewed in the vertical with a maximum at 250hPa and a magnitude of about 0.5K/day. It differs from most other dynamical core studies (e.g Butler et al., 2010; Eichelberger and Hartmann, 2005) since it is constrained to a narrow equatorial band. Given the thermal forcing of the control experiments ICON-DRY provides the opportunity of superimposing additional thermal forcing and letting the circulation distribute the heat. This approach, therefore, gives a solution to the concerns, that prescribing a broad thermal forcing may impact artificially the mid-latitude baroclinicity.

Since the amplification of polar near surface air temperature in the real atmosphere mainly occurs in the arctic the term arctic amplification is used in literature. Since the additional thermal forcing is prescribed in both hemispheres technically the term polar amplification (PA) is more appropriate in this study. The PA is prescribed as zonally symmetric thermal forcing (Figure 2.5b) and as zonally asymmetric thermal forcing spanning 180°N/S (Figure 2.5c) and 90°N/S (Figure 2.5d).The zonally symmetric thermal forcing is not centered at the pole to represent heating along the arctic sea ice edge. All additional PA forcing are prescribed at 70°N/S with an meridional extension of approximately +-15 degrees.

For each of the configurations considered, we have an unperturbed control and a sensitivity experiment where the considered sensitivity forcing is included. In the case of the sensitivity experiments the acronym of the considered forcing is attached to the control experiments acronym (e.g DFT: Dry flat surface forced with TA).The mean differences of the sensitivity to the control experiments are marked with a Δ in front of the acronym. For example ΔDFT is the mean difference of the sensitivity experiment including tropical thermal forcing minus its respective control experiment on a flat surface. Thus, ΔDFT reports only on mean changes due to tropical amplification on dry transient waves and mean circulation, which means, that radiative cooling of the stratosphere changes, surface baroclinicity (SSTs are fixed) and explicit changes in extra-tropical stability are excluded. By comparing the ΔDFT with the $\Delta DW1_xT$ we can

TROPICAL AMPLIFICATION

Long. Extent 360°
Hemispherical symmetric
Height Maximum: 250hPA
Amplitude: ~0.5K/day

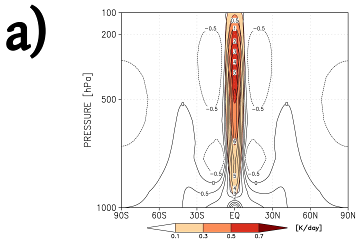

POLAR AMPLIFICATION

SYMMETRIC THERMAL FORCING
Long. Extent 360°
Lat. Maximum 70°N/S
Height Maximum: 950hPA
Amplitude: ~0.25K/day
Combined with SST increase

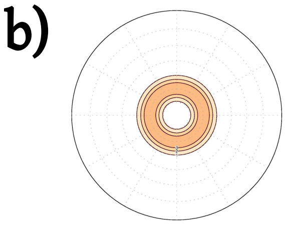

ASYMMETRIC THERMAL FORCING
Long. Extent 180°
Lat. Maximum 70°N/S
Height Maximum: 950hPA
Amplitude: ~0.5K/day
Combined with SST increase

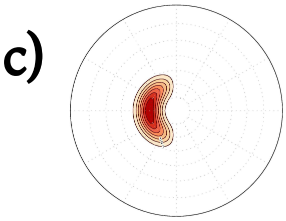

ASYMMETRIC THERMAL FORCING
Long. Extent 90°
Lat. Maximum 70°N/S
Height Maximum: 950hPA
Amplitude: ~0.5K/day
Combined with SST increase

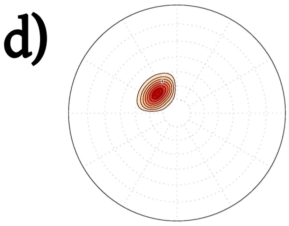

Polar sereographical projection
between 90°N/S and 20°N/S

CO2 INDUCED STRATOPAUSE COOLING

4x CO_2 increase
no change in SST
no water vapour feedback

Figure 2.5. Information and figure on the additional thermal forcing in ICON-DRY. Tropical amplification is shown in pressure - latitude plane in a), symmetric polar amplification is shown in a polar-stereographic projection in b), asymmetric polar amplification spanning 180° and 90° in longitude are shown in c) and d) respectively.

report on the role of the idealized orography in the response to TA or PA.

The CO_2 induced stratosphere cooling is achieved by quadrupling the CO_2 concentrations. Because of the dry conditions and the fixed SST the focus lies on the stratospheric circulation change.

The data is put out in pressure coordinates. All experiments are integrated for 2880 days. The first 360 days are considered as spin up and are excluded from the analysis. In order to calculate fluxes the data is written out 6 hourly. Statistical significance is computed using 30 day means

2.3 Validation of the Control Configurations

In this section the ICON-DRY control configuration DF is tested regarding its equilibration. Further, all control configuration are investigated regarding their low-frequency variability and their hemispherical correlation. Finally, the DF and $DW1_{600}$ mean states are classified with respect to the ERA-Interim climatology.

2.3.1 Equilibration

The thermal forcing, that drive the ICON-DRY atmosphere heats up the atmosphere. The heating is counterbalanced by long wave radiation and to a small degree also by negative surface fluxes (fixed SSTs). In this section it is shown, that the ICON-DRY model equilibrates.

The temperature tendency gives an estimate of whether the atmosphere is thermodynamically balanced. In case of a thermodynamically balanced atmosphere the total temperature tendency would be zero. However, mathematically this is only true for the number of time instants (N) going towards infinity. Technically, any experiment is a sample meaning the number of time instants N are finite leading to a total atmospheric temperature tendency unequal to zero because of internal variability. Nevertheless, the total temperature tendency is expected to be small for even only a 7 years simulation, since ICON-DRY consists of much less complexity than the real atmosphere and the experiments is performed at perpetual equinox condition.

The temperature tendency is calculated from the temporal changes of the temperature and therefore given by:

$$T_{tend} \widehat{=} \frac{\Delta T}{\Delta t} = T_{t+1} - T_t \tag{2.8}$$

where the Δ denotes a finite time increment which in this case is daily.

The ICON-DRY Model's tropospheric temperature tendency is depicted in Figure 2.6 as the daily temporal evolution of the horizontal and vertically pressure weighted mean temperature tendency. The temporal evolution includes the spin up phase (red line) in order to provide a visual impression on the variance of the data (black line). We estimate whether the simulation is equilibrated by calculating a signal to noise ration (SNR) which is given by

$$SNR = \frac{\mu}{\sigma} \tag{2.9}$$

where the μ is the mean tendency in space and time and σ the standard deviation of the daily time series shown in Figure 2.6 excluding spin up. We find μ = 3.12*10^{-5}K/day and σ = 4.3*10^{-3}K/day which results in a SNR of 7.3*10^{-3} meaning the signal is 3 orders of magnitude smaller than the noise, suggesting there is no signal (no trend) and the mean is only different from zero because N is limited. Further, the mean is also a few orders of magnitude smaller than the physical thermal forcing. This strongly suggest, that the *DF* experiment is equilibrated.

2.3.2 Low-Frequency Variability

Depending on the horizontal and vertical resolution and the mean state of the atmosphere Gerber et al. (2008) have shown, that idealized model such as the Held-Suarez model may consists of unrealistic large low-frequency variability. They further point out, that those models, that consist of unrealistic low-frequency variability show an increased amplitude of the model's response to external forcing. Therefore, the ICON-DRY Control configurations' low frequency variability need to be quantified in order to judge on the amplitude of the model's response to external forcing.

Following Gerber et al. (2008) the ICON-DRY model's low-frequency variability is calculated by the use of the annular mode auto-correlation function. The annular mode is defined as the leading mode of atmospheric variability. The leading mode is calculated by the use of a singular value decomposition. It calculates a principle component time series and an associated empirical orthogonal function (EOF) pattern. The procedure is applied to the troposphere and the stratosphere. Since Baldwin and Thompson (2009) have shown, that averaging the variable zonally before calculating the EOF leads to equivalent results zonnally averaged input data is used. The tropospheric annular mode is defined by the first EOF of the zonally averaged lowermost geopotential height. The same applies for the stratospheric annular mode, except that geopotential height data at 10hPa is used. The decorrelation time scale of the annular mode is defined as the time of the principle component time series auto-correlation function being equal to the e-folding time scale τ:

$$\tau = \frac{1}{e} \approx 0.37 \tag{2.10}$$

with e being the Euler's number. The uncertainty of the decorrelation time scale is estimated by

$$std(\tau_N) \approx k\tau^{3/2}N^{-1/2} \tag{2.11}$$

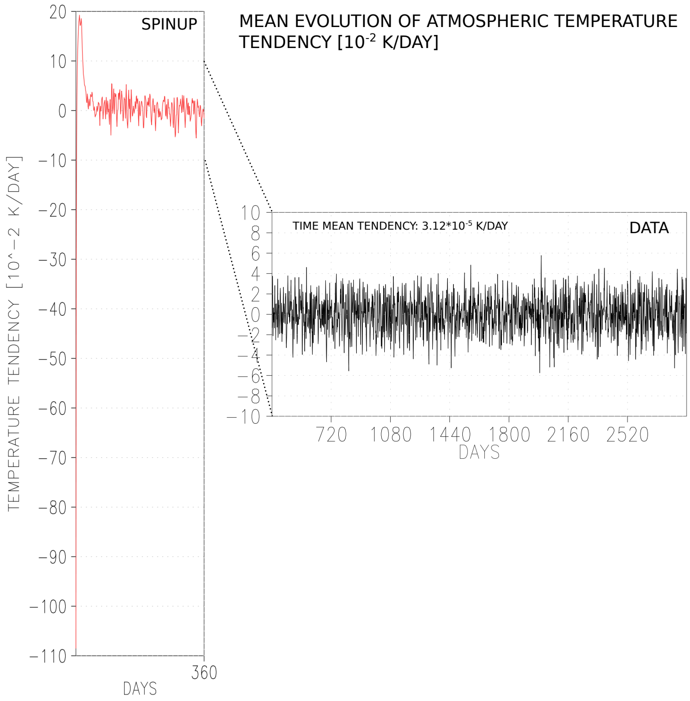

Figure 2.6. Domain mean temperature tendency evolution of the ICON-DRY's DF control experiment. The red line shows the spinup phase and the black line the data

where N is the sample size, τ the decorrelation time scale. k is given by

$$k \approx e(1-3e^{-2})^{(1/2)}. \tag{2.12}$$

A derivation of the equations can be found in the appendix of Gerber et al. (2008). Table 2.2 shows the decorrelation time-scales and the estimated uncertainty for the control configurations. The experiments with larger stationary wave amplitudes tend to show reduced time-scales. The tropospheric and stratospheric decorrelation time-scales reflect a realistic behavior, according to Gerber et al. (2008).

2.3.3 Hemispheric Correlation

The degree of hemispherical independence is of particular interest since given equinox condition a low correlation between both hemispheres provides the opportunity of doubling the data by simply considering both hemispheres as two independent integration periods of the same experiment

The correlation coefficient (r-value) and the significance of the correlation (p-value) is calculated between the Northern and the southern hemisphere as follow. Two time series of the zonal mean zonal wind at 10hPa are used; one at 60°N and the other at 60°S. Given a decorrelation time scale much below 90 days (section 2.4.2) in all control

Table 2.2. Decorrelation time-scales τ and estimated uncertainty std(τ_N) of tropospheric and stratospheric annular modes in ICON-DRY control experiments

Control experiment	Troposphere	Stratosphere
DFS	43 ± 5.34	79 ± 13.31
$DW1_{200}$	65 ± 9.93	56 ± 7.94
$DW1_{400}$	38 ± 4.44	47 ± 6.11
$DW1_{600}$	33 ± 3.59	34 ± 3.76
$DW1_{800}$	32 ± 3.43	28 ± 2.81
$DW2_{200}$	26 ± 2.51	64 ± 9.71
$DW2_{400}$	32 ± 3.43	46 ± 5.91
$DW2_{600}$	33 ± 3.59	35 ± 3.96
$DW2_{800}$	42 ± 5.16	27 ± 2.66
$DW1W2_{600}$	26 ± 2.51	22 ± 1.96

configurations ,for simplicity, 90 day chunks are consider to calculate the correlation between both hemisphere.

In Table 2.3 we show the r-value and p-value for all ICON-DRY control configurations. In all control configurations, correlations lower than 0.38 are found. Further, the p-values reveal no statistical significance considering a significance level of 0.05 (5%) except for the $DW1W2_{600}$ which has a p-value slightly below the significance level. However, the r-value of $DW1W2_{600}$ is the very small (r-value = -0.01). Therefore, there is no significant correlation between the both hemispheres in any control configuration enabling the use of both hemispheres in analysis.

2.3.4 Classification of the ICON-DRY's Atmosphere by Means of ERA-Interim Reanalysis

The European Centre for Medium-Range Weather Forecasts reanalysis data ERA-Interim is used to classify the mean state of the control configurations. The atmospheric stationary wave of those experiments with idealized orography are evaluated. Further, all control configurations' polar vortex strength are compared to the seasonal evolutions of the ERA-Interim Northern and Southern hemisphere stratospheric polar night jets. The comparison aims at classifying the ICON-DRY model in its capability of reproducing the key atmospheric large-scale phenomena, that are of interest in this study.

Table 2.3. Correlation coefficients (r-value) and its statistical significance (p-value) for the ICON-DRY control experiments.

Control experiment	r-value	p-value
DFS	0.17	0.14
$DW1_{200}$	0.25	0.09
$DW1_{400}$	0.11	0.14
$DW1_{600}$	- 0.05	0.1
$DW1_{800}$	0.37	0.07
$DW2_{200}$	0.2	0.09
$DW2_{400}$	0.19	0.09
$DW2_{600}$	0.2	0.13
$DW2_{800}$	0.34	0.1
$DW1W2_{600}$	- 0.01	0.046

2.3.4.1 Stationery Waves

The stationary waves in ICON-DRY are triggered via surface geopotential height anomalies of different amplitudes as described in subsection 2.2.1. The resulting atmospheric stationary waves are obtained by decomposing the basic state of the geopotential height field into wave number 1 and wave number 2. The decomposition is performed using a band pass filter. First the data is transformed into spectral space using a Fourier transformation. After filtering the specific wavenumber the data is inverse transformed. Figure 2.7 shows the decomposed stationary wave number 1 and 2 geopotential height at 500hPa averaged (latitude weighted) between 30°N/S and 70°N/S for different prescribed surface anomalies of the $DW1_x$ control configurations in the upper row and of the $DW2_x$ configuration in the bottom row.

In general, increased prescribed amplitudes in the surface geopotential means increased stationary wave amplitudes in the free atmosphere. This applies to a forced stationary wave 1 (Figure 2.7a) and for the forced stationary wave 2 (Figure 2.7d). However, the relationship between the prescribed surface amplitude and the resulting atmospheric amplitude is found to be non-linear, illustrated by the reduced increase in atmospheric amplitudes for steadily increased surface amplitudes. In, fact going from a prescribed surface amplitude of 600m to an amplitude of 800m hardly impact the atmospheric amplitude at 500hPa at all.

The reason for that may be found in a downscale energy cascade. The amplitude of the stationary wave number 2 at 500hPa of the $DW1_x$ is non-linear in relation to the prescribed surface amplitude. However, in contrast to stationary wave number

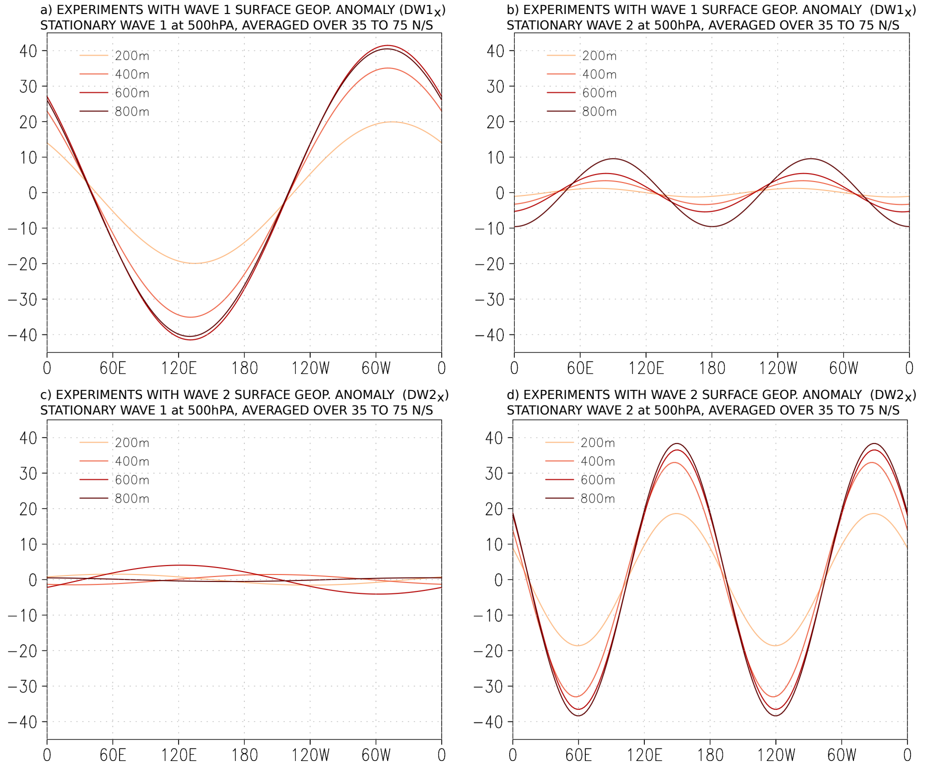

Figure 2.7. Stationary wave amplitudes at 500hPa for different surface geopotential height anomalies. a) and b) show control experiments with a forced stationary wave number 1. c) and d) show control experiments with a forced stationary wave number 2. The left column shows the filtered stationary wave number 1 and the right column the filtered stationary wave number 2.

1 (Figure 2.7a) the atmospheric amplitudes amplify for steadily (Δ 200m) increased surface amplitudes. Especially, in case of $DW1_{800}$ energy transfer to wave number 2 is found. In case of the $DW2_x$ experiment we find an upscale energy cascade to stationary wave number 1(Figure 2.7c). However, the amplitude are small. Given that the $DW2_{800}$ stationary wave 1 amplitude is smaller than the $DW2_{600}$ amplitude and given both have similar stationary wave 2 amplitudes, there is also an downscale energy transfer to stationary wave 3.

Figure 2.8 compares the $DW1_{600}$'s 500hPa stationary wave 1 and the $DW2_{600}$'s 500hPa stationary wave 2 to the Northern hemisphere 1970-2012 November to March mean ERA-Interim stationary wave 1 and wave 2. The plots are shown in a polar stereographical projection. The red (blue) cross mark the position of the prescribed maximum (minimum) surface geopotential anomaly. Shown are configurations with prescribed amplitudes of 600m as those amplitudes lead to free atmospheric amplitudes similar to the reanalysis.

The stationary wave 1 spatial pattern of $DW1_{600}$ (Figure 2.8a) resembles the stationary wave 1 pattern in the reanalysis well (Figure 2.8b). The stationary wave 2 pattern in

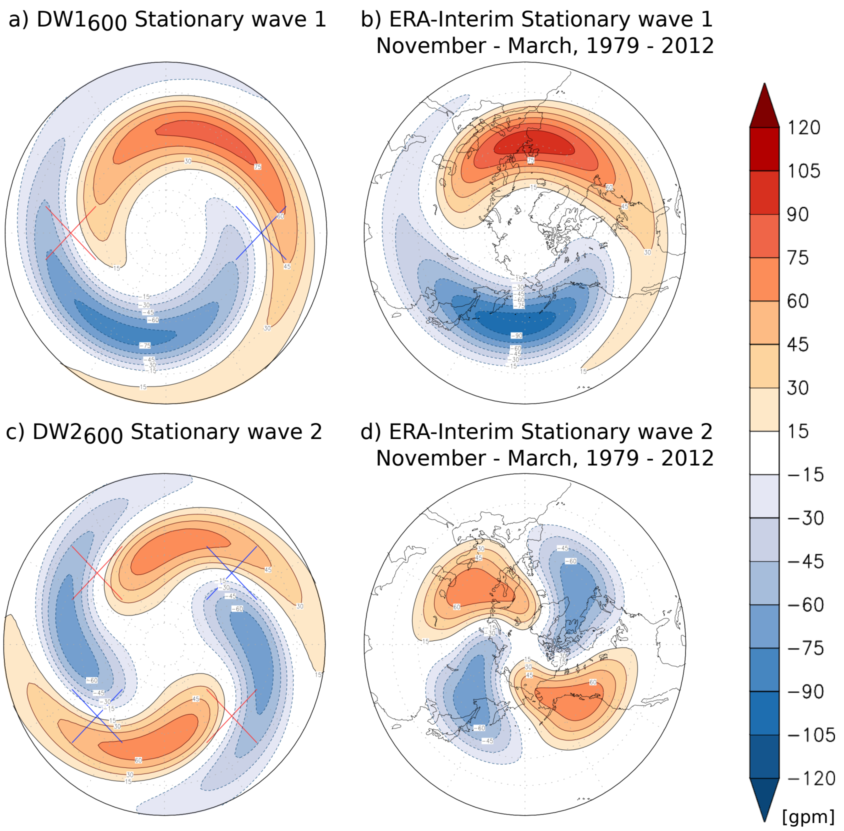
a) DW1600 Stationary wave 1
b) ERA-Interim Stationary wave 1
November - March, 1979 - 2012
c) DW2600 Stationary wave 2
d) ERA-Interim Stationary wave 2
November - March, 1979 - 2012
120
105
90
75
60
45
30
15
−15
−30
−45
−60
−75
−90
−105
−120
[gpm]

Figure 2.8. Polar stereographic plot of the filtered stationary wavenumber 1 (upper row) and stationary wave number 2 (bottom row) at 500hPa. a) shows the $\mathrm{DW1}_{600}$ control experiments and c) the $\mathrm{DW2}_{600}$ control experiments. b) and d) show ERA-Interim Northern hemisphere stationary waves. Red crosses denote maxima and blue crosses minima of the sinusoidal anomaly in the geopotential height.

the reanalysis (Figure 2.8d), however, looks differently from the stationary wave 2 pattern in the $\mathrm{DW2}_{600}$ (Figure 2.8c). The shape of the stationary wave 2 pattern in the reanalysis is more confined to higher latitudes whereas the shape of the stationary wave 2 pattern in the $\mathrm{DW2}_{600}$ is more elongated towards the subtropics and looks similar to the stationary wave 1 shape of both the reanalysis and the $\mathrm{DW1}_{600}$.

The downscale energy cascade may be an explanation for the pattern difference. Given that stationary wave number 1 is the largest possible wave number it is only affected by upscale energy transfer but is not affected by downscale energy transfer. This restriction applies to both the the model and the reanalysis. However, stationary wave 2 can receive energy due to both upscale and downscale energy transfer if stationary wave forcing at higher or lower wave number exist. This is true in the reanalysis, but is not true in the $\mathrm{DW2}_{600}$ control configuration where only a stationary wave number 2 is forced. The stationary wave number 2 in the $\mathrm{DW2}_{600}$ may lead to a stationary wave number 1 due to upscale energy transfer as can be seen in Figure 2.7c and to

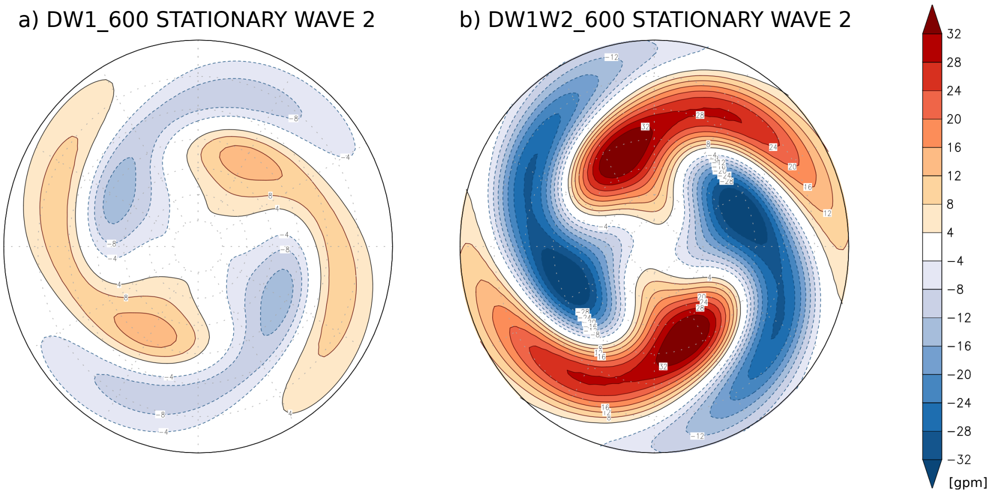

Figure 2.9. Polar stereographic plot of the filtered stationary wavenumber 2 at 500hPa for a)the DW1_{600} control experiments and b) the DW1DW2_{600} control experiments.

stationary wave number 3 due to downscale energy transfer, but it does not receive any from other forced stationary waves. Figure 2.9 illustrated, that the downscale energy transfer may provide an answer to the difference in the stationary wave number 2 pattern in Figure 2.8. It shows the stationary wave number 2 of the DW1_{600} control configuration in Figure 2.9a. The Figure is comparable to the line plot of Figure 2.7b (600m amplitude). In the DW1_{600} only a stationary wave number 1 is forced, hence the stationary wave number 2 is generated due to downs-scale energy transfer. This stationary wave number 2 is characterized by two maxima, a low latitude one and a high latitude one. The maximum at the high latitudes is larger than the one at the lower latitudes. The shape of the high latitude maximum resembles the shape, that is found in the reanalysis. A similar stationary wave 2 pattern is found in the DW1W2_{600} (Figure 2.9b) underpinning, that the stationary wave 2 pattern of the reanalysis is influenced by a down-scale energy cascade.

Given an idealized set up with prescribed sinusoidal surface anomalies and given, that the stationary wave forcing in the the reanalysis is much more complex the idealized set up reproduces the principle signatures of stationary waves very well. The control configurations are, therefore, suitable to study the role of stationary waves in the response to external forcing.

2.3.4.2 Tropospheric and Stratospheric Mean State

The DF control configuration's basic state is compared to the Southern hemisphere September mean basic state (1979 - 2012) of ERA-Interim reanalysis data. The Southern hemisphere is used since it consists of much less stationary waves than the Northern hemisphere. Austral equinox (September) has been chosen since ICON-DRY is configured for equinox conditions.

The basic state of the momentum flux together with the basic state of the zonal wind

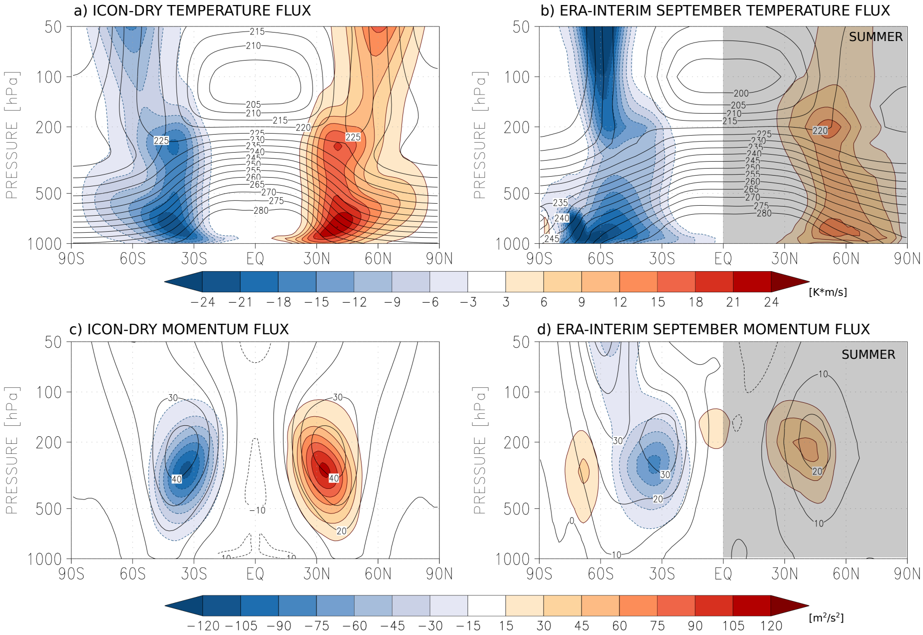

Figure 2.10. The upper row shows the time mean of the temperature flux together with the time mean of the temperature. The bottom row shows the time mean of the momentum flux together with the time mean zonal mean wind for a) and c) the DF control experiment and for b) and c) September ERA-Interim reanalysis. The Northern hemisphere is masked with a gray shading since the DC control experiment is more comparable to the southern hemisphere in terms of orography.

and the basic state of the temperature flux together with the basic state of the temperature are considered.

Figure 2.10a shows the time mean zonal mean temperature and time mean zonal mean temperature of the DF control configuration. Figure 2.10b the same variables for the reanalysis data. The northern hemisphere is masked with a transparent grey shading because no stratospheric westerly vortex exist in September in the northern hemisphere and hence neither stratospheric planetary wave propagation. The basic state of the temperature in ICON-DRY resembles the reanalysis data well showing similar heights of the tropical tropopause (at around 100hPa) and showing similar vertical tropical temperature profiles. The tropospheric temperature flux in ICON-DRY and the reanalysis show both maxima in the baroclinic active region. Also the momentum flux and the zonal winds reveal realistic mean basic states showing subtropical jet maxima at around 200hPa 30°N/S and the momentum flux maxima at around 300hPa.

Difference in the temperature flux between the ICON-DRY and the reanalysis emerge in the lower tropospheric polar region which can be explained by the presence of orography (Antarctica) in the reanalysis. Given the differences in the surface properties, naturally, difference in wave propagation and wave dissipation exits accounting for differences in the stratospheric polar vortex seen by comparing Figure 2.10c with 2.10d. In the real atmosphere the stratospheric stationary wave forcing between the Northern and southern hemisphere is different due to differences in the distributions of SSTs and orography. Figure 2.11 shows the climatological seasonal evolution of the zonal winds obtained from ERA-Interim data (1979-2012). The zonal winds are much weaker during boreal winter than during austral winter since the Northern hemisphere consists of much higher stationary wave forcing than the southern hemisphere. The strength of the stratospheric polar vortex of the DF (flat surface) and the DW1$_{600}$ (orography) control configurations are therefore compared to Southern hemisphere and Northern hemisphere monthly ERA-Interim polar vortexes, respectively.

a) ERA-INTERIM MONTHLY MEAN ZONAL WIND 1979 -2012

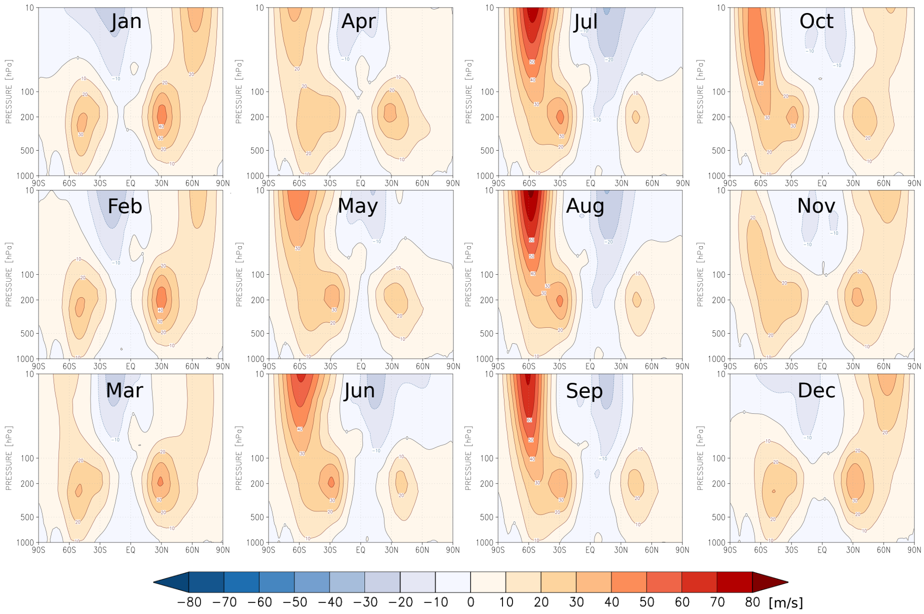

b) Comparison DFC to ERA-Interim Oct, SH

c) Comparison Dw1$_{600}$C to ERA-Interim Feb, NH

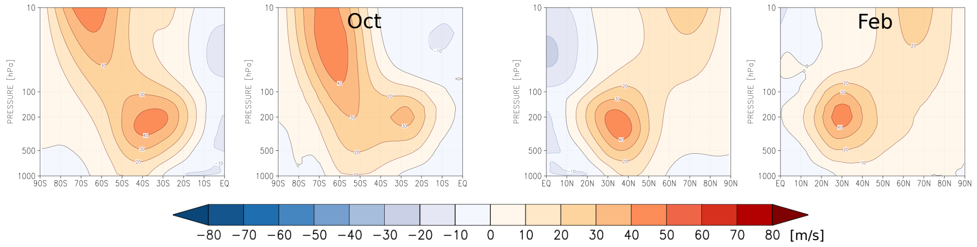

Figure 2.11. Seasonal evolution of the climatological (1979 to 2012) zonal mean zonal wind for ERA-Interim shown in a). Comparison between the time mean zonal mean zonal wind of the DF and the southern hemisphere October ERA-Interim time mean zonal mean zonal wind is shown in b). Comparison between the time mean zonal mean zonal wind of the DFW1$_{600}$ and the Northern hemisphere February ERA-Interim time mean zonal mean zonal wind is shown in c)

The DF control configuration compares best with the October mean Southern hemisphere polar vortex (Figure 2.11b) and the $DW1_{600}$ with the February Northern hemisphere polar vortex (Figure 2.11c). The strength of the polar vortexes in the control configuration therefore fit into the range of stratospheric polar vortex strengths observed in reanalysis.

The control configuration resembles reasonably well the mean large-scale atmospheric circulation of the in ERA-Interim reanalysis data. The ICON-DRY control configurations are therefore suitable to study large scale atmospheric dynamics to thermal forcing.

3

Controls of the Stratosphere-Troposphere Response to Thermal Forcing in Idealized Models: Mean Changes

This chapter addresses the questions of how the mean stratospheric circulation and the mean tropospheric circulation changes and how their changes couple as a response to tropical amplification (TA), asymmetric polar amplification (PA) and CO_2 induced stratopause cooling (SC). The experiments are performed with different complexity aiming at isolating the role of transient dry waves, transient moist waves and dry stationary waves in the response.

3.1 Transient Waves

3.1.1 Dry Atmosphere

The role of the transient dry waves in the response to TA is quantified for the ΔDFT, ΔD_{gw}FT and ΔD_jFT change. Figure 3.1a,c,e show the steady state temperature responses and Figure 3.1b,d,f the steady state zonal wind response. Stippling mark regions that are statistically significant. The statistical significance is calculated using an effective sample size to account for the degrees of freedom, properly.
The degrees of freedom in the system are equal to the sample size, if each time instant is independent from the previous one. Using perpetual equinox condition in ICON-DRY experiments with 6 hourly output data, this is not true, because there is a memory meaning that at a given point in time the atmospheric state has not forgotten the state before. As a first approach 30-day means are calculated to reduce the correlation between two consecutive time instants, and also because 30-day means are comparable to months in the real atmosphere. However, even with 30-day means a certain degree of dependence may remain, and it may differ among the control and sensitivity experiments. Therefore, an effective sample size is calculated. Following Woollings et al. (2008) and Baker et al. (2017) the statistical significance of mean changes is estimated by applying a two-tailed *t*-test using the 95% confidence level. The sample size is reduced

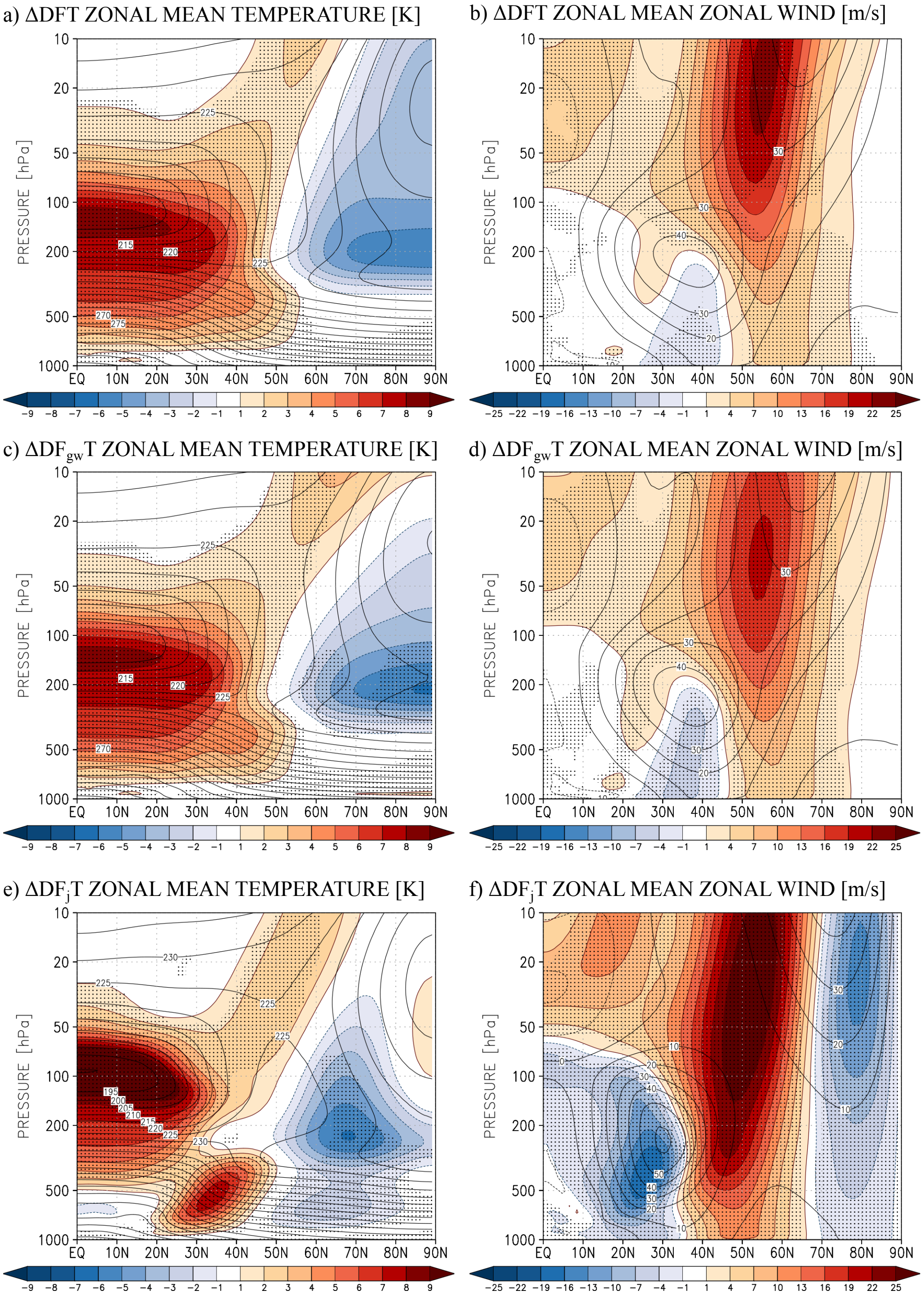

a) ΔDFT ZONAL MEAN TEMPERATURE [K]

b) ΔDFT ZONAL MEAN ZONAL WIND [m/s]

c) $\Delta DF_{gw}T$ ZONAL MEAN TEMPERATURE [K]

d) $\Delta DF_{gw}T$ ZONAL MEAN ZONAL WIND [m/s]

e) $\Delta DF_{j}T$ ZONAL MEAN TEMPERATURE [K]

f) $\Delta DF_{j}T$ ZONAL MEAN ZONAL WIND [m/s]

Figure 3.1. ΔDFT, ΔD_{gw}FT and ΔD_{j}FT steady state temperature [K] and zonal wind [m/s] change shown in color shading. Stippling mark areas where the change is significant using the 95th percentile threshold. Contour lines show the respective control experiment's steady state.

by computing an effective sample size for each time series:

$$N_{eff} = N\left(\frac{1-\rho}{1+\rho}\right), \tag{3.1}$$

where N is the actual sample size, N_{eff} the effective sample size and ρ the lag-1 auto-correlation coefficient of the time series. The Northern hemisphere data and the southern hemisphere data is put temporarily to each other even though the auto-correlation function generates an error at at the particular time step where one hemisphere data ends and the other hemisphere data begins. However, the error is very small and therefore negligible.

The upper troposphere temperature responses (Figure 3.1a,c,e) are characterized by a statistically significant mainly diabatically directly driven temperature increase in the tropics and subtropics related to the additional thermal forcing and by a dynamically indirectly driven cooling in the high latitudes. The cooling, however, is only statistically significant in the ΔD_{gw}FT and ΔD_jFT changes. As a response to the temperature change, via the thermal wind balance relation, the ΔDFT, ΔD_{gw}FT and ΔD_jFT upper level tropospheric mid-latitude zonal winds are strengthened, significantly. In the mid- to lower troposphere the zonal wind responses are characterized by a strengthening of the westerlies on the poleward flank of the eddy-driven jet and a weakening of the westerlies at the equatorward flank. The temperature and zonal wind responses in the troposphere and stratosphere are consistent with previous idealized works such as the work by Butler et al. (2010) and McGraw and Barnes (2016).

The tropospheric dynamical changes are quantified by the means of the eddy-driven wind speed change and the eddy-driven shift. In this thesis the calculation of the eddy-driven jet latitude and wind speed follows closely the method described by Woollings et al. (2010). The daily zonally averaged zonal winds are averaged between 20°N/S and 70°N/S and vertically (pressure weighted) between 750hPa and 850hPa. The resulting field is low-pass filtered to remove features associated with individual synoptic systems by using a 10 day Lanczos filter (Duchon, 1979). The daily maximum wind speed is detected and defined as the eddy-driven jet speed. The eddy-driven jet latitude is defined as the latitude at which the maximum wind speed is detected. The time series of the eddy-driven jet latitude and speed is then averaged in time to obtain the mean eddy-driven jet latitude and speed.

The change of the eddy-driven jet position is quantified in terms of the eddy-driven jet latitude change and the eddy-driven speed change. (Table 3.1). A considerable poleward shift of the eddy-driven jet of about 5.2° in the ΔDFT change, 6.3° in the ΔD_{gw}FT change and 8.6° in the ΔD_jFT change is found. The poleward shift is much larger than what is usually found (Barnes and Polvani, 2013) in climate model simulation (1° to 2°).

Table 3.1. Change of mean (μ) eddy-driven jet latitude (EDJ) [deg.] and EDJ speed [m/s] for the ΔDFT, ΔD_{gw}FT and ΔD_jFT change and their monthly standard deviation change (σ). Stars mark mean changes that are statistically significant

	ΔDFT		ΔD_{gw}FT		ΔD_jFT	
	μ	σ	μ	σ	μ	σ
EDJ latitude change	+5.2*	+0.39	+6.3*	+0.86	+8.6*	+0.76
EDJ speed change	-0.18	+0.04	-0.46*	+0.32	+4.7*	+0.45

The ΔD_jFT eddy-driven jet speed change shows an significant increase, whereas the ΔDFT and ΔD_{gw}FT change show an slightly decrease. The ΔDFT change, however, is non-significant.

Although, the main topic of this chapter are mean changes a short quantification of variability changes is done in terms of standard deviation changes of the eddy-driven jet latitude and the eddy-driven jet speed. The ΔDFT, ΔD_{gw}FT and ΔD_jFT standard deviation change of the eddy-driven jet latitude increases in all experiments and therefore reveals an intensified meridional eddy-driven jet wobble. The ΔDFT standard deviation of the eddy-driven jet speed hardly changes, whereas the ΔD_{gw}FT and ΔD_jFT standard deviation change of the eddy-driven jet speed increases revealing a intensified pulsing of the eddy-driven jet.

Please note, that an impact of the gravity wave parameterization on the troposphere can not entirely be ruled out as the perameterization initiates gravity waves in the troposphere. However, these results highlight that the eddy-driven jet variability can be strongly depending on the mean state even in dry simplified experiments emphasizing the results by Barnes and Polvani (2013) who have found that the leading pattern of variability for a given CMIP5 model can be a strong function of the mean state, specifically the mean jet latitude.

In the next step the mean differences among the experiments are discussed. There is only a small impact of the non-orographic gravity wave parametrization on the mean zonal wind and temperature response to TA given the ΔDFT and ΔD_{gw}FT responses of the troposphere and stratosphere are qualitative and quantitatively similar (Figure 3.1). However, there are large difference in the response between the ΔDFT or ΔD_{gw}FT change and the ΔD_jFT change. The ΔD_jFT zonal wind response amplitude is much larger than the ΔDFT and ΔD_{gw}FT responses. Further, the ΔD_jFT shows a vertical coherent weakening of the high latitude westerlies. There are two questions that emerge. Why does the ΔD_jFT show much stronger zonal wind response amplitudes and why does it show an weakening of the westerlies at high latitudes?

The stronger mid-latitude upper troposphere zonal wind response of the ΔD_jFT change

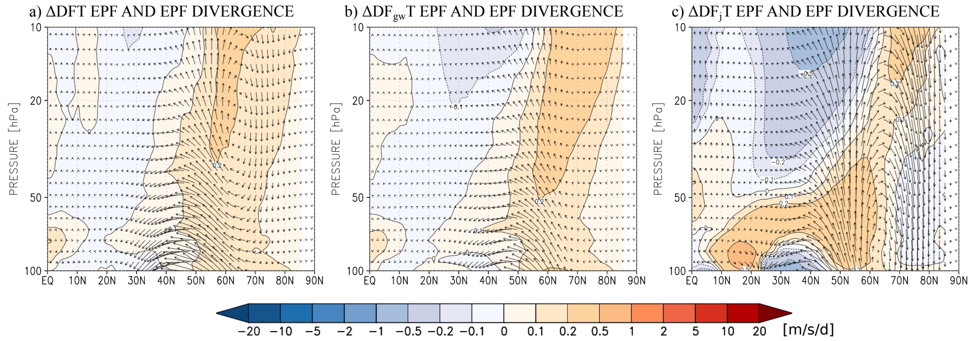

Figure 3.2. ΔDFT, ΔD$_{gw}$FT and ΔD$_{j}$FT lower stratospheric zonal wind tendency due to EP-flux divergence shown in color shading [m/s/d]. Arrows show the EP-flux change. The Arrow size is scaled in order to fit visual properties.

can be explained by the smaller meridional distribution of heat in the tropics and subtropics, possibly due to the equatorward placed eddy-driven jet position in the D$_{j}$F control experiment. Given that all three experiments share an equal additional thermal forcing amplitude the temperature response amplitude depends on the meridional extent of the Hadley circulation. A small meridional extent of the Hadley cell leads to an higher tropical temperature response as the potential meridional distribution of heat is more constraint to the tropics. This, then, leads to intensified mid-latitude upper troposphere winds as the sub-tropical temperature gradient is increased more intensively than in the ΔDFT or ΔD$_{j}$FT change. Therefore, the mid-latitude upper tropospheric zonal wind response difference of the ΔD$_{j}$FT in comparison to the ΔDFT and ΔD$_{gw}$FT response can be explained by the difference in the controls experiment mean state. However, the intensified response of the lower troposphere and stratosphere zonal winds can only be explained using further diagnostics.

In order to quantify the processes leading to the differences both the stratospheric and tropospheric changes are considered and investigated regarding their annular mode decorrelation time-scale changes and the stratospheric wave propagation and dissipation changes. Table 3.2 shows the changes of the decorrealtion time-scales for the three experiments. The ΔDFT and ΔD$_{gw}$FT annular mode autocorrelation time-scales changes are negative in the troposphere, positive in the ΔDFT's stratosphere and negative in the ΔD$_{gw}$FT's stratosphere. A negative (positive) change means that a given atmospheric state forgets an previous atmospheric state faster (slower) in the sensitivity experiment than in the control experiment. The ΔDFT and ΔD$_{gw}$FT magnitudes change less than 25%. Instead being negative, the ΔD$_{j}$FT annular mode autocorrelation time-scale's change is positive in the troposphere but, nevertheless, still shows the same magnitude of the change. However, the ΔD$_{j}$FT stratosphere change is much larger than the ΔDFT and ΔD$_{gw}$FT changes. In fact it increase by 117%. This means the stratospheric polar vortex remains much longer in a particular mode of variability, with implications on

Table 3.2. Change of the annular mode decorrelation time-scales $\Delta\tau$ and change of the estimated uncertainty Δstd(τ_N) of tropospheric and stratospheric annular modes

Experiment	Trop. $\Delta\tau$	Trop. Δstd(τ)	Strat. $\Delta\tau$	Strat. Δstd(τ)
Δ DFT	-13	-2.23	+7	+1.81
Δ D_{gw}FT	-10	-1.56	-19	-4.6
Δ D_jFT	+13	+2.38	+78	+22.03

the statistics and on the mean response. Usually, an experiment that consists of a very large annular mode time-scale needs to be run much longer to have the same statistical certainty provided by an experiment with a lower annular mode time-scale. Further, Gerber et al. (2008) show that models with large annular mode autocorellation time-scale also consist of large response amplitudes to external forcing. However, even if the response's amplitudes are larger, the change of the pattern is possibly not affected. In the next step the differences of the changes of the stratospheric wave dissipation among the experiments are quantified by the use of the Transformed Eulerian Mean (TEM) framework.

The TEM framework has been introduced by Andrews and McIntyre (1976), Andrews and McIntyre (1978) and Boyd (1976). It provides an powerful framework for studying eddy effects by offering a transparent approach to the eddy-mean flow interaction problem. The usefulness of the TEM framework can be illustrated by considering the conventional eulerian mean zonal mean zonal momentum and thermodynamic energy equations for quasi geostrophic motions on the beta-plane which are given by

$$\frac{\partial\overline{u}}{\partial t} - f_0\overline{v} = \frac{-\partial(\overline{u'v'})}{\partial y} + \overline{X}, \tag{3.2}$$

$$\frac{\partial\overline{T}}{\partial t} + N^2HR^{-1}\overline{w} = \frac{-\partial(\overline{v'T'})}{\partial y} + \frac{\overline{J}}{c_p}, \tag{3.3}$$

where N is the buoyancy frequency or Brunt-Väisälä frequency which is defined by

$$N^2 \equiv \frac{R}{H}\left(\frac{\kappa T_0}{H} + \frac{dT_0}{dz}\right) \tag{3.4}$$

The term $(\overline{u'v'})$ is the zonally averaged momentum flux and $(\overline{v'T'})$ the zonally averaged heat flux. Primes denote departure from the zonal mean. From equation 3.3 one can obtain that there is a cancellation between the eddy heat flux convergence and the adiabatic cooling and that the diabatic heating term is a small residual. This implies that in the mean an air parcel can only be lifted to an higher equilibrium altitude, if its potential temperature is increased, which in fact can only be achieved by diabatic heating. Therefore, it is the residual circulation associated with the diabatic heating, that is related to the mean meridional mass flow. Hence, by defining the residual circulation ($\overline{v}^*$ $\overline{w}^*$) the TEM equations can be obtained. The residual circulation is defined as follows:

$$\overline{v}^* = \overline{v} - \frac{1}{\rho} R \frac{1}{H} \partial \left(\frac{\rho_0 \overline{v'T'}}{N^2} \right) \Big/ \partial z \tag{3.5}$$

$$\overline{w}^* = \overline{w} + R \frac{1}{H} \partial \left(\frac{\overline{v'T'}}{N^2} \right) \Big/ \partial y \tag{3.6}$$

The residual vertical velocity now represents that part of the adiabatic temperature change, that is not canceled by the eddy heat flux divergence. The zonal mean circulation ($\overline{v}$ $\overline{w}$) in equation 3.2 and 3.3 can now be substituted using equations 3.5 and 3.6 which results in the TEM equations:

$$\frac{\partial \overline{u}}{\partial t} - f_0 \overline{v}^* = \frac{1}{\rho} \nabla \cdot F + \overline{X} \equiv \overline{G}, \tag{3.7}$$

$$\frac{\partial \overline{T}}{\partial t} + N^2 H R^{-1} \overline{w}^* = \frac{\overline{J}}{c_p}, \tag{3.8}$$

$$\frac{\partial \overline{v}^*}{\partial y} + \rho_0^{-1} \frac{\partial (\rho_0 \overline{w}^*)}{\partial z} = 0 \tag{3.9}$$

The key advantage of the transformation is, that the eddy forcing on the mean state is now simply described by one term namely $\overline{G}$, which contains the large-scale eddy forcing represented by the Eliassen-Palm flux divergence $\nabla \cdot F$ and the dissipation represented by $\overline{X}$. In model experiments, technically, $\nabla \cdot F$ can be seen as the eddy forcing that comes from the resolved waves (Rossby waves) and $\overline{X}$ as the eddy forcing that comes from parameterized, and ,therefore, unresolved waves (gravity waves). Note, that for high horizontal grid resolutions some of the gravity wave spectrum may be resolved.

Hardiman et al. (2010) demonstrated, that it is necessary to transform the model data to pressure coordinates before performing the TEM-diagnostic. Following this suggestions the experiments' data is written out in pressure levels very close to the dynamical core. The hydrostatic primitive equation Eliassen-Palm flux (EP flux) is a 2-dimensional vector in the meridional-vertical plane. In pressure coordinates F is defined by

$$F_{(\phi)} = acos\phi \left(\frac{\partial \overline{u}}{\partial p} \psi - \overline{u'v'} \right), \tag{3.10}$$

$$F_{(p)} = acos\phi \left(\left[f - \frac{\partial \overline{u} cos\phi}{acos\phi \partial \phi} \right] \psi - \overline{u'w'} \right), \tag{3.11}$$

where ψ is the eddy stream-function and given by

$$\psi = \overline{v'\theta'} \Big/ \frac{\partial \overline{\theta}}{\partial p}. \tag{3.12}$$

The EP-flux divergence is defined by

$$\nabla \cdot F = \frac{\partial F_{(\phi)} cos\phi}{acos\phi \partial \phi} + \frac{\partial F_{(p)}}{\partial p} \tag{3.13}$$

Considering equation 3.2 the EP-flux divergence is a measure of the zonal wind tendency and, therefore, provides the opportunity to study the eddy forcing on the zonal mean flow. The mass stream-function at a particular pressure level is defined by

$$\Psi_{(p)} = \frac{2\pi acos\phi}{g_0} \left(\int_0^p \overline{v} dp - \psi \right) \tag{3.14}$$

The ΔDFT, ΔD$_{gw}$FT and ΔD$_j$FT stratospheric wave propagation and dissipation changes between 100hPa and 10hPa are shown in Figure 3.2. The arrows show the EP-flux changes. The color shading shows the divergence changes. Note that the arrows are scaled to fit visual properties best, meaning that they aren't necessarily consistent with the divergence field in the background. The fluxes are plotted in order to show the propagation changes. The flux component changes are discussed in detail in the following paragraph. Positive divergence means less wave dissipation and negative divergence increased wave dissipation. In all experiments wave dissipation shifts slightly toward higher stratospheric levels and toward lower latitudes coinciding with increased westerly winds in the stratospheric mid-latitudes to high latitudes in all experiments. In addition, the ΔD$_j$FT change shows increased wave dissipation in the lower polar stratosphere. This wave dissipation increase at polar latitudes together with the wave dissipation decrease at high latitudes correspond to increased warming at polar latitudes and decreased warming at high latitudes. Warming at the polar latitudes and cooling of the high-latitudes decreases the meridional temperature gradient which is in correspondence with the decreased westerly winds at the high latitudes. An high latitude easterly change, therefore, can occur as a response to tropical amplification, when the control experiment's steady state is characterized by a low latitude eddy-driven jet position. This leads to the follow up questions of: How much of the wave dissipation change is due to changes in wave propagation changes within the stratosphere and how much of it is due to increased wave flux that comes from the troposphere?

The stratospheric wave propagation changes and wave penetration changes are quantified by considering the individual components of the EP-flux change. Figure 3.3 shows the horizontal EP-flux component change in color shading in the upper row and the vertical EP-flux change in color shading in the bottom row for a),d) the ΔDFT change, b),e) the ΔD_{gw}FT change and c),f) the ΔD_jFT change. The contour lines show the control experiment's steady state and stippling mark regions where the change is significant given a 95 percentile threshold. The ΔDFT and ΔD_{gw}FT horizontal component change show a significant negative change meaning increased equatorward refraction of waves in the entire lower stratosphere. The ΔD_jFT change, however, is characterized by an dipole structure with negative values in the subtropics and mid-latitudes and positive values in the high latitudes and polar latitudes. The ΔD_jFT, therefore, shows increased equatorward refraction of waves in the subtropics and mid-latitudes which is similar to the change of the other two experiments, but shows a poleward refraction change (sign change) at the high latitudes.

The ΔDFT, ΔD_{gw}FT and ΔD_jFT vertical EP-flux component change is characterized

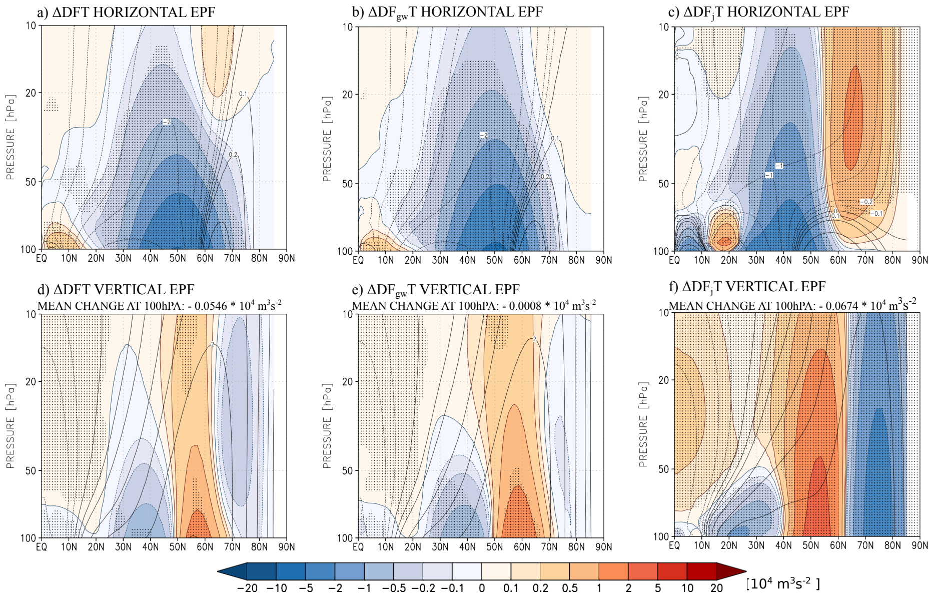

Figure 3.3. ΔDFT, ΔD_{gw}FT and ΔD_jFT lower stratosphere horizontal (top row) and vertical (bottom row) EP-flux component changes in color shading. Stippling mark areas where the change is significant using the 95th percentile threshold. Contour lines show the respective control experiment's steady state.

by a seesaw pattern with positive values in the mid- to high latitudes and negative values poleward and equatorward of the positive change. The total upward flux change calculated as the latitudinal weighted average at 100hPa is negative in all experiments, meaning there are less waves penetrating from the troposphere into the stratosphere. However, the hemispheric mean change is small given it is two orders of magnitudes smaller than the controls experiments EP-flux. Therefore, it is found that the stratospheric circulation change to tropical amplification on a flat surface under dry conditions is largely determined by wave propagation changes also when the gravity wave parameterizations is included or the control's eddy-driven jet is shifted toward the equator. However, the way the wave propagation changes depends on the control's eddy-driven jet position relative to the stratospheric vortex position, meaning the stratospheric circulation change is sensitive to the tropospheric steady state, when only transient planetary waves are involved. In this simple setup an easterly change of the high latitude stratospheric winds as a response to TA is only found, when the control's eddy-driven jet is close to the subtropical jet.

3.1.2 Moist Atmosphere

In this section the impact of moisture on the troposphere-stratosphere coupled response is investigated. For this, the Moist-AP experiments introduced in section 2.1.4 is used. For consistency, from now on, the Moist-AP is called MF and the change to increased SST of 4K ΔMF4K. Figure 3.4 shows in color shading the steady state zonal mean temperature and zonal mean zonal wind response to increased SSTs of 4K. The contour lines show the control experiment's steady state. The control's eddy-driven jet is comparable to the D_jF control experiment's eddy-driven jet position, meaning it is euatorward of the DF and D_{gw}F ones. Given the combination of two dry experiments with different eddy-driven jet positions and one moist experiment with an eddy-driven jet position comparable to one of the dry experiments, this setup provides the opportunity of qualitatively investigating the impact of moisture on the change. Since the dry experiments differ fundamentally from the moist experiment in their tropospheric diabatic forcing a quantitative investigation of the changes to TA is inappropriate, and therefore subtraction of changes are not considered. Also because the SST increase heats up the entire troposphere and is therefore not restricted to the tropics.

The ΔMF4K steady state tropospheric zonal mean temperature is characterized by a warming, which appears throughout the troposphere because the SSTs are increased uniformly by 4K. Increasing the SSTs uniformly prevents induced changes in the mid-latitude baroclinicity. Since the the MF control and MF4K experiments contain atmospheric moist processes, tropical amplification is naturally captured. The overall

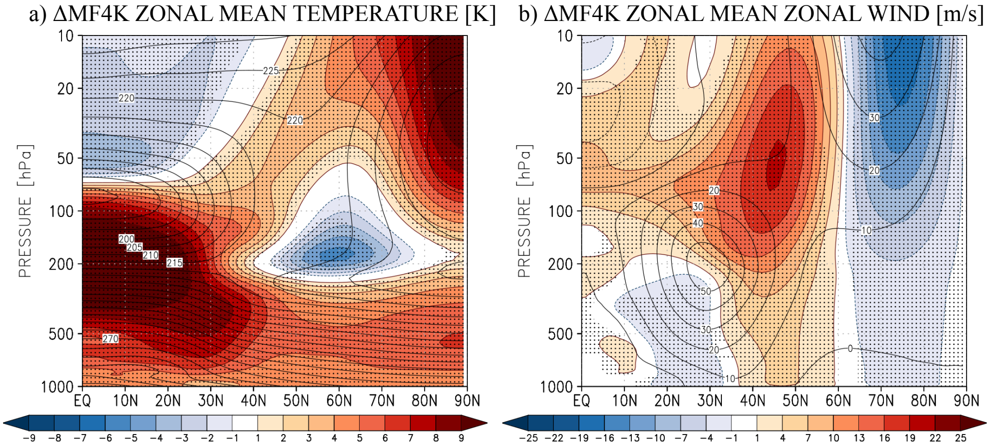

Figure 3.4. ΔMF4K steady state temperature [K] and zonal wind [m/s] change shown in color shading. Stippling mark areas where the change is significant using the 95^{th} percentile threshold. Contour lines show the respective control experiment's steady state.

change in the equator-pole temperature gradient, however, is similar to the dry experiments and therefore comparable. The tropical upper troposphere warms by about 12K and the pole about 5 to 6K. Since the SSTs are increased by 4K, there is an amplification of temperatures at the pole (not at the surface) that is dynamically driven. A similar but smaller dynamically driven increase in polar temperatures is also found in the dry experiments.

The lower and mid-tropospheric zonal mean winds are decreased at the equatorward side of the eddy-driven jet and are increased at the poleward side of the eddy-driven jet. In deed, similar to the dry experiments an poleward shift of the eddy driven jet is found. However, the magnitude (3.8°) of the poleward shift is only 73 percent of the ΔDFT change and only 44 percent of the ΔD_jFT change.

The ΔMF4K stratospheric change is characterized by a cooling throughout the tropics

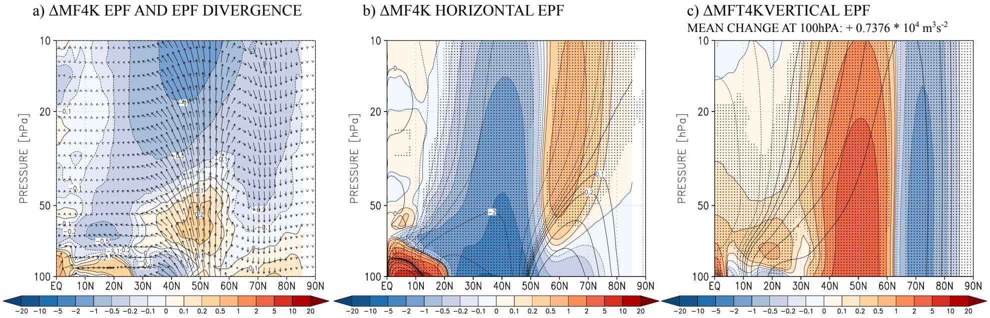

Figure 3.5. ΔMF4K lower stratosphere zonal wind tendency due to EP-flux divergence shown in color shading in a) [m/s/d]. Arrows show the EP-flux change. The Arrow size is scaled in order for visual proposes. b) and c) show the ΔMF4K lower stratosphere horizontal and vertical EP-flux component changes in color shading in [$10^4 m^3 s^{-2}$], respectively. Stippling mark areas where the change is significant using the 95^{th} percentile threshold. Contour lines show the respective control experiment's steady state

and a warming throughout the mid- to polar latitudes. Similar to what is found in the $\Delta \mathrm{D}_j\mathrm{FT}$ change, the stratospheric westerlies strengthen at mid-latitudes, but weaken at high to polar latitudes. However, the weakening of the high latitude stratospheric westerlies is more pronounced and broader in latitudinal extent in the ΔMF4K than in the $\Delta \mathrm{D}_j\mathrm{FT}$ change.

The ΔMF4K wave dissipation change is shown in Figure 3.5a, the horizontal wave EP-flux change in Figure 3.5b and the vertical EP-flux change in Figure 3.5c. As a response to tropical amplification, the ΔMF4K shows more wave dissipation increase than the dry experiments, which is in compliance with more increased vertical EP-flux at the mid-latitudes. In contrast to the dry experiments, the ΔMF4K net hemispheric upward EP-flux change at 100hPa shows a significant increase. The ΔMF4K horizontal EP-flux change, however, looks very similar to the $\Delta \mathrm{D}_j\mathrm{FT}$ horizontal EP-flux change. This means the ΔMF4K change differs from the $\Delta \mathrm{D}_j\mathrm{FT}$, in particular, in the upward EP-flux change, implicating that changes in moist processes contributes significantly to the upward EP-flux change and through increased wave dissipation to the easterly change at high latitudes.

In order to investigate changes in the wave sources the meridional heat flux and geopotential height variance are considered in wavenumber space. The wavenumber space is calculated using a fast-Fourier transform. Figure 3.6 compares the ΔMF4K meridional heat flux and geopotential height variance changes in wavenumber space at 260hPa to the $\Delta \mathrm{D}_j\mathrm{FT}$ changes.

The $\Delta \mathrm{D}_j\mathrm{FT}$ meridional heat flux change (Figure 3.6a) is characterized by an poleward shift of the synoptic-scale heat flux (wavenumber 4 to 8) and a latitudinal narrowing of the planetary-scale heat flux (wavenumber 1 to 3). The ΔMF4K meridional heat flux change (Figure 3.6b), instead, is characterized by a shift of synoptic-scale meridional heat flux from smaller waves (wavenumber 7 to 8) to larger waves (wavenumber 4 to 6), and by an equatorward shift of the planetary-scale meridional heat flux. The $\Delta \mathrm{D}_j\mathrm{FT}$ geopotential height variance change shows a very similar pattern in wavenumber space as the $\Delta \mathrm{D}_j\mathrm{FT}$ meridional heat flux change. Furthermore, the ΔMF4K geopotential height variance change shows two maxima, one at wavenumber 5 and another at wavenumber 1, whereas the ΔMF4K geopotential height variance change only shows one maximum at wavenumber 5. This suggest an upscale energy cascade in the ΔMF4K change. Figure 3.7 shows the wavenumber integrated (wave 1 to wave 12) meridional heat flux (Figure 3.7a) and the wavenumber integrated geopotential height variance (Figure 3.7b). The red line shows the $\Delta \mathrm{D}_j\mathrm{FT}$ change and the blue line the ΔMF4K change. Apparently, the $\Delta \mathrm{D}_j\mathrm{FT}$ minima and maxima of the meridional heat flux change and the geopotential height variance change appear at similar latitudes. This, however, does not apply to the ΔMF4K change. In fact, the ΔMF4K geopotential height variance

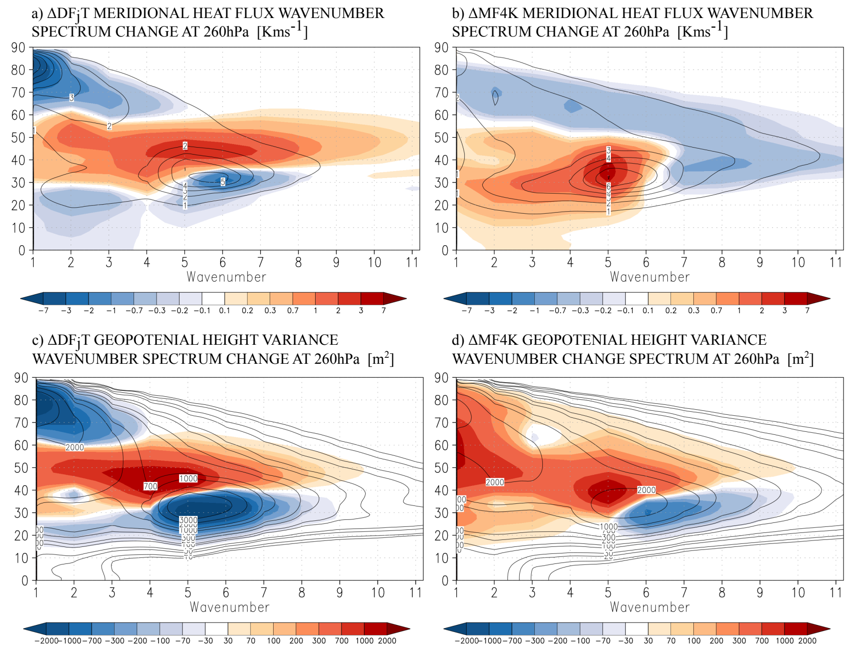

Figure 3.6. $\Delta D_j FT$ and $\Delta MF4K$ mean heat flux (top row) wavenumber spectrum change and mean geopotential height variance (bottom row) wavenumber spectrum change at 260hPa shown in color shading. Contour lines show the respective control experiment's steady state.

change is dominated by an increased variance at almost all latitudes.
Figure 3.6 and 3.7 suggest that the presence of moisture contributes to the stratospheric vertical EP-flux change due to an upscale energy cascade from synoptic-scale waves to planetary-scale waves. In addition, the change in moisture can increase the wave generation of waves. Moisture, therefore, may also be capable of impacting indirectly the eddy-driven jet response through a stratospheric pathway.

3.2 Stationary Waves

The role of the stationary waves in the troposphere-stratosphere coupled response is investigated not only as a response to Tropical Amplification TA, but also as a response to Polar Amplification (PA) and CO_2 induced stratopause cooling (SC).

3.2.1 Tropical Amplification

The drivers of the stratosphere circulation changes are investigated by means of a wave activity budget following Kushner and Polvani (2004). Considering the divergence theorem the term $\nabla \cdot F$ (equations 3.10, 3.11, 3.13) can be broken up into four terms,

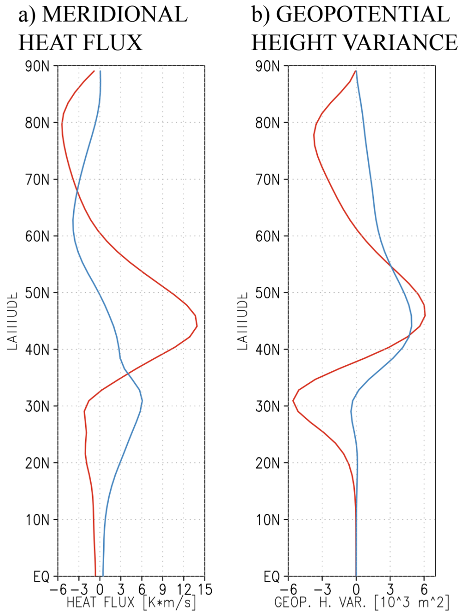

Figure 3.7. Mean integrated meridional heat flux change shown in a) and mean integraded geopotential height variance change shown in b). The integration is performed over wavenumber 1 to 12. The red line shows the ΔD_jFT change and the blue line the ΔMF4K change.

representing the flux through each side of the box:

$$\begin{aligned}\int_{p_1}^{p_2}\int_{\phi_1}^{\phi_2} \nabla \cdot F\, cos\phi\; d\phi\; dp \\ = a^{-1}\, cos\phi \int_{p_1}^{p_2} F_{(\phi)}\; dp|_{\phi_2} - a^{-1}\, cos\phi \int_{p_1}^{p_2} F_{(\phi)}\; dp|_{\phi_1} \\ + \int_{\phi_1}^{\phi_2} cos\phi F_{(p)}\; dp|_{p_2} - \int_{\phi_1}^{\phi_2} cos\phi F_{(p)}\; dp|_{p_1} \end{aligned} \tag{3.15}$$

The EP flux budget of the wave flux is calculated over a selected latitude-pressure box, that extends meridionally from ϕ_1 = 45°N/S to the pole and vertically from p_1 =100hPa to p_1 =10hPa. Figure 3.8 shows the EP-flux budget change as a response to TA for the ΔDFT (grey) and $\Delta \text{DF}_{gw}T$ (grey) experiments, for the $\Delta DW1_xT$ (red) and $\Delta DW2_xT$ (orange) experiments as well as for the $\Delta DW1W2_{600}T$ experiment (yellow). Each arrow represents the experiment's particular boundary integral. The position on the boundary line is arbitrary and has no meaning. Arrows at the lower boundary pointing upward into the box mean increased wave flux entering the stratosphere from below. Arrows that point upward at the upper boundary and to the left at the equatorward boundary mean wave flux changes, that leave the box to the upper stratosphere and to the subtropics, respectively. The bars in the center of the figure denote the EP-flux convergence. Please note, since the box budget is calculated in p-coordinates, positive values mean convergence, and therefore increased wave dissipation. The arrows' length of the individual experiments are scaled with respect to the ΔDFT change arrow length at the lower boundary. The length of the ΔDFT change arrow at the lower boundary is set arbitrary to fit visual properties best. The same applies for the scaling of the bars. The values show the change in units of 10^4 kg m s^{-4}.

The horizontal component change of all experiments show increased equatorward refraction of waves as a response to TA, robustly. This is illustrated by the increased wave flux that leaves the high latitude box at 45°N/S. The horizontal component change, therefore, is independent on the prescribed surface stationary wavenumber and amplitude, given that no correlation is found between the magnitude of the horizontal component change and the stationary wave amplitude or wavenumber.

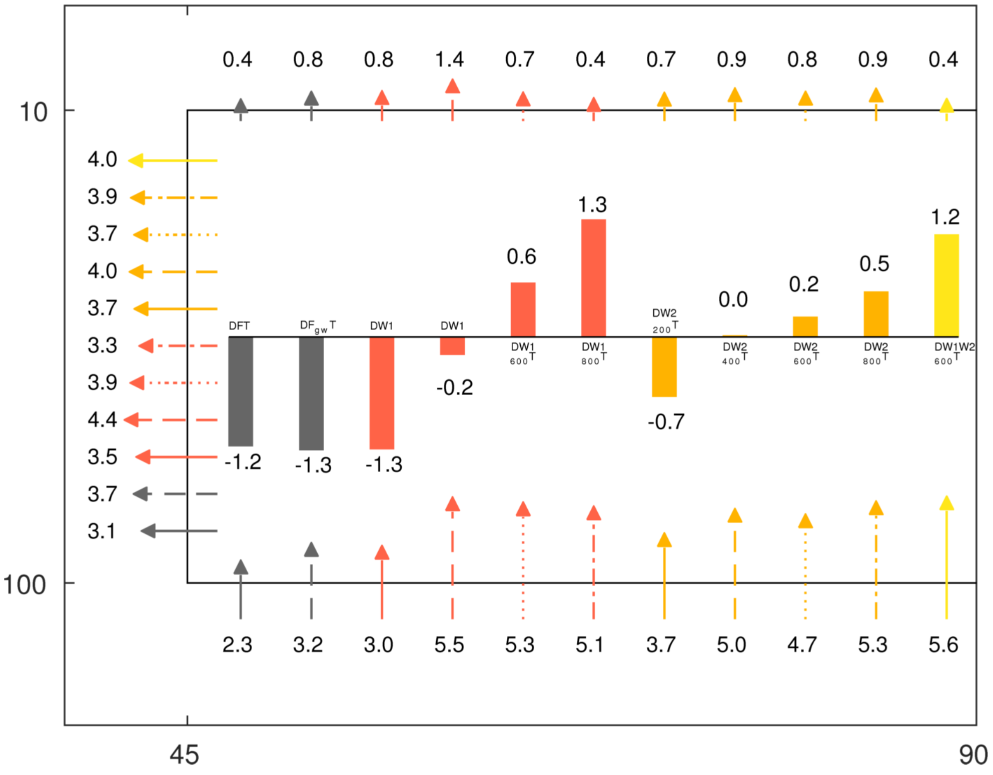

Figure 3.8. ΔDFT, $\Delta D_{gw}FT$, $\Delta DW1_xT$, $\Delta DW2_xT$ and $\Delta DW1W2_{600}T$ EP box budget changes between 45°N/S and 90°N/S and between 100hPa and 10hPa. The arrows indicate the time mean EP-flux change integrated over the respective boundary. The bars in the center denote the EP-flux convergence change. Positive values mean increased wave dissipation. The gray color shows the flat surface experiments, the red color the experiments with idealized stationary wave 1 orography, the orange color the experiments with idealized stationary wave 2 orography and the yellow color the experiment with idealized stationary wave 1 and wave 2 orography. The values next to the bars and arrows quantify the change. They are given in units of of 10^4 kg m s^{-4}. The arrows' length are scaled with respect to the ΔDFT change at the bottom boundary. The ΔDFT arrow length is set arbitrary. The same applies to the bars.

The vertical EP-flux component change at the top boundary is small compared to the one at the bottom boundary, and therefore contributes only slightly to the dissipation changes within the box. The experiments' vertical component changes at 100hPa show a robust increase. In contrast to the horizontal component change the vertical EP-flux component change shows increased vertical wave flux changes when stationary waves are present.

The vertical EP-flux change increases wave propagation into the box and the horizontal EP-flux change decreases wave propagation out of the box. Given that the vertical EP-flux change at the bottom boundary opposes the horizontal EP-flux flux change and given that only the vertical EP-flux component change shows a dependence on the stationary wave amplitudes, it is largely the vertical EP-flux flux change at the bottom boundary, that determines the dissipation change within the box to be positive or negative. In fact, in the experiments with a flat surface the vertical EP-flux change (wave generation change), that enters the box from below is not capable of overcompensating the reduction of the horizontal component change (wave propagation change), which leads to less wave dissipation at the high latitudes. Stationary waves are needed to increase the vertical EP-flux component. However, in order to drive increased wave dissipation at the high latitudes, the surface amplitudes of wavenumbner 1 and wavenumber 2 need to exceed 400m.

Before the impact of the stratospheric circulation change on the tropospheric circulation

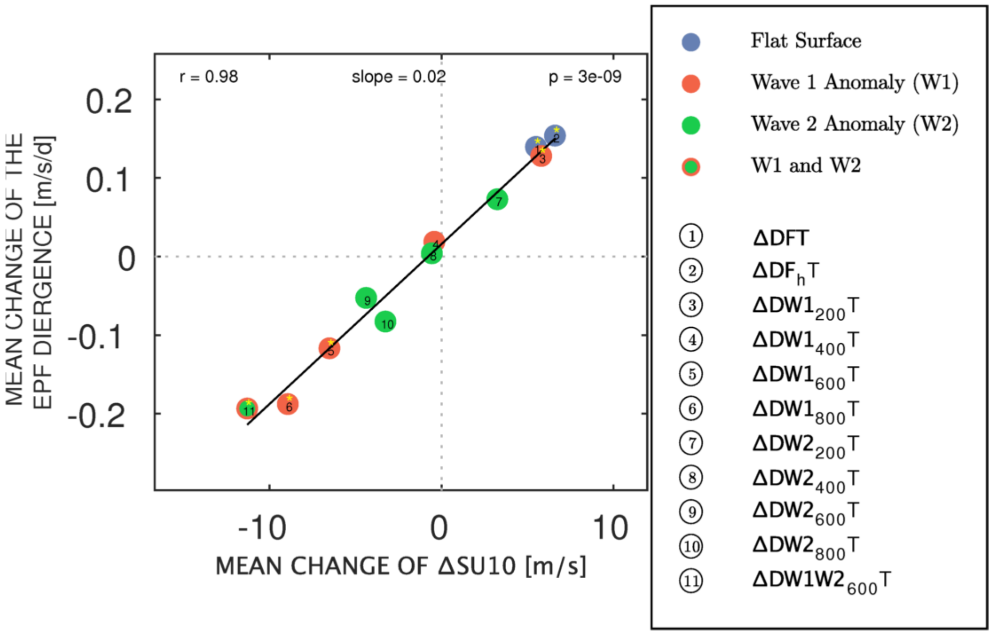

Figure 3.9. ΔDFT, $\Delta D_{gw}FT$, $\Delta DW1_xT$, $\Delta DW2_xT$ and $\Delta DW1W2_{600}T$ mean EP-flux divergence change versus mean ΔSU10 change. The black line shows the regression line. The p-value is the probability and the r-value the correlation coefficient. Stars mark changes that are statistically significant with respect to both variables.

change is investigated, proof of the wave-mean flow interaction is given. It is well known that the wave-mean flow interaction is the dominant driver of the stratospheric dynamical variability, hence mean wave dissipation changes ought to be strongly correlated to mean changes in the stratospheric high latitude winds. The wave-mean flow interaction is quantified using the dissipation change and the ΔSU10 index change. The ΔSU10 index is the zonal mean zonal wind change at 10hPa, averaged between 70°N/S and 80°N/S. It is a measure of the high latitude stratospheric zonal wind change. For simplicity, in the following the latitude-pressure weighted EP-flux divergence change is used instead of EP-flux convergence change as it is more commonly used when comparing to the stratospheric wind change. The EP-flux divergence is averaged between 100hPa to 10hPa and between 45° to 90° and is, therefore, comparable to the EP-flux convergence change shown in Figure 3.8. The wave-mean flow interaction is demonstrated by plotting the ΔDFT, ΔD_{gw}FT, $\Delta DW1_x T$, $\Delta DW2_x T$ and $\Delta DW1W2_{600} T$ EP-flux dissipation change against the ΔSU10 change (Figure 3.9). Please, note that in case of the ΔD_{gw}FT the parameterized waves are added to the wave dissipation[1]. The blue color shows the experiments with the flat surface, the red color the experiments with the idealized surface wavenumber 1 orography and the green color the idealized surface wavenumber 2 orography. The dot with a green filling and a red edge marks the experiment with idealized surface wavenumber 1 and wavenumber 2 orography. A star marks those changes that are statistically significant with respect to both variables. The black line is the regression line. The regression analysis reveals a highly significant relationship ($p \ll 0.05$) supported by a correlation coefficient of 0.98. Each 0.02m/s/d mean EPFD change corresponds to a 1m/s mean zonal wind change, demonstrating the wave-mean flow interaction.

The stratosphere-troposphere coupled response is quantified by linking the ΔSU10 changes and ΔT300 changes to the eddy-driven jet latitude changes and the eddy-driven jet speed changes. The ΔSU10 index is a measure of the stratospheric dynamical change and the ΔT300 index a measure of the TA. The ΔT300 index is the mean temperature change at 300hPa averaged between 30°S and 30°N. Figure 3.10 shows the relationship between the mean eddy-driven jet latitude change and the mean change of the ΔT300. The Figure is technically identical to Figure 3.9 with the extension of the vertical and horizontal lines, which represent the confidence intervals for the difference in population means of the control experiment and sensitivity experiment for a given significance value of 95 percent. A significant relationship between the driven-jet latitude change and the ΔT300 change is found represented by an p-value of $4*10-5$ and a correlation coefficient of 0.86. There are different tropical temperature responses to an identical additional thermal forcing among the experiments. In fact the larger the

---

[1] The contribution of the parameterized gravity wave dissipation to the the total wave dissipation is very small in the lower stratosphere

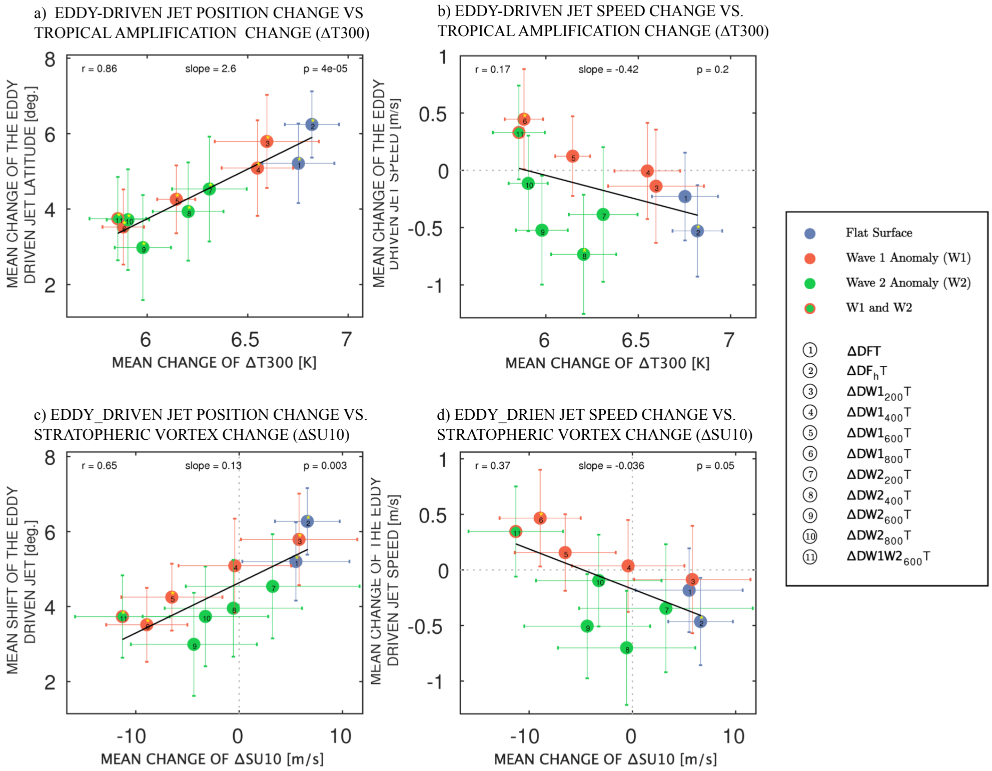

a) EDDY-DRIVEN JET POSITION CHANGE VS TROPICAL AMPLIFICATION CHANGE (ΔT300)

b) EDDY-DRIVEN JET SPEED CHANGE VS. TROPICAL AMPLIFICATION CHANGE (ΔT300)

c) EDDY_DRIVEN JET POSITION CHANGE VS. STRATOPHERIC VORTEX CHANGE (ΔSU10)

d) EDDY_DRIEN JET SPEED CHANGE VS. STRATOPHERIC VORTEX CHANGE (ΔSU10)

Figure 3.10. ΔDFT, ΔD_{gw}FT, $\Delta DW1_x$T, $\Delta DW2_x$T and $\Delta DW1W2_{600}$T mean changes of the eddy-driven jet latitude and speed versus the mean changes of ΔT300 and versus the mean changes of the ΔSU10. The black lines show the regression line. The p-value is the probability and the r-value the correlation coefficient. The horizontal and vertical lines show the estimated uncertainty of the mean changes. Stars mark changes that are statistically significant with respect to both variables.

prescribed surface orography wave amplitude the less pronounced is the temperature response due to TA and the less pronounced the poleward shift of the eddy-driven jet latitude. It is not a surprise, that there is a strong link between the magnitude of the TA and the position of the eddy-driven jet. However, it is known that the magnitude of the TA connects linearly to the eddy-driven jet shift (Baker et al., 2017). Assuming a similar behavior in the ICON-DRY experiments, the change of the eddy-driven jet latitude would be zero for a warming of approximately 4.5K, when extrapolating the regression line. This strongly suggests, that TA is not the only contributor to the eddy-driven jet latitude change but induced dynamical changes matter too.

Figure 3.10c shows the relationship between the eddy-driven jet latitude change and the ΔSU10 change. A significant relationship between both indexes is found. The strongest poleward displacement of the eddy-driven jet is found in those experiments, that have small orographic amplitudes or a flat surface. The $\Delta DW2_x T$ changes show that for a orographic wavenumber 2 an amplitude in the surface geopotential of 200m is sufficient in leading to a weakening of the high latitude stratospheric winds, and also sufficient in leading to a reduction of the associated poleward shift of the eddy-driven jet. The $\Delta DW1_xT$ changes show that in case of a orographic wavenumber 1 an amplitude of at least 400m is needed to weaken the high latitude winds, and to lead to a reduction of the poleward shift of the eddy-driven jet latitude. This suggest the wavenumber 2 is more potent in affecting stratosphere-troposphere coupled response to TA. Even though, the wavenumber 1 seems to be less potent in affecting the stratosphere-troposphere coupled response to TA, since no affect can be seen for a wave amplitude of 200m, it seems to be more potent for large wave 1 amplitudes. However, for both the $\Delta DW1_xT$ and the $\Delta DW2_xT$ change a wave numbers with an amplitude of at least 400m is necessary to drive an easterly change of the high latitude stratospheric zonal winds.

Even though, there is no relationship found between the the eddy-driven jet speed change and the ΔT300 change (Figure 3.10b), given a p-value larger than 0.05 (5 percent) and an low correlation coefficient of 0.17, there may be a tendency of increased eddy-driven jet speed in the $\Delta DW1_xT$ changes and a decreased eddy-driven jet speed in the $\Delta DW2_xT$ experiments. Since the relationship to the ΔSU10 change is larger than to the ΔT300 change an impact of the stratospheric change on the eddy-driven jet speed can not be ruled, but neither be confirmed with certainty as the p-value hits exactly the 5 percent threshold.

3.2.2 Polar Amplification

Idealized studies, so far, investigated the tropospheric dynamical response to sea ice retreat by imposing a zonally symmetric thermal forcing centered at the pole. In this study the eddy-driven jet response is investigated also to an additional asymmetric thermal forcing with different longitudinal extends and idealized orography.

First, the response to a symmetric thermal forcing is investigated in order to have an reference experiments that can be compared to other studies. Figure 3.11a shows the temperature response due to an imposed zonally symmetric thermal forcing near the polar surface. As a consequence the lower tropospheric polar region warms by about 4K. The $\Delta \mathrm{DFP}_{360}$ zonal wind response (Figure 3.11b) is consistent with other studies (Deser et al., 2015; Oudar et al., 2017; Peings and Magnusdottir, 2014b) showing a broad region of easterly zonal wind change poleward of the eddy-driven jet and an increase of westerly winds equatorward of the eddy-driven jet. The stippling shows that the change is statistical significant using the 95^{th} percentile as a threshold. Further, the eddy-driven-jet shifts toward the equator by -0.64° (Table 3.3) which seem to be a robust response to PA given it occurs in complex climate models, barotropic models (Ronalds et al., 2018) and dry dynamical core models (Butler et, al 2010). However, the $\Delta \mathrm{DFP}_{360}$ eddy-driven jet shift is found to be non-significant. Instead, a significant

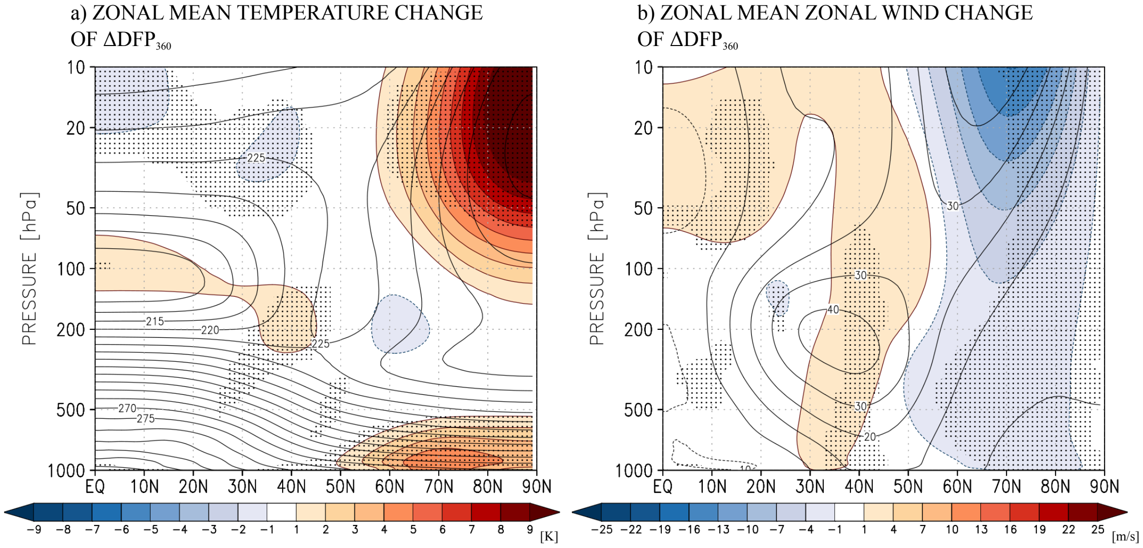

Figure 3.11. $\Delta\mathrm{DFP}_{360}$ steady state temperature and zonal wind change shown in color shading. Stippling mark areas where the change is significant using the 95^{th} percentile threshold. Contour lines show the control experiment's steady state.

increase in the eddy-driven jet speed of 0.76 m/s is found.

The stratospheric change is investigated using the EPF-budget. The zonally symmetric polar amplification increases the high latitude wave dissipation (Figure 3.13,$\Delta\mathrm{DFP}_{360}$) mostly due to increased incoming wave flux from the troposphere. As a consequence a dynamical warming in the polar stratosphere (Figure 3.11a) and an associated weakened polar vortex (Figure 3.11b) is found. Since the thermal forcing is symmetric it does not by itself act as a wave source. The increase of wave flux into the stratosphere, therefore, is an indirect effect, involving changes in transient planetary waves. The vertical coherent changes of the zonal winds confirm what was found by Wu and Smith (2016), that the symmetric PA projects onto the annular mode of variability in both the stratosphere and troposphere amplifying the tropospheric response via a stratospheric pathway.

To investigate the impact of asymmetric PA, two different latitudinal forcing extents are considered, one experiment, whose forcing covers 90° in longitudes and another one, whose forcing covers 180° in longitudes. The latter one is, in addition to a flat surface, also performed with idealized wave 1 orography. Note, that the DFP90 has the same amplitude as the DFP180, but covers only half the size. Therefore, the ΔDFP90 zonal mean temperature change is only half of the ΔDFP180 change. Since both have a doubled amplitude with respect to the DFP360 experiment, the ΔDFP180 zonal temperature change is similar to the ΔDFP360 change and therefore better comparable to each other.

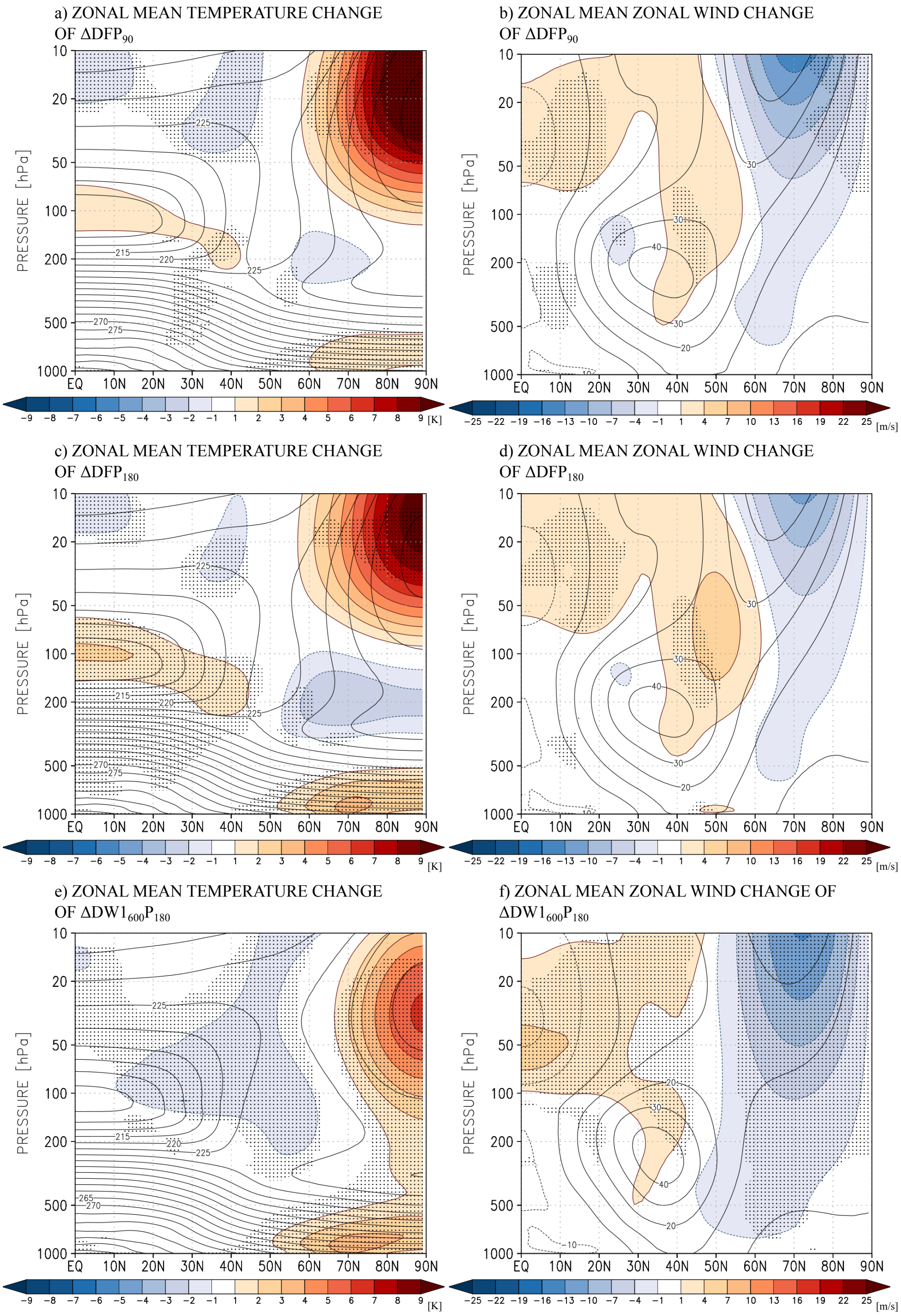

Figure 3.12. ΔDFP$_{90}$, ΔDFP$_{180}$, ΔDW1$_{600}$P$_{180}$ steady state temperature and zonal wind change shown in color shading. Stippling mark areas where the change is significant using the 95th percentile threshold. Contour lines show the control experiment's steady state.

The ΔDFP90, ΔDFP180 and ΔDW1$_{600}$P180 steady state temperature and zonal wind changes are shown in Figure 3.12. All changes have in common a warming of the polar

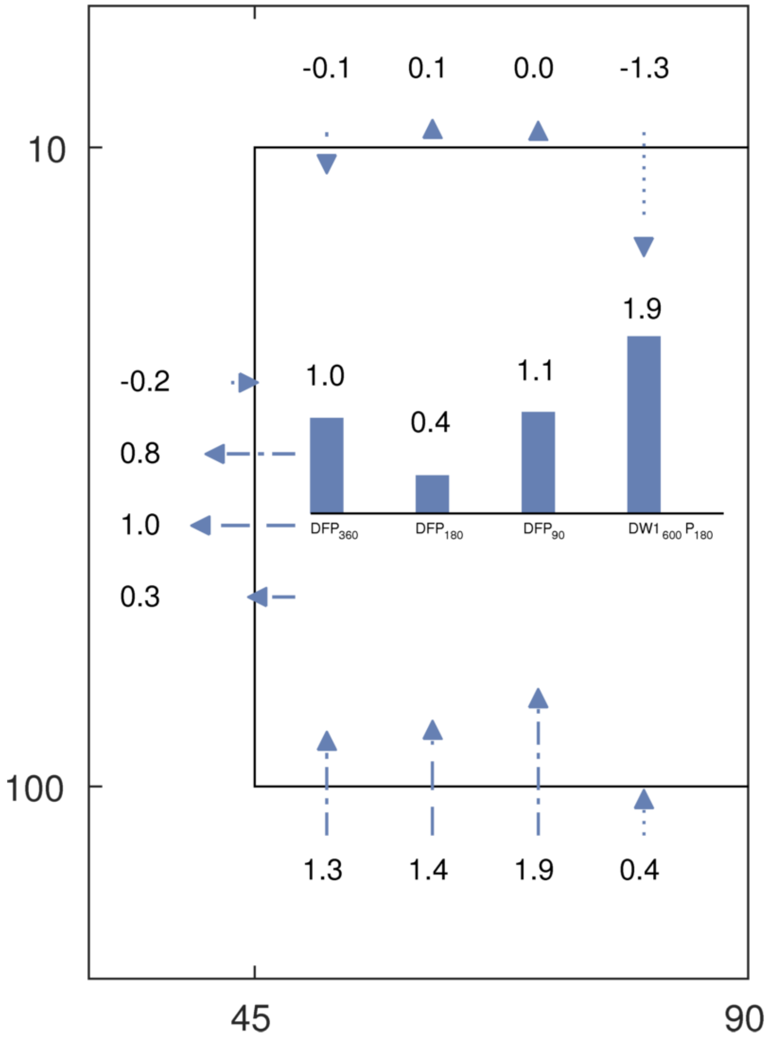

Figure 3.13. ΔDFP$_{360}$, ΔDFP$_{180}$, ΔDFP$_{90}$and ΔDW1$_{600}$P$_{180}$ EP box budget change between 45°N/S and 90°N/S and between 100hPa and 10hPa. The arrows indicate the time mean EP-flux change integrated over the respective boundary. The bars in the center denote the EP-flux convergence change. Positive values mean increased wave dissipation. The values next to the bars and arrows quantify the change. They are given in units of of 10^4 kg m s^{-4}. The arrows' length are scaled with respect to the ΔDFP$_{360}$ change at the bottom boundary. The ΔDFP$_{360}$ arrow length is set arbitrary. The same applies to the bars.

near surface temperature, which is about 1K in the ΔDFP90 change and about 3K in the ΔDFP180 and ΔDW1$_{600}$P180 change. They further share an stratospheric dynamically driven increase in polar temperature and an high latitude vertical coherent easterly change. However, there are differences in the lower stratosphere. Interestingly, the ΔDFP90 change shows stronger response of stratospheric temperatures and a more intense easterly change than the ΔDFP180 even though the DFP90 surface warming is only half of the DFP180 one.

To understand the difference the high latitude wave dissipation changes are quantified.

Table 3.3. Change of mean (μ) eddy-driven jet latitude (EDJ) [deg.] and EDJ speed [m/s] for the ΔDFT, ΔD_{gw}FT and ΔD_jFT change and their monthly standard deviation change (σ). Stars mark mean changes, that are statistical significant.

	ΔDFP360		ΔDFP180		ΔDFP90		ΔDW1_{600}P180	
	μ	σ	μ	σ	μ	σ	μ	σ
EDJ latitude ch.	-0.64	+0.23	+0.39	0.01	-0.25	+0.23	-0.54	0.07
EDJ speed ch.	+0.76*	-0.1	+0.58*	-0.07	+0.34	-0.1	-0.05	+0.03

Figure 3.13 shows the ΔDFP90, ΔDFP180 and ΔDW1_{600}P180 EP-flux budget changes. Indeed, the ΔDFP90 change shows more wave dissipation change than the ΔDFP180. Most of the higher dissipation change comes from stronger increase of tropospheric wave flux. Only part of the higher dissipation change is due to less equatorward refraction of waves. This means that PA restricted to 90° is more potent in increasing the wave flux into the stratosphere than a PA that expands over 180° in longitude.

When comparing the tropospheric ΔDFP_{90} and ΔDFP_{180} zonal wind changes to the ΔDFP_{360} zonal wind change, obviously the tropospheric changes are less pronounced in case of an asymmetric thermal forcing. This is also found in the eddy-driven jet properties. The ΔDFP_{90} and ΔDFP_{180} eddy-driven jet latitude changes are found to be non-significant. The ΔDFP_{180} jet speed change is less strong than the ΔDFP_{360} change, but still significant. The ΔDFP_{90} jet speed change is non-significant. These results suggest that the asymmetric thermal forcing, in particular the one that spans 90° in longitudes,poses an efficient source of additional wave flux into the stratosphere but, however, projects less strong on the tropospheric annular mode of variability.

The $\Delta DW1_{600}P_{180}$ lower stratosphere temperature increase extents to lower altitudes than the ΔDFP_{180} temperature change. Further, the $\Delta DW1_{600}P_{180}$ high latitude easterly change is much more pronounced and statistically significant. The EP-flux budget change shows much more wave dissipation change. Surprisingly, the higher increase in wave dissipation isn't due to increase upward wave flux (the wave flux change is even smaller than the ΔDFP_{180} change) but due to decreased wave penetration into the upper stratosphere. In other words, the wave dissipation increases because more waves break in the lower stratosphere.

The $DW1_{600}P_{180}$ experimental setup is constructed in a way, that the thermal forcing is in the same hemisphere (eastern hemisphere) as the positive anomaly of the low latitude stationary wave 1. This setup, therefore, facilitates constructive interference of the additional thermal forcing induced stationary wave with the low latitude stationary wave (orography). Figure 3.14 shows the $\Delta DW1_{600}P_{180}$ mean change of the geopotential height zonal anomaly averaged over the 30°N/S and 60°N/S. In deed,

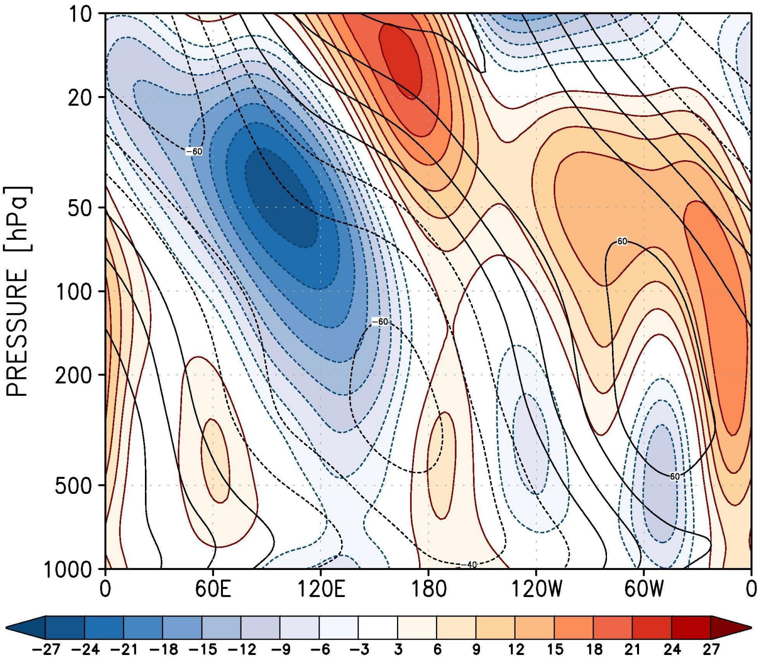

Figure 3.14. Pressure-longitude cross section of the $\Delta DW1_{600}P_{180}$ geopotential height zonal anomaly change averaged between 30°N/S and 60°N/S shown in color shading. The contour lines show the control experiment's steady state.

constructive interference occurs given that the positive zonal anomalies increase and the negative anomalies decrease. The vertical westward tilt of the stationary wave is slightly increased, which accounts for increased wave flux. The increased stationary wave amplitudes, instead, may lead to wave breaking at lower latitudes, which may account for the reduced wave propagation into the upper stratosphere.

3.2.3 CO_2 Induced Stratopause Cooling

Increasing the CO_2 concentration in ICON-DRY hardly impact the troposphere since the greenhouse effect is limited given that there is no water vapor feedback (no moisture) and given that the SSTs are fixed. Further, ICON-DRY neither has interactive chemistry. Therefore, with ICON-DRY the maximum possible biases on the dynamical response can be quantified by only investigating the thermodynamical impact of the stratosphere induced cooling due to quadrupled CO_2 concentration, without changes in O_3 concentrations and tropospheric thermodynamical changes.

The ΔDFS temperature response is shown in Figure 3.15a. Due to the radiative changes a considerable cooling in the middle stratosphere is found. The pattern of cooling resembles the DF control experiment's temperature distribution. This is expected, since the long wave radiation strongly depends on the temperature, which is described by

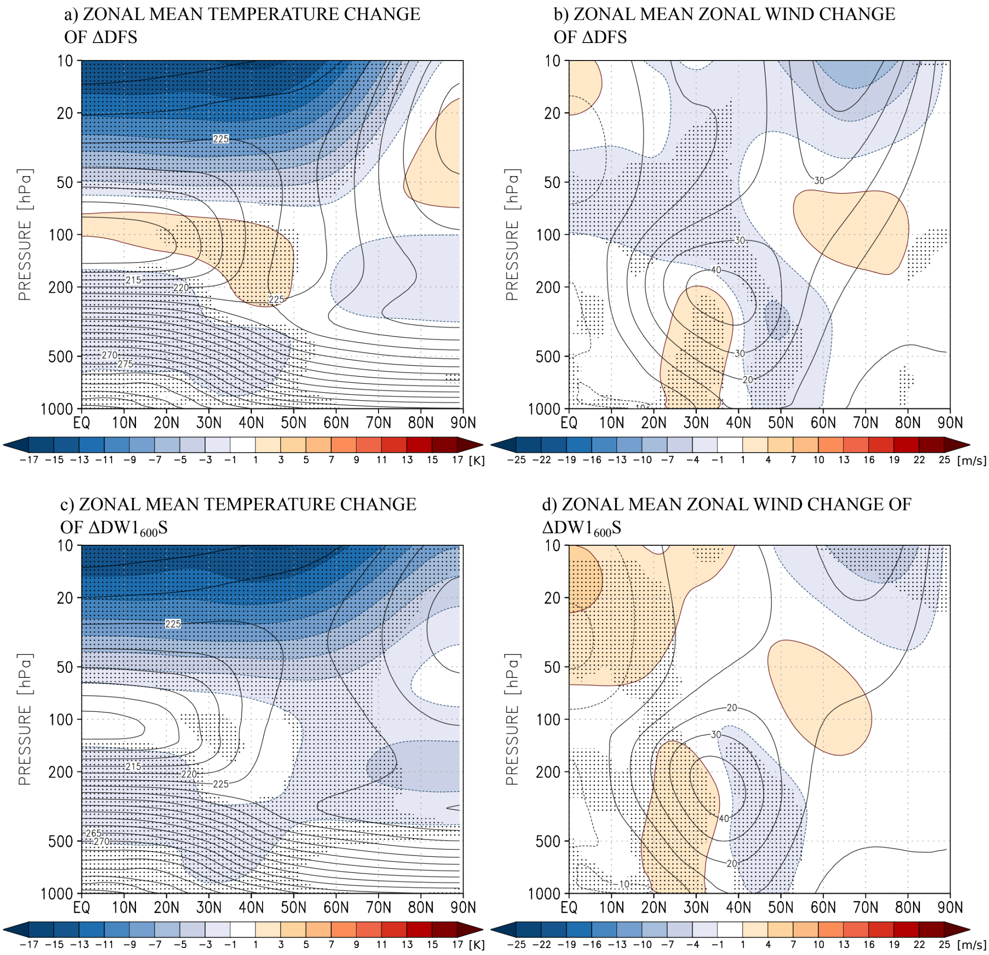

a) ZONAL MEAN TEMPERATURE CHANGE OF ΔDFS

b) ZONAL MEAN ZONAL WIND CHANGE OF ΔDFS

c) ZONAL MEAN TEMPERATURE CHANGE OF $\Delta DW1_{600}S$

d) ZONAL MEAN ZONAL WIND CHANGE OF $\Delta DW1_{600}S$

Figure 3.15. ΔDFPS and $\Delta DW1_{600}S$ steady state temperature and zonal wind change shown in color shading. Stippling mark areas where the change is significant using the 95th percentile threshold. The method used to calculate the statistical significance is explained in section 2.3.6. Contour lines show the control experiment's steady state.

the Stefan-Boltzmann law. There are, further, significant changes in the lower stratosphere and also in the troposphere. These temperature changes can be attributed to dynamically induced changes, since the thermally induced CO_2 cooling only reaches down to the middle stratosphere Akmaev (2002). However, an direct thermal impact of the CO_2 on the troposphere can not entirely be ruled out. Therefore, the focus is on the stratospheric dynamical changes. The ΔDFS stratospheric zonal wind change shows a weakening of the polar vortex. However, the change is not significant with the exception of a small region at 10hPa between 80°N and 90°N. The $\Delta DW1_{600}S$ temperature and zonal wind change is shown in Figure 3.15c and Figure 3.15d, respectively. Including, a stationary wave does not change the response strongly. Nevertheless, the high latitude wind change becomes more significant and the easterly change of the zonal winds reaches to lower altitudes at the high latitudes. Furthermore, the zonal

wind response is more statistically significant than without stationary waves.
Even though the experiments have slightly different control stratospheric background flows, the stratospheric zonal wind response is similar and therefore can be considered as robust. Hence, the CO_2 induced cooling helps to weaken the polar vortex as its response is in the same direction as the change that is induced by stationary waves (orography).

3.3 Baroclinic Eddies

In order to investigate the role of the tropospheric transient eddies in the coupling, this study quantifies the tropospheric mean change of the baroclinic instabilities and its linkage to stratospheric mean zonal mean wind changes for different stationary wave forcing.

In order to investigate the baroclinic instabilities changes the Eady growth rate is considered (Simmonds and Lim, 2009; Vallis, 2006). It is a measure of the maximum growth rate of baroclinic instabilities. The maximum Eady growth rate is given by

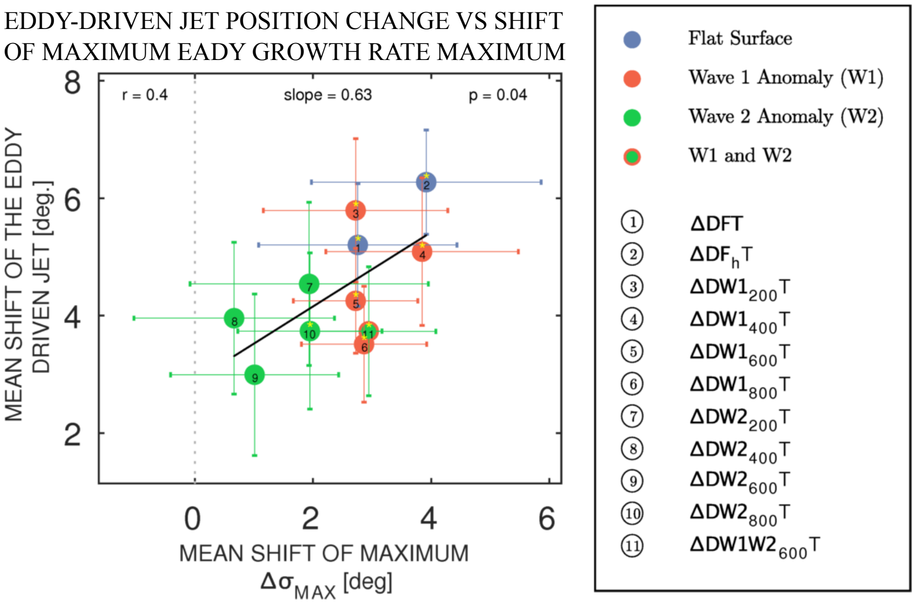

Figure 3.16. ΔDFT, ΔD_{gw}FT, $\Delta W1_{x}$T, $\Delta W2_{x}$T and $\Delta W1W2_{600}$T mean changes of the eddy-driven jet latitude versus the mean shifts of the $\Delta\sigma_{MAX}$ (maximum Eady growth rate). The black line shows the regression line. The p-value is the probability and the r-value the correlation coefficient. The horizontal and vertical lines show the estimated uncertainty of the mean changes. Stars mark changes that are statistically significant with respect to both variables

$$\sigma_{max} = 0.3098 \frac{|f| \left| \frac{\partial U(z)}{\partial z} \right|}{N} \tag{3.16}$$

where 0.3098 is a scaling factor (Lindzen and Farrell, 1980), f the Coriolis parameter, $\frac{\partial U(z)}{\partial z}$ the vertical shear of zonal winds and N the Brunt-Väisälä frequency (static stability). N is given by $\sqrt{\frac{g}{\Theta}\frac{\partial\Theta}{\partial z}}$ where g is the acceleration due to gravity and Θ the potential temperature and z the vertical coordinate. The maximum Eady growth rate, therefore, is mainly described by the vertical shear of zonal winds an the static stability. σ_{max}, $\frac{\partial U(z)}{\partial z}$ and N are calculated for each available level (layer) between 750hPa and 400hPa. Afterward the pressure weighted vertical mean is calculated.

As a starting point the relationship between the change of the σ_{max} and the change of the eddy-driven jet latitude is investigated. Since the σ_{max} has a maximum at the mid-latitudes (Simmonds and Lim, 2009), the question is raised whether the shift in the eddy-driven jet latitude is associated with a shift in the latitudinal maximum of σ_{max}? Figure 3.16 shows the the relationship between the mean Eddy-driven jet position change and the shift of the $\Delta\sigma_{max}$ for the ΔDFT, ΔD$_{gw}$FT, $\Delta DW1_xT$, $\Delta DW2_xT$ and $\Delta DW1W2_{600}T$.

The regression analysis shows a probability value of 0.04 (4 percent), which is only slightly below the in statistics often used threshold of 0.05 (5 percent) to determine significance. A probability value of 4 percent means, that there is still a chance of 4 percent that the arrangement of mean changes is by chance. Given the quite low correlation coefficient of 0.4 and the fact, that the estimated uncertainty bars of many changes overlay each other, the relationship is rather non-significant than significant. Hence, if there is an relationship between the shift in the eddy-driven jet latitude and the shift in the maximum of the Eady growth rate it is rather weak. Moreover, considering the distribution of the $\Delta DW1_xT$ changes and $\Delta DW2_xT$ changes, it rather seems, that

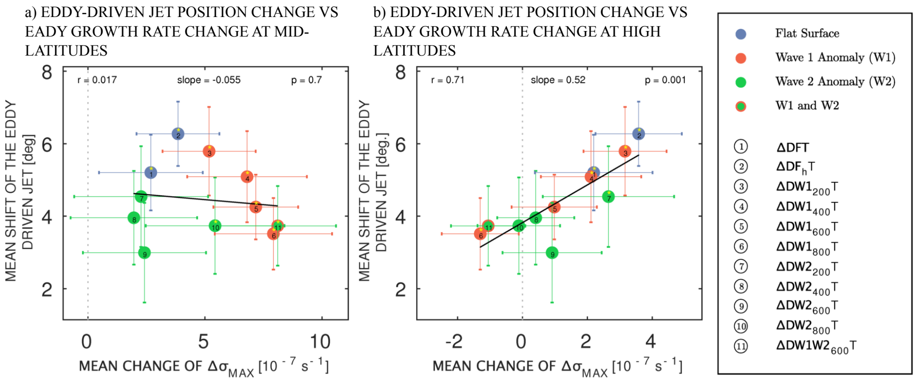

a) EDDY-DRIVEN JET POSITION CHANGE VS EADY GROWTH RATE CHANGE AT MID-LATITUDES

b) EDDY-DRIVEN JET POSITION CHANGE VS EADY GROWTH RATE CHANGE AT HIGH LATITUDES

Figure 3.17. ΔDFT, ΔD$_{gw}$FT, ΔDW1$_x$T, ΔDW2$_x$T and ΔDW1W2$_{600}$T mean change of the eddy-driven jet latitude versus the mean $\Delta\sigma_{max}$ change (maximum Eady growth rate) at mid-latitudes (40°N/S to 60°N/S) and versus the mean $\Delta\sigma_{max}$ change at high latitudes (60°N/S to 80°N/S). The black lines show the regression line. The p-value is the probability and the r-value the correlation coefficient. The horizontal and vertical lines show the estimated uncertainty of the mean changes. Stars mark changes that are statistically significant with respect to both variables there might be a difference between the two groups of experiments, hence, the role of stationary wave 1 and the role of stationary wave 2 in the change, which might be the cause for the weak relationship. Given that no relationship is found between the shift in the eddy-driven jet latitude and the shift in the $\Delta\sigma_{max}$, next latitudinal fixed changes are considered. The questions is raised, whether there is a relationship between the shift in the eddy-driven jet latitude and mean changes of the $\Delta\sigma_{max}$ for a mid-latitude band and a high latitude band.

Figure 3.17 shows the relationship between the shift of the eddy-driven jet and the change of the $\Delta\sigma_{max}$ for a midlatitude band (40°N/S to 60°N/S) and for a high latitude band (60°N/S to 80°N/S). There is no statistical significant relationship between the eddy-driven jet shift and the mid-latitude $\Delta\sigma_{max}$ change given a probability value of 0.7 and a correlation coefficient of 0.017. However, there is a significance relationship at the high latitudes given a probability of 0.001 and a correlation coefficient of 0.71. The strongest increase in the $\Delta\sigma_{max}$ is found in the experiments with a flat surface or idealized orography with small amplitudes. Those, experiments also show the strongest pole-ward shift of the eddy-driven jet. Those experiments that have the largest amplitudes of idealized orography show a decrease of $\Delta\sigma_{max}$ coinciding with the weakest poleward shift of the eddy-driven jet position.

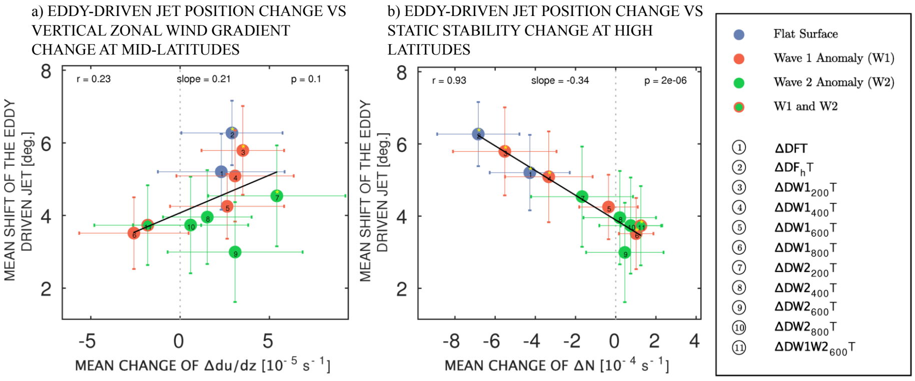

Figure 3.18. ΔDFT, ΔD_{gw}FT, $\Delta DW1_{x}$T, $\Delta DW2_{x}$T and $\Delta DW1W2_{600}$T mean change of the eddy-driven jet latitude versus the mean change of the vertical zonal winds (Δdu/dz) and versus the mean static stability change (N) at the high latitudes (60°N/S to 80°N/S). The black lines show the regression line. The p-value is the probability and the r-value the correlation coefficient. The horizontal and vertical lines show the estimated uncertainty of the mean changes. Stars mark changes that are statistically significant with respect to both variables

The maximum Eady growth rate given by equation 3.1 can easily be decomposed into changes due to vertical zonal wind shear change $\Delta\frac{\partial U(z)}{\partial z}$ and the static stability change ΔN. The relationship between the mean shift of the eddy-driven jet latitude and the high latitude mean change of the vertical wind shear is shown in Figure 3.18a.The relationship between the mean shift of the eddy-driven jet latitude and the high latitude

mean static stability change is shown in Figure 3.18b. The high latitude static stability change determines the statistical significant relationship between the shift of the eddy-driven jet latitude and the maximum Eady growth rate. The relationship between the mean change of the eddy-driven jet latitude and the mean change of the high latitude static stability is very significant given a correlation of 0.93. The question, that follows up is, is there also a relationship between the change of the static stability at the high latitudes and the stratospheric polar vortex change?
Figure 3.19 shows the change of the stratospheric zonal winds at 60°N/S to 70°N/S and at 70°N/S to 80°N/S for two different pressure levels in relationship with the tropospheric static stability change. There is significant relationship between all stratospheric regions given a probability value at least lower than $5*10^{-4}$ and a correlation coefficient at least larger than 0.61.

These results suggest a stratospheric impact on the high latitude tropospheric static stability change. Further, the static stability change at the high latitude troposphere seem

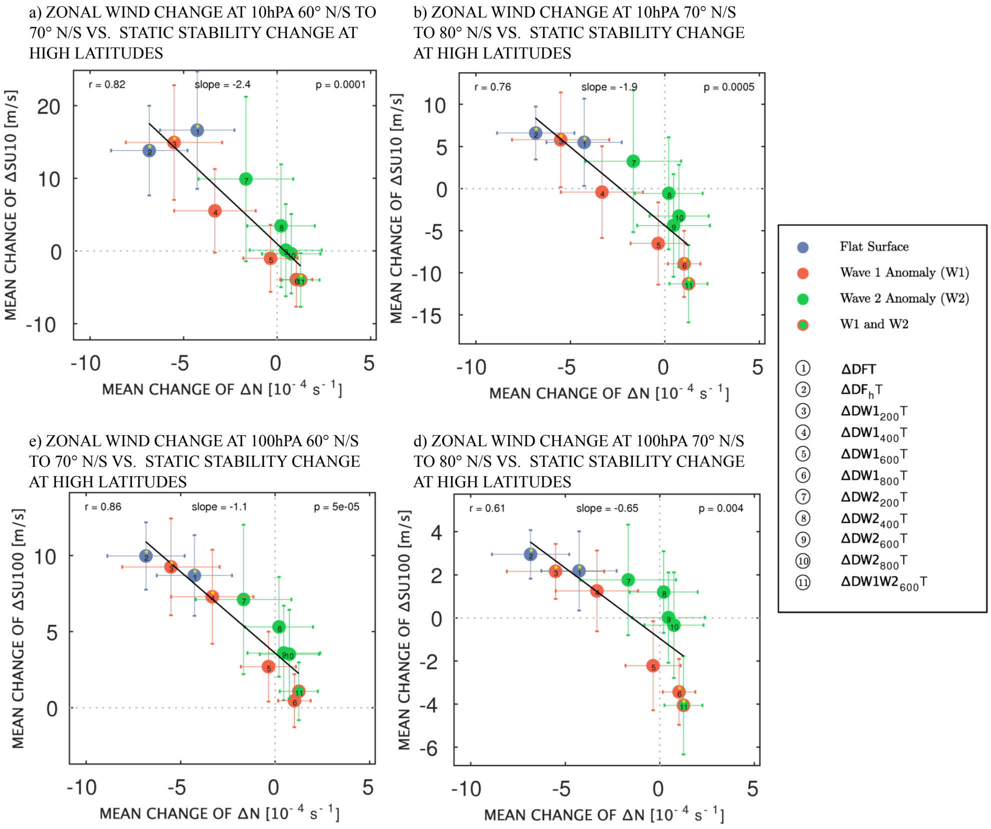

a) ZONAL WIND CHANGE AT 10hPA 60° N/S TO 70° N/S VS. STATIC STABILITY CHANGE AT HIGH LATITUDES

b) ZONAL WIND CHANGE AT 10hPA 70° N/S TO 80° N/S VS. STATIC STABILITY CHANGE AT HIGH LATITUDES

e) ZONAL WIND CHANGE AT 100hPA 60° N/S TO 70° N/S VS. STATIC STABILITY CHANGE AT HIGH LATITUDES

d) ZONAL WIND CHANGE AT 100hPA 70° N/S TO 80° N/S VS. STATIC STABILITY CHANGE AT HIGH LATITUDES

Figure 3.19. ΔDFT, ΔD_{gw}FT, $\Delta DW1_x$T, $\Delta DW2_x$T and $\Delta DW1W2_{600}$T mean change of ΔSU10 at 60°N/S to 70°N/S and at 70°N/S to 80°N/S versus the mean static stability change (N) at the high latitudes (60°N/S to 80°N/S). The black lines show the regression line. The p-value is the probability and the r-value the correlation coefficient. The horizontal and vertical lines show the estimated uncertainty of the mean changes. Stars mark changes that are statistically significant with respect to both variables

to play an important role in the change of the eddy-driven jet position. The question that emerges is what determines the change in the static stability at the tropospheric high latitudes. Since N is given by $\sqrt{\frac{g}{\Theta}\frac{\partial\Theta}{\partial z}}$ the change is determine by changes in the potential temperature. This indicates, that there is an polar upper level temperature amplification possibly induced due to dynamically coupled changes between the stratosphere and the troposphere. Such a warming in the upper polar troposphere is, indeed, found in the experiments with large stationary wave amplitudes (see Appendix: Figure 4.1 to 4.3). Given that the transient eddy feedback projects on the tropospheric intrinsic annular modes (Song and Robinson, 2004), the upper tropospheric polar warming found in the ICON-DRY experiments may be the signature of such an annular mode change. An increase in the static stability at the high latitudes as observed in the experiments with a large stationary wave amplitude, would suppress baroclinic instabilities at the high latitudes, and by that keeping the eddy-driven jet at a lower latitudes as suggest by (Scaife et al., 2012). Therefore, the combination of tropical amplification and stationary waves is a sufficient condition to reproduce what is seen in climate models.

Conclusions and Outlook

4

This chapter, first, gives conclusions on the mean results of the thesis. Afterward the results are summarized and discussed in more detail. The outlook follows at the end.

The winter time stratospheric circulation response and the tropospheric storm track response to global warming remain uncertain. Further, the mechanisms by which the winter time stratospheric circulation response impact the tropospheric storm track response are still incomplete. Understanding the complex climate system and its response to external forcing has often been tackled with idealized models. However, given that complex climate models as well as idealized models come to opposing stratospheric results, there is the need for developing an idealized model framework that is tailored to study the two-way coupled stratosphere-troposphere system under global warming. This is achieved with the ICON-DRY model (first part of the thesis) that consists of full radiation but at the same time is highly idealized in its moist processes. In this sense, it is conceptually similar to the dry dynamical core studies, but by incorporating full radiation is non-simplified regarding radiation-wave interactions.

It is shown that the ICON-DRY model consists of realistic annular mode time-scales and realistic (compared to ERA-Interim) stratospheric polar vortex strengths. The ICON-DRY's atmospheric stationary waves triggered by prescribed idealized orography reproduce the principle signatures of stationary waves of zonal wave number 1 and zonal wave number 2 very well. The ICON-DRY model is, therefore, suitable to study stratosphere-troposphere dynamical responses to external forcing.

In the second part of the thesis, the stratospheric circulation response and its impact on the eddy-driven jet to prescribed tropical amplification (TA), polar amplification (PA) and CO_2 induced stratopause cooling is investigated for the first time in an idealized model with full radiation-wave interactions.

When only dry transient waves are present, it is shown that the response to tropical amplification is largely dominated by wave propagation changes. Regarding the Brewer-Dobson circulation (BDC) response to global warming, dry dynamical core studies, therefore, may be rather inappropriate when it comes to drawing conclusion on whether the BDC will strengthen or weaken due to global warming. It is further shown that wave propagation changes are dependent on the control's eddy-driven jet position relative to the subtropical vortex. An eddy-driven jet close to the subtropical jet (i.e more equatorward) leads to increased poleward refraction of waves at the high latitudes and increased wave dissipation at the high latitudes reducing the high latitude stratospheric winds. An eddy-driven jet that is well separated from the subtropical jet shows increased euqtaorward refraction of waves at all latitudes and a reduction of high latitude wave dissipation leading to intensified westerly winds. Independently on the control's eddy-driven jet position, the eddy-driven jet shifts poleward markedly by about 5.2° to 8.6°. The eddy-driven jet variability is found to depend strongly on the mean state even in an idealized model framework emphasizing the results by Barnes and Polvani (2013) who found that the leading pattern of variability for a given CMIP5 model can be a strong function of the mean jet latitude.

In the presence of moisture, TA leads to a significant increase of baroclinic and planetary waves, increasing the wave flux into the stratosphere and amplifying the wave dissipation change at the high latitudes. The weakening of the polar vortex coincides with an significantly less strong equatorward shift of the eddy-driven jet compared to dry conditions. Moisture, therefore, may also be capable of impacting indirectly the eddy-driven jet response through a stratospheric pathway.

Under dry conditions, only if stationary waves with sufficient large amplitudes are included an increase of stratospheric high latitude wave dissipation is found, as a response to TA. Under dry conditions, if stationary waves are involved in the response to TA, two competing mechanisms are found: (1) The horizontal EP-flux (associated with wave propagation), whose response is a robust reduction of high latitude wave dissipation; and (2) The vertical EP-flux component, whose response is an increase of high latitude wave dissipation. This wave dissipation increase depends strongly on the surface orography amplitude. The increase in wave dissipation leads to a weakening of the stratospheric polar vortex. It is found that the decrease of the stratospheric polar vortex is associated with a significant less strong equatorward shift of the eddy-driven jet. Excluding other possible factor, the stratospheric circulation change is found to be the dominant factor in limiting the poleward shift of the eddy-driven jet as a response to TA.

The circulation responses to polar amplification is found to be more complex than the circulation response to tropical amplification. The asymmetric polar amplification poses an additional wave source that increases wave flux into the stratosphere. Positive interference of the anomalous wave response with the stationary wave (orography) impact the stratospheric circulation mainly due to shifting the preferred region of wave breaking downward. The presence of stationary waves, therefore, may amplify the stratospheric response to asymmetric polar amplification through constructive interference. The zonal wind response shows vertical coherent changes suggesting a strong projection onto the annular mode. The magnitude of the dissipation and zonal wind changes are large, demonstrating that polar amplification has a great potential to impact the stratospheric and tropospheric circulations if the conditions are appropriate (constructive interference). Given that climate models may consists of of both, uncertainty in the stationary wave response and uncertainty in the projection of sea ice retreat (temporal and in space), the asymmetric sea ice retreat poses a potent contributor to the stratospheric circulation uncertainty in climate models.

The CO_2 induced stratopause cooling helps to weaken the polar vortex as its response is in the same direction as the change that is induced by stationary waves (orography). This suggests that interactive chemistry is needed to reduce potentially unrealistic impacts of CO_2 induced stratopause cooling on the stratospheric circulation response. Concerning the response to tropical amplification, the regression analysis diagnosed from experiments with different stationary wave amplitudes show a significant relationship between the high latitude (60°N/S to 80°N/S) static stability change and the eddy-driven jet shift. It is also shown that the change of the high latitude static stability is significantly correlated to the change of the polar vortex at 100 hPa and 10 hPa. This thesis constraints the possible mechanisms responsible for the linkage by showing that stationary waves play a crucial role in the linkage. Given a correlation coefficient of about 0.93 between the eddy-driven jet shift and the high latitude static stability change, it seems that, as a response to TA, the high latitude static stability change is intrinsically linked to the eddy-driven jet position via the presence of stationary waves which on their own are dynamically coupled to the stratosphere. Therefore, this thesis shows a sufficient condition for the static stability increase in climate models (Scaife et al., 2012). In the following the research questions are answered in detail.

4.1 ICON-DRY

Is it possible to construct an idealized numerical model that provides full radiation-wave interactions but which at the same time is highly idealized in its moist processes, allowing for prescribing tropospheric thermal forcing conceptually similar to the HS model?

This thesis demonstrates the possibility of constructing a dry idealized model framework (ICON-DRY) that allows for full wave-radiation interactions but at the same time consists of a dry idealized troposphere allowing for prescribing idealized thermal forcing similar to what is done in dry dynamical core models. Beside the full radiation the ICON-DRY model's advantage is that the steady state background temperature and wind field can adapt to external forcing, making the model more realistic than the dry dynamical core model with a prescribed temperature profile. Hence, the ICON-DRY model's complexity is placed in between a dry dynamical core model such as the Held-Suarez model and the Aquaplanet model.

The ICON-DRY model is forced by fixed uniformly distributed SST profile, the Coriolis force and the short wave radiation. It is further forced by a zonally symmetric idealized thermal forcing which substitutes atmospheric heating rates related to moist processes in order to drive a tropospheric circulation which is realistic in terms of magnitude and spatial scales. The idealized forcing substitutes heating rates related to latent heating, evaporative cooling and absorption of short wave radiation due to the moist compounds. It further substitutes indirectly the effects of moisture on the vertical diffusion and sensible heat flux. The zonally symmetric thermal forcing is a function that is built from heating rates obtained from a moist version by using a best fit algorithm. The best fit algorithm creates the idealized thermal forcing by applying a number of bivariate Gaussian functions.

The ICON-DRY model is validated by means of control experiments with different idealized orophrahical wave numbers (1 and 2) and different amplitudes (200m, 400m, 600m, 800m). Since the ICON-DRY model is forced by an idealized thermal heating that drives the ICON-DRY large-scale circulation, it is necessary to show that ICON-DRY equilibrates. Using the temperature tendency, it is shown that the domain mean vertical pressure weighted total temperature tendency is 3 orders of magnitude smaller than the noise, and further a few orders of magnitude smaller than the idealized thermal forcing. Therefore, it is shown that the ICON-DRY model equilibrates within the first 12 months of the simulation.

Using the European Centre for Medium-Range Weather Forecasts reanalysis data ERA-Interim, it is shown that sinusoidal surface anomalies with at least 600m lead to atmospheric stationary waves comparable to what is observed in ERA-Interim. Further, it can be shown that for an experiment with both, an idealized sinusoidal surface wave 1 and wave 2 anomaly, that the spatial distribution of the stationary wave number 2 is modified by the stationary wave number 1 through an down-scale energy transfer. This modification seems to happen also in ERA-Interim. In General, the analysis shows that the ICON-DRY's atmospheric stationary waves triggered by idealized orography reproduce the principle signatures of stationary waves of zonal wave number 1 and zonal wave number 2 very well.

The ERA-Interim southern hemisphere monthly mean climatological zonal winds are compared to an ICON-DRY configuration on a flat surface and the Northern hemisphere monthly mean climatological zonal winds are compared to the ICON-DRY experiment with idealized wave number 1 orography with an amplitude of 600m. It is found that the ICON-DRY experiment with a flat surface compares best with the October mean Southern hemisphere polar vortex and the ICON-DRY experiment with an stationary wave number 1 amplitude of 600m with the February Northern hemisphere polar vortex. Therefore, the strength of the polar vortexes fit into the range of stratospheric polar vortex strengths observed in ERA-Interim. Given that the ICON-DRY tropospheric momentum and temperature fluxes compare reasonably well to the

ERA-Interim fluxes, the ICON-DRY model configurations resemble reasonably well the mean large-scale atmospheric circulation of the in ERA-Interim reanalysis data. Thus, the ICON-DRY is suitable to study large-scale atmospheric dynamics to external forcing.

4.2 Controls of the Stratosphere-Troposphere Response to Thermal Forcing in Idealized Models: Mean Changes.

What is the role of transient waves in the stratospheric polar vortex and eddy-driven jet response to tropical amplification for different background states

The question is answered by using the experiment with a flat surface (DF), the experiment with a flat surface including non-orgraphical gravity wave parameterization ($D_{gw}F$) and the experiment with a flat surface consisting of an equatorward shifted eddy-driven jet (D_jF). It is found that the stratospheric circulation change to tropical amplification on a flat surface under dry conditions is largely determined by wave propagation changes. Wave generation changes play only a minor role. This is true also when the gravity wave parameterization is included or the control's eddy-driven jet is shifted toward the equator.

The wave propagation changes, however, depend on the tropospheric mean state. It is shown that for an eddy-driven jet that is shifted poleward with respect to the subtropical jet, an intensified equatorward refraction is found at all latitudes. However, in case of an eddy-driven jet that is closer to the subtropical jet (equatorward shifted eddy-driven jet), the intensified equatorward refraction of waves are found to be constrained to the mid-latitudes. Instead, at the high latitudes a change to poleward refracted waves is found leading to increased wave dissipation at polar latitudes and leading to an easterly change of the high latitude zonal winds. The vertical EP-flux change is slightly negative in all experiments.

These results may shed some light on the discussion of why dry dynamical core studies often come to different stratospheric circulation responses to idealized thermal forcing. The study of Butler et al. (2010) and Eichelberger and Hartmann (2005) use an Held-Suarez (HS) model and a similar forcing (TA), but come to different results regarding the lower stratospheric circulation change and the Brewer-Dobson circulation (BDC) change. The lower stratospheric temperature change of the ICON-DRY experiment with a flat surface (ΔDFT) can be compared to Figure 2a of Butler et al. (2010) and Figure 2 of Eichelberger and Hartmann (2005). This temperature change is dynamically driven since there is no forcing in the stratosphere and therefore gives an estimate on the BDC change. The polar latitude temperature decrease found in Butler et al.

(2010) point into the direction of an decreased BDC. They support their finding by the decrease of the net-hemispheric vertical flux in their HS model. Eichelberger and Hartmann (2005) instead find an increase in stratospheric temperatures, an increase in the upward wave flux and an increase in the BDC.

However, when looking at both studies' temperature changes in detail and comparing them to ICON-DRY flat surface experiment responses, the stratospheric temperature changes, surprisingly, aren't that different. The temperature change in Eichelberger and Hartmann (2005) shows a similar band of increased mid-latitude temperature as the ΔDFT change. They, also show an polar decrease of temperature, which, however, is non-significant. Butler et al. (2010)'s temperature change shows also an adiabatic warming at pressure level below 50hPa. Further, there has been concerns about artificially forced baroclinic instabilities in the Eichelberger and Hartmann (2005) study's experimental setup, which might have contributed to the increased upward wave flux. Given the advantage of the ICON-DRY model that the mean temperature state is not prescribed and therefore is capable of adapting to the additional thermal forcing, the ICON-DRY model experiments are more realistic compared to the HS model. For this reason and because of the results obtained and described above the change in the net-hemispheric wave flux in simplified models on a flat surface (only transient) seems to be negative, but in any case small.

Given that this study finds horizontal wave propagation changes being the most important contributor to the stratospheric changes on a flat surface under dry conditions and given that the wave propagation changes depend on the mean tropospheric state in particular the relative position of the eddy-driven jet to the stratospheric polar vortex, it seems that dry dynamical core models do not capture the important process responsible for a potential increase in the upward wave component flux. Potent contributors to the upward wave flux may be stationary waves and moisture related processes.

A considerable poleward shift of the eddy-driven jet of about 5.2° in the ΔDFT change, 6.3° in the ΔD_{gw}FT change and 8.6° in the ΔD_jFT change is found. This demonstrates the potential magnitude of poleward displacement in the absence of compensating (opposing) dynamical influences on the eddy-driven jet related to polar amplification and stratospheric dynamical changes. Further, the ΔDFT, ΔD_{gw}FT and ΔD_jFT changes reveal an intensified meridional eddy-driven jet wobble. The ΔDFT shows no change in the pulsing of the eddy-driven jet, whereas ΔD_{gw}FT and ΔD_jFT show an intensified pulsing of the eddy-driven jet. The increase in the meridional wobble is in agreement with McGraw and Barnes (2016) who also find an increase in the meridional wobble in their HS model as the jet shifts poleward. However, Barnes and Hartmann (2011) who used a barotropic model show an increase in the pulsing of the jet as it shifts poleward. The ΔDFT change is dominated by an intensification of the meridional wobble, whereas the ΔD_{gw}FT and ΔD_jFT change combines both, an increase in the meridional wobble and an increase in the pulsing. A combination of both is also found by Baker et al. (2017). The eddy-driven jet variability, therefore, is found to strongly depend on the mean state emphasizing the results by Barnes and Polvani (2013) who found that the leading pattern of variability for a given CMIP5 model can be a strong function of the mean jet latitude.

Do moisture related effects impact the troposphere-stratosphere coupled response on a flat surface

It is shown that the presence of moisture contributes to the stratospheric vertical EP-flux change due to an increase in wave generation at planetary and synoptic-scale waves. The increase of planetary waves may happen due to an upscale energy cascade from synoptic sale waves. Geen et al. (2016) showed that moisture leads to a strengthening of the cold sector's heat transport suggesting an additional feedback mechanism onto the midlatitude heat transport. This might be an explanation for the increase in baroclinic waves in the moist experiment.
The moist control experiment's eddy-driven jet is positioned close to the subtropical jet similar as in the D_j experiments. The moist experiment's horizontal EP-flux component change is similar as the ΔD_jFT EP-flux component change showing increased equatorward refraction of waves at the mid-latitudes and increased poleward refraction at high latitudes. Therefore, the moist experiment change can confirm the role of the controls eddy-driven jet position in the response of the stratospheric wave propagation change. However, the vertical EP flux component change is much larger in the moist experiment than in the ΔD_jFT change. It is found that the wave generation increase leads to increased wave penetration into the stratosphere amplifying the high latitude wave dissipation increase and leading to an easterly change of the polar vortex. The weakening of the polar vortex coincide with an significantly equatorward shift of the eddy-driven jet compared to dry conditions. Moisture, therefore, may also be capable of impacting indirectly the eddy-driven jet response through a stratospheric pathway.

What is the role of stationary waves in limiting the poleward shift of the eddy-driven jet through a stratospheric pathway?

The role of the stationary waves are tested by prescribing an identical additional thermal forcing to the control experiments with different idealized orographical wave numbers (1 and 2) and different amplitudes (200m, 400m, 600m, 800m,)
Two competing mechanisms are found: (1) The horizontal EP-flux (associated with

wave propagation), whose response is a robust reduction of high latitude wave dissipation; and (2) The vertical EP-flux component, whose response is an increase of high latitude wave dissipation. This wave dissipation increase depends strongly on the surface orography amplitude. In order to overcompensate the decrease of wave dissipation due to the stronger equatorward refraction, it is found that the idealized surface orography amplitude needs to be at least 400m high. Further, it is found that the stationary wave number 2 is more potent to impact the stratospheric circulation change than the stationary wave number 1 for small amplitudes. This is because the stationary wave number 2 even in case of an amplitude of only 200m break at lower stratospheric levels than the stationary wave 1 with an amplitude of 200m. However, it is shown that the stationary wave 1 is more potent in effecting the stratospheric circulation for wave amplitudes larger than 600m.
Further, a significant relationship between the tropospheric eddy-driven jet latitude change and stratospheric circulation response is found. For each 1m/s reduction of the polar vortex an equatorward shift of 0.12° is found. This poses the upper end of the potential impact of the stratospheric circulation on the position of the eddy-driven jet in the experiments, since as shown in section 3.2.1 there are some small direct impacts of the tropics on the eddy-driven jet shift.

Is there a condition, under which the asymmetric component of polar amplification affects the eddy-driven jet through a stratospheric pathway

In this study the eddy-driven jet response is investigated to an asymmetric PA with different longitudinal extends and in combination with idealized stationary wave number 1 orography.
It is shown that the the asymmetric thermal forcing, in particular the one that spans 90° in longitudes, pose an efficient source of additional wave flux into the stratosphere but, however, projects weakly onto the tropospheric annular mode of variability. Further, it is shown that the asymmetric thermal forcing that spans 180° constructively interferes with the lower latitude orographically forced stationary wave. The vertical westward tilt of the stationary wave is slightly increased which accounts for increased wave flux. The increased stationary wave amplitudes, instead, may lead to wave breaking at lower latitudes which may account for the reduced wave propagation into the upper stratosphere.The presence of stationary waves, therefore, may amplify the stratospheric response to asymmetric polar amplification through constructive interference. The zonal wind response shows vertical coherent changes suggesting a strong projection onto the annular mode. The magnitude of the dissipation and zonal wind changes are large, demonstrating that polar amplification has a great potential to impact the

stratospheric and tropospheric circulations if the conditions are appropriate (constructive interference). Polar amplification therefore may be an potent contributor to the stratospheric circulation change in climate models.
An increase of the eddy-driven jet speed is found as a response to the asymmetric polar amplification. The impact of the polar amplification on the position of the eddy-driven jet is found to be small and in all polar amplification cases non-significant.

How large is the potential bias in the stratospheric response without chemistry?

The CO_2 induced cooling helps to weaken the polar vortex and its response is in the same direction as the change that is induced by stationary waves (orography). This suggests that interactive chemistry is needed to reduce potentially unrealistic impacts of CO_2 induced stratosphere cooling on the circulation response.

What is the role of the baroclinic eddies in the stratosphere-troposphere coupled response including different stationary wave amplitudes?

The role of the baroclinic eddies are studied for different control experiments' orography amplitudes by calculating the eady-growth rate and the contributions of the vertical zonal wind shear and static stability, separately. It is found that there is no association between the shift of the Eady growth rate maximum an the eddy-driven jet shift. Considering a high latitudinal (60° to 80°) and a mid-latitudinal band (40° to 60°), it is found that the high latitude Eady growth rate change is significantly linked to the eddy-driven jet shift. Further, it is found that the link is mainly due to the changes in the high latitude static stability change. It is also shown that the change of the high latitude static stability is significantly correlated to the change of the polar vortex at 100 hPa and 10 hPa.
As a response to tropical amplification, this means, that the higher the idealized surface orography, the less strong the equatorward shift of the eddy-driven jet, the less strong the decrease in high latitude static stability and the weaker the polar vortex. Scaife et al. (2012) has found that climate models that consist of a well resolved stratosphere show a high latitude change in the baroclinic growth rate shifting the preferred latitude for growth of eddies, and hence the storm tracks southward. This thesis constraints the possible mechanisms responsible for the linkage by showing one sufficient condition. Given a correlation coefficient of about 0.93 between the eddy-driven jet shift and the high latitude static stability change, it seems that the high latitude static stability change is intrinsically linked to the eddy-driven jet position involving the presence of stationary waves which on their own are coupled to the stratosphere. Given the

annular structure of the response, it may be likely that the direct impact of stratospheric anomalies onto the tropospheric baroclinic eddies is rather unimportant as suggested by Hitchcock and Simpson (2016). However, this does not exclude the possibility that the baroclinic eddies, once shifted to the south by planetary scale changes, feed back onto annular modes maintaining the equatorward displacement of eddies.

4.3 Outlook

The results of this thesis show that the stationary waves are crucial in the downward coupling between the stratospheric mean changes and the tropospheric mean eddy-driven jet shift. The change of the stratospheric vortex may, however, not only be directly caused by the stationary wave flux changes themselves but may incorporate changes in transient wave fluxes via changes in the mean background flow. To understand the role of the stationary waves in the response to TA, especially regarding the stratospheric polar vortex change but also regarding the high latitude static stability change, it is therefore necessary to investigate the contributions of transient planetary and stationary waves to the total wave dissipation change. Moreover, the contributions of the transient planetary waves may be separated into high frequency waves and low-frequency (quasi-stationary) waves to investigate the role of wave variability changes in the stratospheric response.

Further, this thesis shows, when only transient waves are present, that moisture is an important contributor to the stratospheric changes as it poses a significant contribution to increased tropospheric wave activity. In the presence of stationary waves, however, their relative contribution is not known. From the results shown here it cannot be concluded, how relevant moisture is in more complex model configurations, when the wave number space incorporates more wave activity.

Only recently there have been studies that have been investigating the asymmetric (regional) sea ice retreat in a systematic manner. Given that the potential impact on the stratosphere and the feedback (downward coupling) to the troposphere in the real atmosphere remain illusive and given that this thesis shows that the potential impact of the asymmetric polar amplification may be pronounced, there is the need to gain an understanding on the limits of the asymmetric sea ice retreat to impact the stratospheric polar vortex by the use of simplified models. This can be achieved by prescribing heating sources with different sizes and amplitude at different relative positions to a prescribed idealized wavenumner 1 and 2 orography In ICON-DRY. The dynamical responses may than be analyzed regarding time-mean linear and time-mean nonlinear changes.

Bibliography

Akmaev, R., 2002: Modeling the cooling due to co2 increases in the mesosphere and lower thermosphere. *Physics and Chemistry of the Earth, Parts A/B/C*, **27 (6)**, 521 – 528.

Andrews, D., J. Holton, and C. Leovy, 1987: *Middle Atmosphere Dynamics*. International Geophysics, Elsevier Science.

Andrews, D. G. and M. E. McIntyre, 1976: Planetary waves in horizontal and vertical shear: The generalized eliassen-palm relation and the mean zonal acceleration. *Journal of the Atmospheric Sciences*, **33 (11)**, 2031–2048.

Andrews, D. G. and M. E. McIntyre, 1978: Generalized eliassen-palm and charney-drazin theorems for waves on axismmetric mean flows in compressible atmospheres. *Journal of the Atmospheric Sciences*, **35 (2)**, 175–185.

Baker, H. S., T. Woollings, and C. Mbengue, 2017: Eddy-driven jet sensitivity to diabatic heating in an idealized gcm. *Journal of Climate*, **30 (16)**, 6413–6431.

Baldwin, M. P., X. Cheng, and T. J. Dunkerton, 1994: Observed correlations between winter-mean tropospheric and stratospheric circulation anomalies. *Geophysical Research Letters*, **21 (12)**, 1141–1144.

Baldwin, M. P. and T. J. Dunkerton, 1999: Propagation of the arctic oscillation from the stratosphere to the troposphere. *Journal of Geophysical Research: Atmospheres*, **104 (D24)**, 30 937–30 946.

Baldwin, M. P. and T. J. Dunkerton, 2001: Stratospheric harbingers of anomalous weather regimes. *Science*, **294 (5542)**, 581–584, doi:10.1126/science.1063315.

Baldwin, M. P. and D. W. Thompson, 2009: A critical comparison of stratosphere–troposphere coupling indices. *Quarterly Journal of the Royal Meteorological Society*, **135 (644)**, 1661–1672.

Barnes, E. A. and D. L. Hartmann, 2011: Rossby wave scales, propagation, and the variability of eddy-driven jets. *Journal of the Atmospheric Sciences*, **68 (12)**, 2893–2908.

Barnes, E. A. and L. Polvani, 2013: Response of the midlatitude jets, and of their variability, to increased greenhouse gases in the cmip5 models. *Journal of Climate*, **26 (18)**, 7117–7135.

Bates, J. R., 1977: Dynamics of stationary ultra-long waves in middle latitudes. *Q. J. Royal Meteorol. Soc.*, **103 (437)**, 397–430, doi:10.1002/qj.49710343703.

Boville, B. A., 1984: The influence of the polar night jet on the tropospheric circulation in a gcm. *Journal of the Atmospheric Sciences*, **41 (7)**, 1132–1142, doi:10.1175/1520-0469(1984)041<1132:TIOTPN>2.0.CO;2.

Boyd, J. P., 1976: The noninteraction of waves with the zonally averaged flow on a spherical earth and the interrelationships on eddy fluxes of energy, heat and momentum. *Journal of the Atmospheric Sciences*, **33 (12)**, 2285–2291.

Butler, A. H., D. W. J. Thompson, and R. Heikes, 2010: The steady state atmospheric circulation response to climate change like thermal forcings in a simple general circulation model. *J. Climate*, **23**, 3474 – 3496.

Cai, D., M. Dameris, H. Garny, and T. Runde, 2012: Implications of all season arctic sea-ice anomalies on the stratosphere. *Atmospheric Chemistry and Physics*, **12 (24)**, 11 819–11 831.

Deser, C., R. A. Tomas, and L. Sun, 2015: The role of ocean–atmosphere coupling in the zonal-mean atmospheric response to arctic sea ice loss. *Journal of Climate*, **28 (6)**, 2168–2186.

Domeisen, D. I. V., L. Sun, and G. Chen, 2013: The role of synoptic eddies in the tropospheric response to stratospheric variability. *Geophysical Research Letters*, **40 (18)**, 4933–4937.

Doyle, J. D., C. Amerault, C. A. Reynolds, and P. A. Reinecke, 2014: Initial condition sensitivity and predictability of a severe extratropical cyclone using a moist adjoint. *Monthly Weather Review*, **142 (1)**, 320–342.

Duchon, C. E., 1979: Lanczos filtering in one and two dimensions. *Journal of Applied Meteorology*, **18 (8)**, 1016–1022.

Eichelberger, S. J. and D. L. Hartmann, 2005: Changes in the strength of the brewer-dobson circulation in a simple agcm. *Geophysical Research Letters*, **32 (15)**.

Fels, S. B., 1985: Radiative–dynamical interactions in the middle atmosphere. *Issues in Atmospheric and Oceanic Modeling*, B. Saltzman, Ed., Elsevier, Advances in Geophysics, Vol. 28, 277 – 300.

Frierson, D. M. W., J. Lu, and G. Chen, 2007: Width of the hadley cell in simple and comprehensive general circulation models. *Geophysical Research Letters*, **34 (18)**.

Geen, R., A. Czaja, and J. D. Haigh, 2016: The effects of increasing humidity on heat transport by extratropical waves. *Geophysical Research Letters*, **43 (15)**, 8314–8321.

Geller, M. A., 1983: Dynamics of the middle atmosphere. *Space Science Reviews*, **34 (4)**, 359–375.

Geller, M. A. and J. C. Alpert, 1980: Planetary wave coupling between the troposphere and the middle atmosphere as a possible sun-weather mechanism. *Journal of the Atmospheric Sciences*, **37 (6)**, 1197–1215, doi:10.1175/1520-0469(1980)037<1197:PWCBTT>2.0.CO;2.

Gerber, E. P. and L. M. Polvani, 2009: Stratosphere–troposphere coupling in a relatively simple agcm: The importance of stratospheric variability. *Journal of Climate*, **22 (8)**, 1920–1933.

Gerber, E. P., S. Voronin, and L. M. Polvani, 2008: Testing the annular mode autocorrelation time scale in simple atmospheric general circulation models. *Monthly Weather Review*, **136 (4)**, 1523–1536.

Giorgetta, M. A., et al., 2018: Icon-a, the atmosphere component of the icon earth system model: I. model description. *Journal of Advances in Modeling Earth Systems*, **10 (7)**, 1613–1637.

Hardiman, S. C., D. G. Andrews, A. A. White, N. Butchart, and I. Edmond, 2010: Using different formulations of the transformed eulerian mean equations and eliassen–palm diagnostics in general circulation models. *Journal of the Atmospheric Sciences*, **67 (6)**, 1983–1995.

Held, I. M. and M. J. Suarez, 1994: A proposal for the intercomparison of the dynamical cores of atmospheric general circulation models. *Bulletin of the American Meteorological Society*, **75 (10)**, 1825–1830.

Hitchcock, P., T. G. Shepherd, M. Taguchi, S. Yoden, and S. Noguchi, 2013: Lower-stratospheric radiative damping and polar-night jet oscillation events. *Journal of the Atmospheric Sciences*, **70 (5)**, 1391–1408.

Hitchcock, P. and I. R. Simpson, 2016: Quantifying eddy feedbacks and forcings in the tropospheric response to stratospheric sudden warmings. *Journal of the Atmospheric Sciences*, **73 (9)**, 3641–3657.

Jaiser, R., K. Dethloff, and D. Handorf, 2013: Stratospheric response to arctic sea ice retreat and associated planetary wave propagation changes. *Tellus A: Dynamic Meteorology and Oceanography*, **65 (1)**, 19 375.

Karpechko, A. Y. and E. Manzini, 2012: Stratospheric influence on tropospheric climate change in the northern hemisphere. *Journal of Geophysical Research: Atmospheres*, **117 (D5)**.

Karpechko, A. Y. and E. Manzini, 2017: Arctic stratosphere dynamical response to global warming. *Journal of Climate*, **30 (17)**, 7071–7086.

Kidston, J., A. A. Scaife, S. C. Hardiman, D. M. Mitchell, N. Butchart, M. P. Baldwin, and L. J. Gray, 2015: Stratospheric influence on tropospheric jet streams, storm tracks and surface weather. *Nature Geoscience*, **8**, 433–440.

Kim, B.-M., S.-W. Son, S.-K. Min, J.-H. Jeong, S.-J. Kim, X. Zhang, T. Shim, and J.-H. Yoon, 2014: Weakening of the stratospheric polar vortex by arctic sea-ice loss. *Nature Communications*, **5 (4646)**.

Kodera, K., K. Yamazaki, M. Chiba, and K. Shibata, 1990: Downward propagation of upper stratospheric mean zonal wind perturbation to the troposphere. *Geophysical Research Letters*, **17 (9)**, 1263–1266.

Kushner, P. J. and L. M. Polvani, 2004: Stratosphere–troposphere coupling in a relatively simple agcm: The role of eddies. *Journal of Climate*, **17 (3)**, 629–639.

Lin, B.-D., 1982: The behavior of winter stationary planetary waves forced by topography and diabatic heating. *Journal of the Atmospheric Sciences*, **39 (6)**, 1206–1226.

Lindzen, R. S. and B. Farrell, 1980: A simple approximate result for the maximum growth rate of baroclinic instabilities. *Journal of the Atmospheric Sciences*, **37 (7)**, 1648–1654.

Lorenz, D. J. and D. L. Hartmann, 2001: Eddy–zonal flow feedback in the southern hemisphere. *Journal of the Atmospheric Sciences*, **58 (21)**, 3312–3327.

Lu, J., G. Chen, and D. M. W. Frierson, 2010: The position of the midlatitude storm track and eddy-driven westerlies in aquaplanet agcms. *Journal of the Atmospheric Sciences*, **67 (12)**, 3984–4000.

Manzini, E., et al., 2014: Northern winter climate change: Assessment of uncertainty in cmip5 projections related to stratosphere-troposphere coupling. *J. Geophys. Res. Atmos.*, **119 (13)**, 7979–7998.

McGraw, M. C. and E. A. Barnes, 2016: Seasonal sensitivity of the eddy-driven jet to tropospheric heating in an idealized agcm. *Journal of Climate*, **29 (14)**, 5223–5240.

Nakamura, T., K. Yamazaki, K. Iwamoto, M. Honda, Y. Miyoshi, Y. Ogawa, Y. Tomikawa, and J. Ukita, 2016: The stratospheric pathway for arctic impacts on midlatitude climate. *Geophysical Research Letters*, **43 (7)**, 3494–3501.

Neale, R. B. and B. J. Hoskins, 2000: A standard test for agcms including their physical parametrizations: I: the proposal. *Atmospheric Science Letters*, **1 (2)**, 101–107.

Nigam, S., 1990: On the structure of variability of the observed tropospheric and stratospheric zonal-mean zonal wind. *Journal of the Atmospheric Sciences*, **47 (14)**, 1799–1813.

Oudar, T., E. Sanchez-Gomez, F. Chauvin, J. Cattiaux, L. Terray, and C. Cassou, 2017: Respective roles of direct ghg radiative forcing and induced arctic sea ice loss on the northern hemisphere atmospheric circulation. *Climate Dynamics*, **49 (11)**, 3693–3713.

Palmer, C. E., 1959: The stratospheric polar vortex in winter. *Journal of Geophysical Research*, **64 (7)**, 749–764.

Peings, Y. and G. Magnusdottir, 2014a: Response of the wintertime northern hemisphere atmospheric circulation to current and projected arctic sea ice decline: A numerical study with cam5. *Journal of Climate*, **27 (1)**, 244–264.

Peings, Y. and G. Magnusdottir, 2014b: Response of the wintertime northern hemisphere atmospheric circulation to current and projected arctic sea ice decline: A numerical study with cam5. *Journal of Climate*, **27 (1)**, 244–264.

Perlwitz, J. and H.-F. Graf, 1995: The statistical connection between tropospheric and stratospheric circulation of the northern hemisphere in winter. *Journal of Climate*, **8 (10)**, 2281–2295.

Perlwitz, J. and N. Harnik, 2003: Observational evidence of a stratospheric influence on the troposphere by planetary wave reflection. *Journal of Climate*, **16 (18)**, 3011–3026.

Petoukhov, V. and V. A. Semenov, 2010: A link between reduced barents-kara sea ice and cold winter extremes over northern continents. *Journal of Geophysical Research: Atmospheres*, **115 (D21)**.

Plumb, R. A., 2002: Stratospheric transport. *Journal of the Meteorological Society of Japan. Ser. II*, **80 (4B)**, 793–809.

Polvani, L. M. and P. J. Kushner, 2002: Tropospheric response to stratospheric perturbations in a relatively simple general circulation model. *Geophysical Research Letters*, **29 (7)**, 18–1–18–4.

Ronalds, B., E. Barnes, and P. Hassanzadeh, 2018: A barotropic mechanism for the response of jet stream variability to arctic amplification and sea ice loss. *Journal of Climate*, **31 (17)**, 7069–7085.

Rossby, C.-G., 2015: Relation between variations in the intensity of the zonal circulation of the atmosphere and the displacements of the semi-permanent centers of action.

Scaife, A. A., et al., 2012: Climate change projections and stratosphere–troposphere interaction. *Climate Dynamics*, **38 (9)**, 2089–2097.

Schmitz, G. and N. Grieger, 1980: Model calculations on the structure of planetary waves in the upper troposphere and lower stratosphere as a function of the wind field in the upper stratosphere. *Tellus*, **32 (3)**, 207–214, doi:10.1111/j.2153-3490.1980.tb00948.x.

Screen, J. A., 2014: Far-flung effects of arctic warming. *Nature Geoscience*, **10**, 253–254.

Screen, J. A., I. Simmonds, C. Deser, and R. Tomas, 2013: The atmospheric response to three decades of observed arctic sea ice loss. *Journal of Climate*, **26 (4)**, 1230–1248.

Shaw, T. A., J. Perlwitz, and N. Harnik, 2010: Downward wave coupling between the stratosphere and troposphere: The importance of meridional wave guiding and comparison with zonal-mean coupling. *Journal of Climate*, **23 (23)**, 6365–6381.

Shepherd, T. G., 2014: Atmospheric circulation as a source of uncertainty in climate change projections. *Nature Geoscience*, **7**, 703–708.

Shine, K. P., 1987: The middle atmosphere in the absence of dynamical heat fluxes. *Quarterly Journal of the Royal Meteorological Society*, **113 (476)**, 603–633.

Sigmond, M. and J. F. Scinocca, 2010: The influence of the basic state on the northern hemisphere circulation response to climate change. *Journal of Climate*, **23 (6)**, 1434–1446.

Simmonds, I. and E.-P. Lim, 2009: Biases in the calculation of southern hemisphere mean baroclinic eddy growth rate. *Geophysical Research Letters*, **36 (1)**.

Simpson, I. R., P. Hitchcock, R. Seager, Y. Wu, and P. Callaghan, 2018: The downward influence of uncertainty in the northern hemisphere stratospheric polar vortex response to climate change. *Journal of Climate*, **31 (16)**, 6371–6391.

Song, Y. and W. A. Robinson, 2004: Dynamical mechanisms for stratospheric influences on the troposphere. *Journal of the Atmospheric Sciences*, **61 (14)**, 1711–1725.

Sun, L., C. Deser, and R. A. Tomas, 2015: Mechanisms of stratospheric and tropospheric circulation response to projected arctic sea ice loss. *Journal of Climate*, **28 (19)**, 7824–7845.

Swart, N. C. and J. C. Fyfe, 2012: Observed and simulated changes in the southern hemisphere surface westerly wind-stress. *Geophysical Research Letters*, **39 (16)**.

Thatcher, D. R. and C. Jablonowski, 2016: A moist aquaplanet variant of the held-suarez test for atmospheric model dynamical cores. *Geoscientific Model Development*, **9 (4)**, 1263–1292.

Thompson, D. W. J. and J. M. Wallace, 1998: The arctic oscillation signature in the wintertime geopotential height and temperature fields. *Geophysical Research Letters*, **25 (9)**, 1297–1300.

Thompson, D. W. J. and J. M. Wallace, 2000: Annular modes in the extratropical circulation. part i: Month-to-month variability. *Journal of Climate*, **13 (5)**, 1000–1016.

Vallis, G. K., 2006: *Planetary Waves and the Stratosphere*, 541–580. Cambridge University Press.

Wan, H., et al., 2013: The icon-1.2 hydrostatic atmospheric dynamical core on triangular grids – part 1: Formulation and performance of the baseline version. *Geoscientific Model Development*, **6 (3)**, 735–763.

Wang, S., E. P. Gerber, and L. M. Polvani, 2012: Abrupt circulation responses to tropical upper-tropospheric warming in a relatively simple stratosphere-resolving agcm. *Journal of Climate*, **25 (12)**, 4097–4115.

Waugh, D. W., A. H. Sobel, and L. M. Polvani, 2017: What is the polar vortex and how does it influence weather? *Bulletin of the American Meteorological Society*, **98 (1)**, 37–44.

Woollings, T., A. Hannachi, and B. Hoskins, 2010: Variability of the north atlantic eddy-driven jet stream. *Quarterly Journal of the Royal Meteorological Society*, **136 (649)**, 856–868.

Woollings, T., B. Hoskins, M. Blackburn, and P. Berrisford, 2008: A new rossby wave–breaking interpretation of the north atlantic oscillation. *Journal of the Atmospheric Sciences*, **65 (2)**, 609–626.

Wu, Y. and K. L. Smith, 2016: Response of northern hemisphere midlatitude circulation to arctic amplification in a simple atmospheric general circulation model. *Journal of Climate*, **29 (6)**, 2041–2058.

Yin, J. H., 2005: A consistent poleward shift of the storm tracks in simulations of 21st century climate. *Geophysical Research Letters*, **32 (18)**.

Zängl, G., D. Reinert, P. Rípodas, and M. Baldauf, 2015: The icon (icosahedral non-hydrostatic) modelling framework of dwd and mpi-m: Description of the non-hydrostatic dynamical core. *Quarterly Journal of the Royal Meteorological Society*, **141 (687)**, 563–579.

Appendix

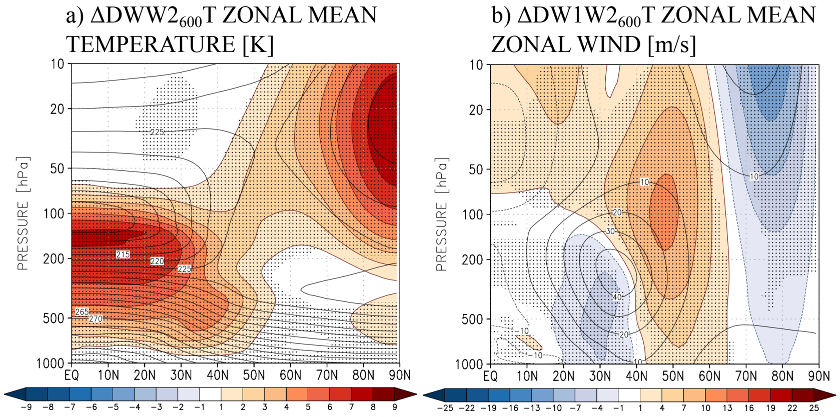
a) ΔDWW2$_{600}$T ZONAL MEAN TEMPERATURE [K]

b) ΔDW1W2$_{600}$T ZONAL MEAN ZONAL WIND [m/s]

Figure 4.1. ΔDW1W2$_{600}$T steady state zonal mean temperature and zonal mean zonal wind response to tropical amplification. Countour lines show the control experiment's steady state.

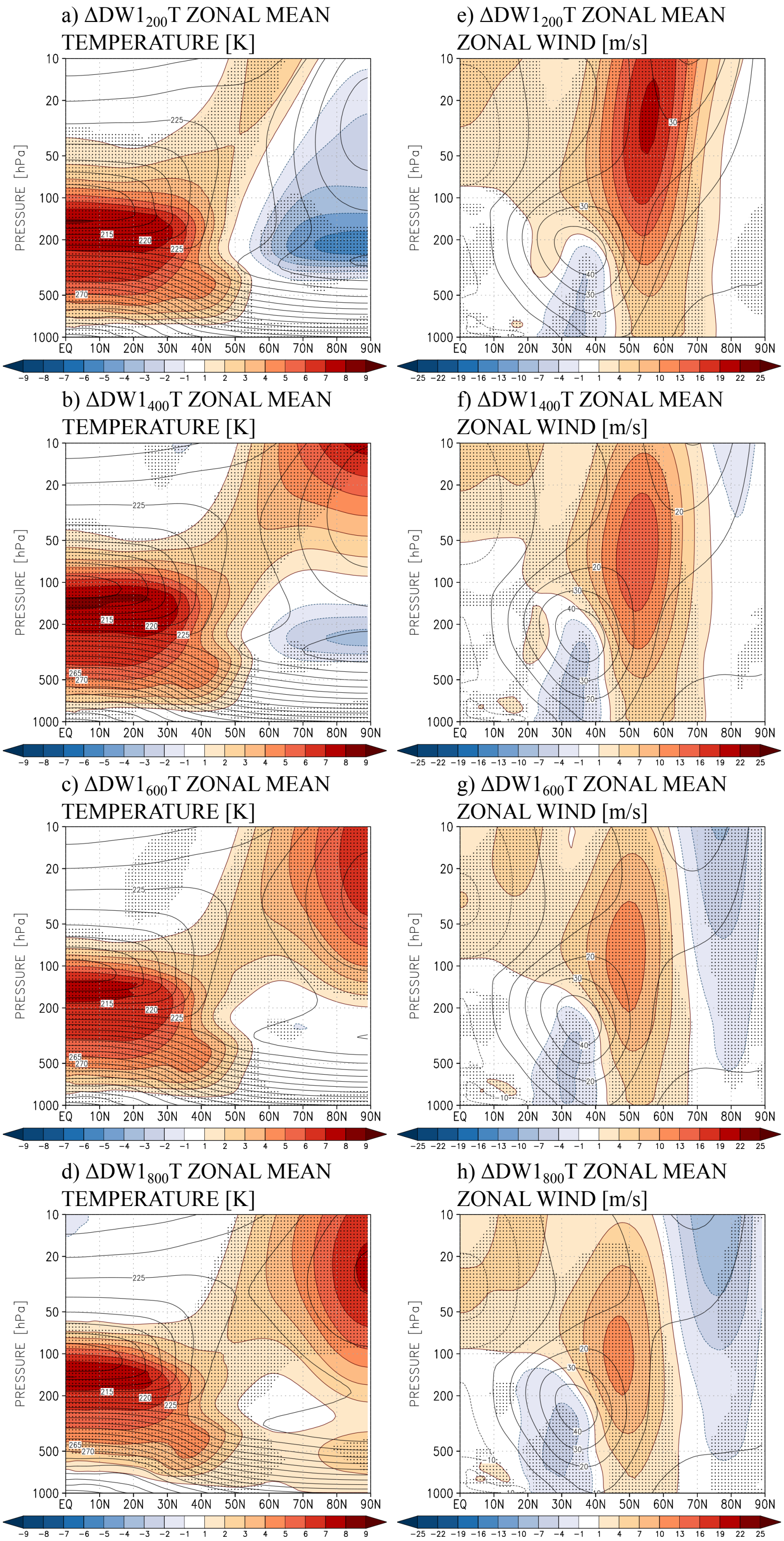

a) ΔDW1$_{200}$T ZONAL MEAN TEMPERATURE [K]

e) ΔDW1$_{200}$T ZONAL MEAN ZONAL WIND [m/s]

b) ΔDW1$_{400}$T ZONAL MEAN TEMPERATURE [K]

f) ΔDW1$_{400}$T ZONAL MEAN ZONAL WIND [m/s]

c) ΔDW1$_{600}$T ZONAL MEAN TEMPERATURE [K]

g) ΔDW1$_{600}$T ZONAL MEAN ZONAL WIND [m/s]

d) ΔDW1$_{800}$T ZONAL MEAN TEMPERATURE [K]

h) ΔDW1$_{800}$T ZONAL MEAN ZONAL WIND [m/s]

Figure 4.2. ΔDW1$_x$T steady state zonal mean temperature and zonal mean zonal wind response to tropical amplification. Countour lines show the control experiment's steady state.

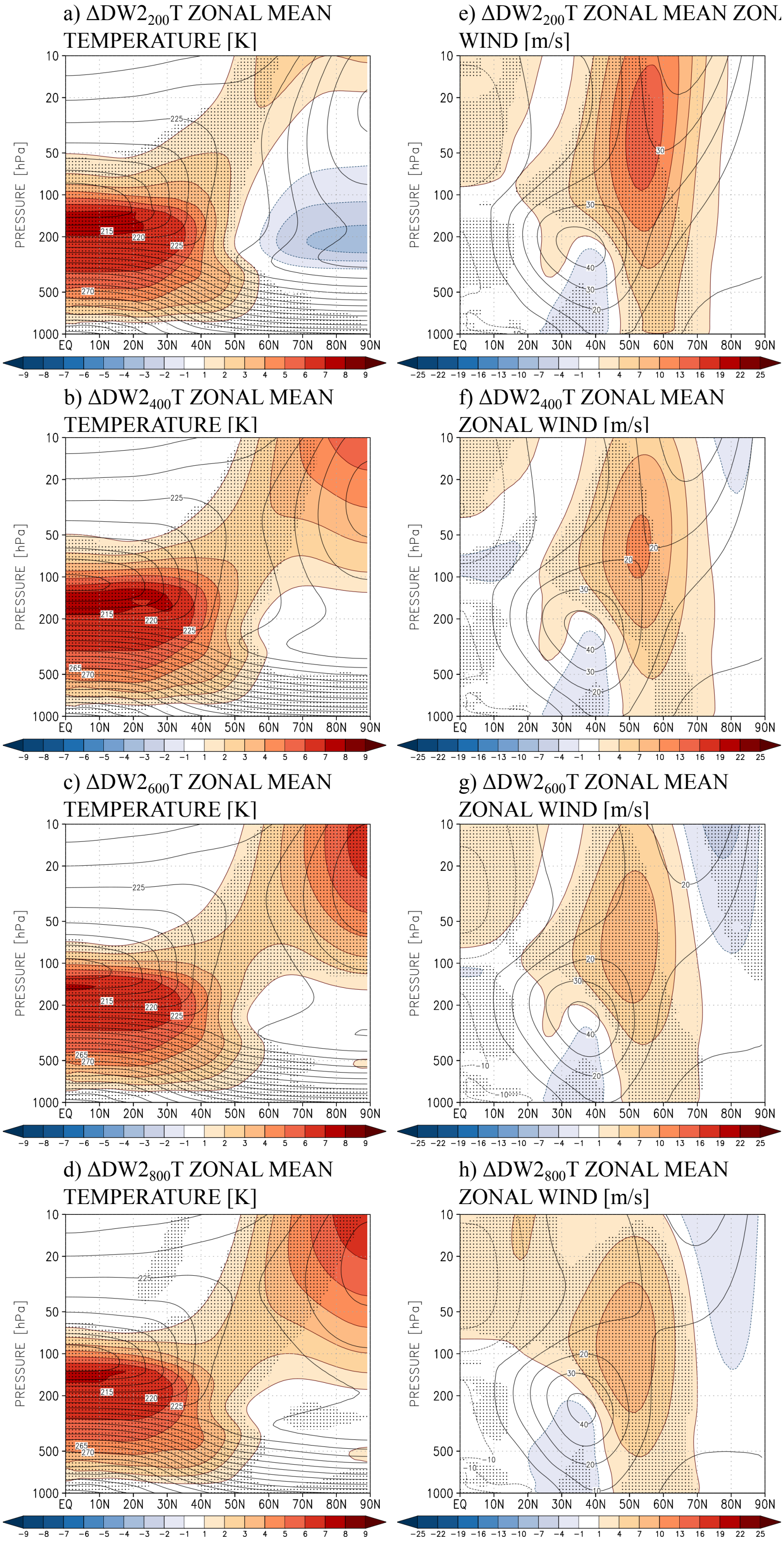

a) ΔDW2$_{200}$T ZONAL MEAN TEMPERATURE [K]

e) ΔDW2$_{200}$T ZONAL MEAN ZON WIND [m/s]

b) ΔDW2$_{400}$T ZONAL MEAN TEMPERATURE [K]

f) ΔDW2$_{400}$T ZONAL MEAN ZONAL WIND [m/s]

c) ΔDW2$_{600}$T ZONAL MEAN TEMPERATURE [K]

g) ΔDW2$_{600}$T ZONAL MEAN ZONAL WIND [m/s]

d) ΔDW2$_{800}$T ZONAL MEAN TEMPERATURE [K]

h) ΔDW2$_{800}$T ZONAL MEAN ZONAL WIND [m/s]

Figure 4.3. ΔDW2$_x$T steady state zonal mean temperature and zonal mean zonal wind response to tropical amplification. Countour lines show the control experiment's steady state.

List of Figures

1.1 Sketch of the key elements of the tropospheric and stratospheric circulation. Depicted are the polar vortex, the subtropical jet, the eddy-driven jet, the Brewer-Dobson circulation (BDC) and the upward propagation of waves. The black line separating the stratosphere and the troposphere represents the tropopause region 2

1.2 Composite of weak and strong polar vortex events represented by the Northern annular mode, calculated using the geopotential height at all levels between 1 hPa and 1000 hPa and between 20°N 90°N. The events are determined by the dates on which the 10 hPa annular mode values cross -3 and +1.5, respectively. With respect to those onset dates composites are calculated covering a period ranging from -60 day lag to +60 day lag. The composite consists of 15 weak events and 32 strong events. Color shading and contours show the standard deviation. The Figure is produced by using ERA-Interim data during 1979 -2008 and therfeore is an update of the Figure of Baldwin and Dunkerton (2001) who used reanalysis data from the National Centers for Environmental Prediction during 1958-1999 4

2.1 Basic state of the zonal mean temperature (a,b), the zonal mean zonal wind (c,d), and zonal mean stream function (e,f) shown for the MOIST-AP on the left and for the DRY-AP on the right. 15

2.2 Heating rates due to the evaporative cooling and diabatic warming (a) and short wave radiation (b) in the MOIST-AP in K/day. 17

2.3 Heating rates due to long wave radiation in the MOIST-AP (a) and in the DRY-AP (b) in K/day. Heating rates due to vertical diffusion in MOIST-AP (a) and in DRY-AP (b) in K/day. 18

2.4 Sum of the heating rates due to evaporative cooling and diabatic warming, the water vapour related long wave radiation, the vertical diffusion difference and tropospheric short wave radiation in K/day (a). The tuned thermal forcing is shown in K/day in (b). 20

2.5 Information and figure on the additional thermal forcing in ICON-DRY. Tropical amplification is shown in pressure - latitude plane in a), symmetric polar amplification is shown in a polar-stereographic projection in b), asymmetric polar amplification spanning 180° and 90° in longitude are shown in c) and d) respectively. 25

2.6 Domain mean temperature tendency evolution of the ICON-DRY's DF control experiment. The red line shows the spinup phase and the black line the data 28

2.7 Stationary wave amplitudes at 500hPa for different surface geopotential height anomalies. a) and b) show control experiments with a forced stationary wave number 1. c) and d) show control experiments with a forced stationary wave number 2. The left column shows the filtered stationary wave number 1 and the right column the filtered stationary wave number 2. 31

2.8 Polar stereographic plot of the filtered stationary wavenumber 1 (upper row) and stationary wave number 2 (bottom row) at 500hPa. a) shows the $DW1_{600}$ control experiments and c) the $DW2_{600}$ control experiments. b) and d) show ERA-Interim Northern hemisphere stationary waves. Red crosses denote maxima and blue crosses minima of the sinusoidal anomaly in the geopotential height. 32

2.9 Polar stereographic plot of the filtered stationary wavenumber 2 at 500hPa for a)the $DW1_{600}$ control experiments and b) the $DW1DW2_{600}$ control experiments. 33

2.10 The upper row shows the time mean of the temperature flux together with the time mean of the temperature. The bottom row shows the time mean of the momentum flux together with the time mean zonal mean wind for a) and c) the DF control experiment and for b) and c) September ERA-Interim reanalysis. The Northern hemisphere is masked with a gray shading since the DC control experiment is more comparable to the southern hemisphere in terms of orography. 34

2.11 Seasonal evolution of the climatological (1979 to 2012) zonal mean zonal wind for ERA-Interim shown in a). Comparison between the time mean zonal mean zonal wind of the DF and the southern hemisphere October ERA-Interim time mean zonal mean zonal wind is shown in b). Comparison between the time mean zonal mean zonal wind of the DFW1_{600} and the Northern hemisphere February ERA-Interim time mean zonal mean zonal wind is shown in c) 35

3.1 ΔDFT, ΔD_{gw}FT and ΔD_jFT steady state temperature [K] and zonal wind [m/s] change shown in color shading. Stippling mark areas where the change is significant using the 95^{th} percentile threshold. Contour lines show the respective control experiment's steady state. 38

3.2 ΔDFT, ΔD_{gw}FT and ΔD_jFT lower stratospheric zonal wind tendency due to EP-flux divergence shown in color shading [m/s/d]. Arrows show the EP-flux change. The Arrow size is scaled in order to fit visual properties. 41

3.3 ΔDFT, ΔD_{gw}FT and ΔD_jFT lower stratosphere horizontal (top row) and vertical (bottom row) EP-flux component changes in color shading. Stippling mark areas where the change is significant using the 95^{th} percentile threshold. Contour lines show the respective control experiment's steady state. 45

3.4 ΔMF4K steady state temperature [K] and zonal wind [m/s] change shown in color shading. Stippling mark areas where the change is significant using the 95^{th} percentile threshold. Contour lines show the respective control experiment's steady state. 47

3.5 ΔMF4K lower stratosphere zonal wind tendency due to EP-flux divergence shown in color shading in a) [m/s/d]. Arrows show the EP-flux change. The Arrow size is scaled in order for visual proposes. b) and c) show the ΔMF4K lower stratosphere horizontal and vertical EP-flux component changes in color shading in [$10^4 m^3 s^{-2}$], respectively. Stippling mark areas where the change is significant using the 95^{th} percentile threshold. Contour lines show the respective control experiment's steady state 47

3.6 ΔD_jFT and ΔMF4K mean heat flux (top row) wavenumber spectrum change and mean geopotential height variance (bottom row) wavenumber spectrum change at 260hPa shown in color shading. Contour lines show the respective control experiment's steady state. 49

3.7 Mean integrated meridional heat flux change shown in a) and mean integraded geopotential height variance change shown in b). The integration is performed over wavenumber 1 to 12. The red line shows the ΔD_jFT change and the blue line the ΔMF4K change. 50

3.8 ΔDFT, ΔD_{gw}FT, $\Delta DW1_x$T, $\Delta DW2_x$T and $\Delta DW1W2_{600}$T EP box budget changes between 45°N/S and 90°N/S and between 100hPa and 10hPa. The arrows indicate the time mean EP-flux change integrated over the respective boundary. The bars in the center denote the EP-flux convergence change. Positive values mean increased wave dissipation. The gray color shows the flat surface experiments, the red color the experiments with idealized stationary wave 1 orography, the orange color the experiments with idealized stationary wave 2 orography and the yellow color the experiment with idealized stationary wave 1 and wave 2 orography. The values next to the bars and arrows quantify the change. They are given in units of of 10^4 kg m s^{-4}. The arrows' length are scaled with respect to the ΔDFT change at the bottom boundary. The ΔDFT arrow length is set arbitrary. The same applies to the bars. 51

3.9 ΔDFT, ΔD_{gw}FT, $\Delta DW1_xT$, $\Delta DW2_xT$ and $\Delta DW1W2_{600}T$ mean EP-flux divergence change versus mean ΔSU10 change. The black line shows the regression line. The p-value is the probability and the r-value the correlation coefficient. Stars mark changes that are statistically significant with respect to both variables. 52

3.10 ΔDFT, ΔD_{gw}FT, $\Delta DW1_xT$, $\Delta DW2_xT$ and $\Delta DW1W2_{600}T$ mean changes of the eddy-driven jet latitude and speed versus the mean changes of ΔT300 and versus the mean changes of the ΔSU10. The black lines show the regression line. The p-value is the probability and the r-value the correlation coefficient. The horizontal and vertical lines show the estimated uncertainty of the mean changes. Stars mark changes that are statistically significant with respect to both variables. 54

3.11 ΔDFP_{360} steady state temperature and zonal wind change shown in color shading. Stippling mark areas where the change is significant using the 95^{th} percentile threshold. Contour lines show the control experiment's steady state. 56

3.12 ΔDFP_{90}, ΔDFP_{180}, $\Delta DW1_{600}P_{180}$ steady state temperature and zonal wind change shown in color shading. Stippling mark areas where the change is significant using the 95^{th} percentile threshold. Contour lines show the control experiment's steady state. 57

3.13 ΔDFP_{360}, ΔDFP_{180}, $\Delta DFP_{90}$and $\Delta DW1_{600}P_{180}$ EP box budget change between 45°N/S and 90°N/S and between 100hPa and 10hPa. The arrows indicate the time mean EP-flux change integrated over the respective boundary. The bars in the center denote the EP-flux convergence change. Positive values mean increased wave dissipation. The values next to the bars and arrows quantify the change. They are given in units of of 10^4 kg m s^{-4}. The arrows' length are scaled with respect to the ΔDFP_{360} change at the bottom boundary. The ΔDFP_{360} arrow length is set arbitrary. The same applies to the bars. 58

3.14 Pressure-longitude cross section of the ΔDW1$_{600}$P$_{180}$ geopotential height zonal anomaly change averaged between 30°N/S and 60°N/S shown in color shading. The contour lines show the control experiment's steady state. 60

3.15 ΔDFPS and ΔDW1$_{600}$S steady state temperature and zonal wind change shown in color shading. Stippling mark areas where the change is significant using the 95th percentile threshold. The method used to calculate the statistical significance is explained in section 2.3.6. Contour lines show the control experiment's steady state. 61

3.16 ΔDFT, ΔD$_{gw}$FT, ΔDW1$_x$T, ΔDW2$_x$T and ΔDW1W2$_{600}$T mean changes of the eddy-driven jet latitude versus the mean shifts of the $\Delta\sigma_{MAX}$ (maximum Eady growth rate). The black line shows the regression line. The p-value is the probability and the r-value the correlation coefficient. The horizontal and vertical lines show the estimated uncertainty of the mean changes. Stars mark changes that are statistically significant with respect to both variables 62

3.17 ΔDFT, ΔD$_{gw}$FT, ΔDW1$_x$T, ΔDW2$_x$T and ΔDW1W2$_{600}$T mean change of the eddy-driven jet latitude versus the mean $\Delta\sigma_{max}$ change (maximum Eady growth rate) at mid-latitudes (40°N/S to 60°N/S) and versus the mean $\Delta\sigma_{max}$ change at high latitudes (60°N/S to 80°N/S). The black lines show the regression line. The p-value is the probability and the r-value the correlation coefficient. The horizontal and vertical lines show the estimated uncertainty of the mean changes. Stars mark changes that are statistically significant with respect to both variables 63

3.18 ΔDFT, ΔD_{gw}FT, ΔDW1_xT, ΔDW2_xT and ΔDW1W2_{600}T mean change of the eddy-driven jet latitude versus the mean change of the vertical zonal winds (Δdu/dz) and versus the mean static stability change (N) at the high latitudes (60°N/S to 80°N/S). The black lines show the regression line. The p-value is the probability and the r-value the correlation coefficient. The horizontal and vertical lines show the estimated uncertainty of the mean changes. Stars mark changes that are statistically significant with respect to both variables 64

3.19 ΔDFT, ΔD_{gw}FT, ΔDW1_xT, ΔDW2_xT and ΔDW1W2_{600}T mean change of ΔSU10 at 60°N/S to 70°N/S and at 70°N/S to 80°N/S versus the mean static stability change (N) at the high latitudes (60°N/S to 80°N/S). The black lines show the regression line. The p-value is the probability and the r-value the correlation coefficient. The horizontal and vertical lines show the estimated uncertainty of the mean changes. Stars mark changes that are statistically significant with respect to both variables 65

4.1 ΔDW1W2_{600}T steady state zonal mean temperature and zonal mean zonal wind response to tropical amplification. Countour lines show the control experiment's steady state. XVII

4.2 ΔDW1_xT steady state zonal mean temperature and zonal mean zonal wind response to tropical amplification. Countour lines show the control experiment's steady state. XVIII

4.3 ΔDW2_xT steady state zonal mean temperature and zonal mean zonal wind response to tropical amplification. Countour lines show the control experiment's steady state. XIX

List of Tables

2.1 Explanation of acronyms 23

2.2 Decorrelation time-scales τ and estimated uncertainty std(τ_N) of tropospheric and stratospheric annular modes in ICON-DRY control experiments 29

2.3 Correlation coefficients (r-value) and its statistical significance (p-value) for the ICON-DRY control experiments. 30

3.1 Change of mean (μ) eddy-driven jet latitude (EDJ) [deg.] and EDJ speed [m/s] for the ΔDFT, ΔD$_{gw}$FT and ΔD$_j$FT change and their monthly standard deviation change (σ). Stars mark mean changes that are statistically significant 40

3.2 Change of the annular mode decorrelation time-scales $\Delta\tau$ and change of the estimated uncertainty Δstd(τ_N) of tropospheric and stratospheric annular modes 42

3.3 Change of mean (μ) eddy-driven jet latitude (EDJ) [deg.] and EDJ speed [m/s] for the ΔDFT, ΔD$_{gw}$FT and ΔD$_j$FT change and their monthly standard deviation change (σ). Stars mark mean changes, that are statistical significant. 59

Acronyms

AP	Aqua-Planet
CMIP(5)	Coupled Model Intercomparison Project (Phase 5)
ECHAM6	Atmospheric general circulation model (acronym: ECMWF and Hamburg)
EP	Eliassen Palm
GCM	General Circulation Models
HS	Held-Suarez
ICON	ICOsahedral Non-hydrostatic
NAO	North-Atlantic Oscillation
NAM	Northern Annular Mode
PA	Polar Amplification
RCP8.5	Representative Concentration Pathway, +8.5 W/m^2 in the year 2100
SC	CO_2 induced Stratopause Cooling
SST	Sea Surface Temperature
TA	Tropical Amplification
TEM	Transformed Eulerian Mean

Acknowledgments

I would like to thank Elisa Manzini for her initial idea of this thesis and her supervision. I especially appreciated her scientific advises and the discussions, which were essential for realizing this thesis. Special thanks also to the Panel members Gualtiero Badin and Hauke Schmidt for their useful suggestions during the meetings. Thanks to Sebastian Rast for his technical support during the time of the model development and for the helpful discussions.

I would like to thank the IMPRS-ESM team for their great administrative support, which allowed me to focus on my research. Special thanks to Antje Weiz for her administrative advises in the last year of my PHD.

Including my Masters, I have been at the MPI-M for more than 5 years,therefore, I would like to thank all members of the MPI-M for the unique and inspirational atmosphere. It has always been a great pleasure to work in such an interdisciplinary environment. Special thanks to Sebastian, Leonore, Tobias, Kathrine, Sally and many more, for the helpful science chats and more important for all the different social activities.

Zu guter Letzt, danke ich meinem Bruder und meiner Schwester für die Unterstützung und dafür, dass sie immer ein offenes Ohr hatten. Ein besonderer Dank gilt Birgit, die mich nicht nur während meiner Promotion sondern auch während meiner gesamten universitären Ausbildung jederzeit unterstützt hat. Lieber Tom, ich danke dir sehr für deine bedingunglose Unterstützung und den Rückhalt, den du mir während der letzten Jahre gegeben hast.

Eidesstattliche Versicherung

Declaration on Oath

Hiermit versichere ich an Eides statt, dass ich die vorliegende Dissertation mit dem Titel: „Stratospheric controls on northern hemispheric storm tracks“ selbstständig verfasst und keine anderen als die angegebenen Hilfsmittel - insbesondere keine im Quellenverzeichnis nicht benannten Internet-Quellen - benutzt habe. Alle Stellen, die wörtlich oder sinngemäß aus Veröffentlichungen entnommen wurden, sind als solche kenntlich gemacht. Ich versichere weiterhin, dass ich die Dissertation oder Teile davon vorher weder im In- noch im Ausland in einem anderen Prüfungsverfahren eingereicht habe und die eingereichte schriftliche Fassung der auf dem elektronischen Speichermedium entspricht.

I hereby declare, on oath, that I have written the present dissertation by myself and have not used other than the acknowledged resources and aids.

Hamburg, den 6. Februar 2019

Tobias Haufschild

Hinweis / Reference

Die gesamten Veröffentlichungen in der Publikationsreihe des MPI-M
„Berichte zur Erdsystemforschung / Reports on Earth System Science“,
ISSN 1614-1199

sind über die Internetseiten des Max-Planck-Instituts für Meteorologie erhältlich:
http://www.mpimet.mpg.de/wissenschaft/publikationen.html

All the publications in the series of the MPI -M
„Berichte zur Erdsystemforschung / Reports on Earth System Science“,
ISSN 1614-1199

are available on the website of the Max Planck Institute for Meteorology:
http://www.mpimet.mpg.de/wissenschaft/publikationen.html